

# Microwave Synthesis Methods for Lithium-Ion Battery Cathodes

CHRISTOPHER A. HOWARD  
SCHOOL OF PHYSICAL SCIENCES  
UNIVERSITY OF KENT

THESIS SUBMITTED FOR THE DEGREE OF RESEARCH MASTERS IN CHEMISTRY AT THE  
UNIVERSITY OF KENT

SUPERVISED BY DR. SERENA A. CORR AND DR. GAVIN MOUNTJOY  
2011–2014

---

## Declaration

I hereby declare that this thesis is my own work and effort and that it has not been submitted by me or anyone else in support of an application for a degree or qualification at the University of Kent or at any other university. Where other sources of information have been used, they have been acknowledged.

Signed:

A handwritten signature in black ink, consisting of a large, stylized loop that starts on the left, goes up and over, and then comes back down to the left, ending in a small hook.

Date: 20/01/2015

---

## Abstract

With the rapidly expanding market for mobile devices such as mobile phones, laptops and cameras, as well as the push towards greener, more renewable energy sources, rechargeable batteries have been brought to the fore. With the many uses of lithium-ion batteries from high drain appliances to power storage, to vehicle propulsion, varying cathodes are required to provide these differing functionalities.

This thesis contains a comprehensive literature review, outlining the history of secondary batteries, their uses, current technologies and ongoing research topics within the field of lithium-ion battery cathodes.

Bronze-phase vanadium dioxide,  $\text{VO}_2(\text{B})$ , is a very promising cathode material, with higher theoretical capacity than the current commercial lithium cobalt oxide,  $\text{LiCoO}_2$ . Current synthesis techniques for  $\text{VO}_2(\text{B})$  utilise solvothermal synthesis in a Teflon-lined Parr bomb, which is then placed in an oven for 48 hours. Microwave-assisted synthesis had never before been used for  $\text{VO}_2(\text{B})$ , but through its use the reaction time for formation has been significantly reduced.

$\text{VO}_2(\text{B})$  was also characterised through the use of X-ray absorption spectroscopy whilst undergoing a discharge cycle at the Diamond Synchrotron near Oxford, the first experiment of this kind on  $\text{VO}_2(\text{B})$  using a relatively new battery cell design.

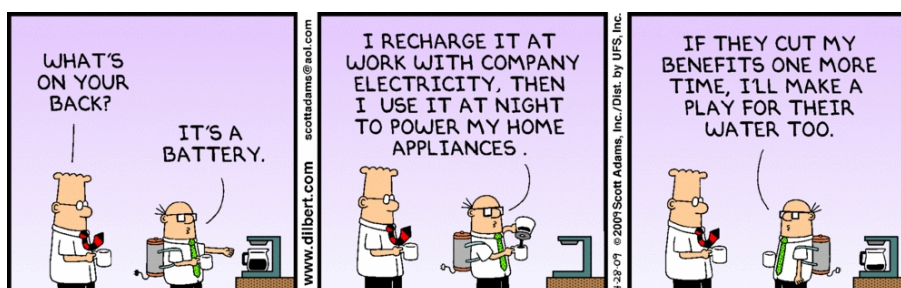
Olivine phosphate structures of iron, manganese and cobalt were also prepared through microwave-assisted synthesis, with lithium iron phosphate being developed as a future electric vehicle battery cathode. These were successfully characterised and cells containing them charge-discharged – the results of these are presented.

---

## Acknowledgements

I would like to thank the following people for this thesis:-

- My supervisor, Dr. Serena Corr for all her support, patience, technical guidance and knowledge within this area of research and helping to make it a very enjoyable degree.
- Dr. Donna Arnold for her assistance with the powder X-ray diffractometers.
- Prof. Alan Chadwick for his help and support with the Synchrotron visit and XAS data analysis.
- Dr. Mark Price for his help and guidance with using the scanning electron microscope.
- Collaborators in Amiens, France for their help with the cycling of my samples.
- Dr. Gavin Mountjoy for his support in writing this thesis.
- The postgraduate students here at the university, namely Kate Belsey, Aaron Kliene and Marc Williams for their assistance and support through the year.
- The Functional Materials Group based at the University of Kent for the regular meetings and presentations.



---

# Contents

<b>Declaration</b>	<b>i</b>
<b>Abstract</b>	<b>ii</b>
<b>Acknowledgements</b>	<b>iii</b>
<b>Contents</b>	<b>vi</b>
<b>List of Figures</b>	<b>xvii</b>
<b>List of Tables</b>	<b>xviii</b>
<b>1 Introduction</b>	<b>1</b>
1.1 General introduction . . . . .	1
1.2 Types of battery . . . . .	1
1.2.1 Lead–acid batteries . . . . .	2
1.2.2 Nickel–cadmium and nickel metal hydride batteries . . . . .	2
1.3 Development of lithium–ion (Li–ion) batteries . . . . .	3
1.3.1 Charging and discharging processes . . . . .	4
1.3.2 Synthesis Methods . . . . .	5
1.3.3 Cathode materials for lithium–ion batteries . . . . .	9
1.3.4 Other components for Li–ion batteries . . . . .	17
1.3.5 Current challenges . . . . .	18
1.4 Aims and objectives . . . . .	20
<b>2 Experimental</b>	<b>21</b>
2.1 Characterisation techniques . . . . .	21
2.1.1 X–ray Diffraction . . . . .	21
2.1.2 Synchrotron Radiation . . . . .	28
2.1.3 Microscopy . . . . .	35

2.1.4	Use of a Potentiostat . . . . .	41
2.2	Starting Materials . . . . .	42
2.3	Experimental Procedures . . . . .	42
2.3.1	Solvothermal synthesis of VO <sub>2</sub> (B) nanorods . . . . .	43
2.3.2	Microwave synthesis of VO <sub>2</sub> (B) . . . . .	44
2.3.3	Swagelok <sup>TM</sup> battery preparation . . . . .	45
2.3.4	Bellcore film preparation for EXAFS experiments . . . . .	46
2.3.5	Preparation of samples for EXAFS measurements . . . . .	46
2.3.6	Microwave synthesis of olivine phosphates . . . . .	47
<b>3</b>	<b>New routes to vanadium oxides</b>	<b>49</b>
3.1	Introduction . . . . .	49
3.2	Preparation and characterisation of VO <sub>2</sub> (B) nanorods . . . . .	50
3.2.1	Solvothermal Synthesis of VO <sub>2</sub> (B) nanorods . . . . .	50
3.2.2	Characterisation of VO <sub>2</sub> (B) nanorods made via solvothermal synthesis . . . . .	50
3.3	Microwave synthesis of VO <sub>2</sub> (B) . . . . .	55
3.3.1	Characterisation of VO <sub>2</sub> (B) made via microwave synthesis at varying reaction times . . . . .	56
3.3.2	Characterisation of VO <sub>2</sub> (B) prepared via microwave synthesis at varying reaction temperatures . . . . .	65
3.4	Discussion . . . . .	68
3.5	Future work . . . . .	70
<b>4</b>	<b>Battery Applications of Vanadate Materials</b>	<b>75</b>
4.1	Potentiostat use in battery characterisation . . . . .	75
4.2	<i>In situ</i> X-ray spectroscopy (XAS) studies . . . . .	77
4.2.1	Pure VO <sub>2</sub> (B) sample . . . . .	77
4.2.2	VO <sub>2</sub> prepared as a Bellcore Film for <i>in situ</i> cycling . . . . .	77
4.3	<i>In situ</i> charge–discharge measurements . . . . .	80

---

4.4	Conclusions and future work . . . . .	83
<b>5</b>	<b>Olivine Phosphate Cathode Materials</b>	<b>85</b>
5.1	Studies of Products of Microwave Synthesis . . . . .	85
5.2	Studies of Products of Microwave synthesis of $\text{LiFePO}_4$ . . . . .	85
5.3	Studies of Products of Microwave synthesis of $\text{LiCoPO}_4$ . . . . .	92
5.4	Studies of Products of Microwave synthesis of $\text{LiMnPO}_4$ . . . . .	97
5.5	Conclusions and Future Work . . . . .	102
<b>6</b>	<b>Conclusions and Future Work</b>	<b>103</b>
6.1	Summary . . . . .	103
6.2	Conclusions . . . . .	104
6.3	Future Work . . . . .	106

## List of Figures

- 1 Crystal structure of  $\text{LiCoO}_2$ , which is commonly used as a cathode material. The lithium ions, shown in green, occupy channels in the structure. 4
- 2 Graphical representation of the charging and discharging processes of a lithium-ion battery. As the battery is charged, (a), lithium ions and electrons leave the cathode and move towards the anode and charger respectively. During discharging, (b), the lithium ions and electrons leave the anode and move towards the cathode and load respectively. . . . . 5
- 3 Schematic representation displaying the evolution of product over time during solid-state synthesis. (a) The interface (orange) where the product forms between the reactants (red, yellow) is small at the start of the reaction. (b) As the reaction progresses, the interface between the two reactants increases as the amount of product increases. This increase in interface and product slows down the reaction due to the increased distance that the reactants have to travel to interact with each other. To limit this, the synthesis is stopped, the sample reground, and placed back into the furnace. . . . . 6
- 4 Graphical representation of (a) a solvothermal bomb and (b) the bomb components. The bomb is designed to allow pressure to build up, but also be released safely if it becomes too high. The reactants are placed within the PTFE liner and the lid placed upon it. Making sure the bottom disc is in correctly, the PTFE liner is then placed within the vessel body. The lower and upper corrosion discs are then placed on top of the PTFE lid and the lower pressure plate added onto that. To finish off, a spring is placed in with the upper pressure plate placed on it, and then the screw cap lid tightened on to maintain a tight seal for the Parr bomb. . . . . 7
- 5 Image of the microwave oven synthesiser used for the experiments within this thesis. . . . . 9

---

6	Structural representations of the olivine structures (a) $\text{LiCoPO}_4$ , (b) $\text{LiFePO}_4$ and (c) $\text{LiMn}_2\text{O}_4$ , which are promising battery cathode materials. Common to each of these structures is an open framework, where the lithium ions (shown here in green) occupy channels in the structure.	11
7	Structure of $\text{VO}_2(\text{B})$ . The red atoms represent oxygen and the blue vanadium atoms. The channels that can be seen within the structure are the pathways taken by lithium ions. Observing from different angles, there can be seen many pathways available for the lithium ions. <sup>1</sup>	14
8	Image displaying the different varieties of coating. (a) shows rough coating, where it can be seen that there are areas where the particle is unprotected. (b) however shows core-shell coating. Here the coating is too thick and impedes the transport of electrons and lithium ions. (c) displays the best option of the three, where a thin, tune-able thickness provides protection for the cathode from the electrolyte and also allows the access and egress of lithium ions and electrons.	19
9	Generation of a $\text{Cu K}\alpha$ X-ray. A 1s electron is ionised, a 2p electron falls into the vacancy in the 1s level and the excess energy is emitted as an X-ray photon.	22
10	Visual representation of Bragg's law, showing the path-length difference $AB + BC$ , which will depend upon the glancing angle, $\theta$ . Constructive interference, or a reflection, will occur when $AB + BC$ is equal to an integer number of the wavelength.	25
11	Miller indices for (a) simple cubic lattice and (b) body-centred cubic lattice displaying planes 100 and 200. The reflection from the 200 plane will interfere with that from the 100 plane, but not vice versa.	26

---

12	Arrangement of a sample, source and detector on the circumference of a circle. The X-rays will leave the source, be monochromated in a collimator, strike the sample and be reflected. The detector (and maybe also the source) will gradually move, increasing in $2\theta$ , detecting the intensity of X-rays at each angle. . . . .	27
13	General diagram of Diamond Light Source Synchrotron based in Oxfordshire, England <sup>2</sup> . . . . .	29
14	Example spectra showing the EXAFS and XANES absorption spectrum of vanadium dioxide. This shows the pre-edge, the XANES region, and the EXAFS region. . . . .	31
15	Schematic of electronic transitions responsible for emission and absorption X-ray spectra. Values included are those of copper. . . . .	32
16	Figure showing the electronic transitions responsible for emission and absorption X-ray spectra. . . . .	33
17	Schematic showing the interference from the outgoing electron and the backscattered electron. Constructive and destructive peaks and troughs occur in the absorption spectra due to these interactions. . . . .	34
18	Figure shows the different signals produced from the sample being struck by the electron beam from the scanning electron microscope. Those used most commonly by scanning electron microscopes are secondary and backscattered electrons. . . . .	38

- 19 The path electrons take in a typical scanning electron microscope set-up to enable the magnification of small objects. The electron gun (a) emits and accelerates the electrons, the condenser lenses (b) then converge this beam to make it finer. The deflection coils then aim the beam at the sample whilst the objective lens (c) focus the beam. The electron beam then leaves the column and enters the sample chamber. The secondary electron detector (d) then detects the electrons emitted, amplifies them and converts them into an electrical signal and transfers this to a computer monitor (e) where the image can be seen. The vacuum pump (f) keeps the column under low pressure at all times. . . . . 40
- 20 Schematic of a two and three-electrode Teflon Swagelok<sup>TM</sup> cell. The major difference between the two is the addition of a third electrode (b). This acts as a reference for the voltage at the other two electrodes as can be seen in the image. By maintaining the potential at the working electrode (c), that at the counter or auxiliary electrode (a) can then be adjusted with respect to the reference electrode (b). Image from Amatucci *et al.*<sup>3</sup> . . . . . 41
- 21 X-ray diffraction patterns for samples prepared through solvothermal synthesis. Samples were ground and mounted in an aluminium sample holder. Samples were prepared at 180°C for (a) 12 hours (b) 24 hours and (c) 48 hours. It can be seen that for the sample synthesised over 12 hours is very different from the other two data sets, indicating that 12 hours is not long enough at 180°C to produce VO<sub>2</sub>(B). The other two data sets show very little change indicating that VO<sub>2</sub>(B) can be synthesised after just 24 hours, rather than 48 hours. . . . . 51

- 22 X-ray diffraction pattern of  $\text{VO}_2$  prepared through solvothermal synthesis of  $\text{V}_2\text{O}_5$  which is reduced by formaldehyde in a Parr bomb for 48 hours at  $180^\circ\text{C}$ . Samples were ground and mounted in an aluminium sample holder. Rietveld refinement was performed on the data collected, using a structural model of Oka *et al.*<sup>1</sup> The black circles represent the data, the red curve represents the model the data were fitted to and the blue curve represents the difference between the data and the model. . . . . 54
- 23 Scanning electron microscopy images of samples prepared via solvothermal synthesis at varying reaction times. Samples were synthesised at  $180^\circ\text{C}$  for (a) 24 and (b) 48 hours. There is a noticeable thickening of the rods with increasing time. . . . . 55
- 24 X-ray diffraction pattern of  $\text{VO}_2(\text{B})$  prepared via microwave synthesis using  $\text{V}_2\text{O}_5$  and formaldehyde at  $180^\circ\text{C}$  for (a) 1 hour (b) 3 hours and (c) 6 hours. Samples were ground and mounted in an aluminium sample holder. There is a noticeable change in the X-ray diffraction patterns as the time of the reaction is increased. The widening of the peaks within (b) could be due to it having a more nanosized phase than (a) and (c). . . 57
- 25 X-ray diffraction pattern of  $\text{VO}_2(\text{B})$  prepared via microwave and solvothermal synthesis using  $\text{V}_2\text{O}_5$  and aqueous formaldehyde at  $180^\circ\text{C}$ . Samples were ground and mounted in an aluminium sample holder. (a) is the 6 hour microwave synthesis run and (b) is the 48 hour solvothermal synthesis experiment. Both patterns appear very similar in appearance indicating that the 6 hour microwave synthesis run has produced  $\text{VO}_2(\text{B})$ . 59

- 26 X-ray diffraction pattern of  $\text{VO}_2(\text{B})$  prepared via microwave synthesis using  $\text{V}_2\text{O}_5$  and aqueous formaldehyde at  $180^\circ\text{C}$  for 6 hours. Samples were ground and mounted in an aluminium sample holder. The data have been fitted using a Rietveld refinement, using the data from Oka *et al.*<sup>1</sup> as the model. The black circles represent the data, the red curve represents the model the data were fitted to and the blue curve represents the difference between the data and the model. . . . . 61
- 27 Scanning electron microscopy images of samples prepared via microwave synthesis at varying reaction times. Samples were prepared at  $180^\circ\text{C}$  for (a) – (c) 1 hour, (d) – (f) 3 hours and (g) – (i) 6 hours. There is a noticeable change in particle morphology and assembly with increasing time. . . . . 63
- 28 X-ray diffraction pattern of  $\text{VO}_2(\text{B})$  prepared via microwave synthesis using  $\text{V}_2\text{O}_5$  and formaldehyde for 1 hour at (a)  $150^\circ\text{C}$  (b)  $180^\circ\text{C}$  and (c)  $200^\circ\text{C}$ . Samples were ground and mounted in an aluminium sample holder. As the temperature increases it can be noticed that there is a change of phase present. (b) and (c) are more similar than that of (a) which shows that the reaction progresses quicker with a higher temperature. 66
- 29 Scanning electron microscopy images of samples prepared via microwave synthesis at varying reaction temperatures. Samples were prepared over one hour at (a) – (c)  $150^\circ\text{C}$ , (d) – (f)  $180^\circ\text{C}$  and (g) – (i)  $200^\circ\text{C}$ . There is a noticeable change in particle width and length with increasing temperature. . . . . 67
- 30 X-ray diffraction patterns showing products after  $\text{NH}_4\text{VO}_3$  being used as the starting vanadate and using formaldehyde. Samples were ground and mounted in an aluminium sample holder. Synthesis was carried out in a PTFE lined Parr bomb cell. The reaction times were varied to see if there was any significant difference. (a) refers to the run carried out over 12 hours, (b) is for 24 hours and (c) was carried out over 48 hours. 71

- 31 X-ray diffraction pattern of  $\text{VO}_2(\text{B})$  synthesised in a PTFE lined Parr bomb cell with aqueous formaldehyde. Samples were ground and mounted in an aluminium sample holder. Reactions were carried out with different starting vanadates,  $\text{V}_2\text{O}_5$  and  $\text{NH}_4\text{VO}_3$  being used, and the reaction times were both over 48 hours. (a) refers to use of  $\text{NH}_4\text{VO}_3$  and (b)  $\text{V}_2\text{O}_5$  . . . . . 72
- 32 X-ray diffraction pattern of  $\text{VO}_2(\text{B})$  synthesised using  $\text{NH}_4\text{VO}_3$  and formaldehyde as the starting materials. Samples were ground and mounted in an aluminium sample holder. (a) was carried out using microwave synthesis for  $180^\circ\text{C}$  for 6 hours. (b) was carried out in a PTFE lined Parr bomb cell at  $180^\circ\text{C}$  for 48 hours. . . . . 73
- 33 Charge and discharge curve for  $\text{VO}_2(\text{B})$  at a discharge rate of  $\text{C}/10$ . The battery was cycled from 2.0 to 3.0V and the redox potential plateau lies at 2.73V. Cycling was carried out under standard ambient conditions ( $25^\circ\text{C}$  and 100k Pa). Colours are used to represent different cycles. . . . 76
- 34 (a) XANES, (b) EXAFS data and (c) Fourier transform of EXAFS data for  $\text{VO}_2(\text{B})$ . In (a), a pre-edge feature is located at 5480 keV. The doublet noted at 5486 and 5489 keV is a feature found for the  $\text{V}^{4+}$  oxidation state. (b) shows the chi data extracted from the averaged EXAFS data, while (c) shows the Fourier transform of this data. The Fourier transform of the EXAFS (c) reveals nearest neighbour bond distances. Here, the peak at 1.500 Å is for a V–O bond, while the two peaks at 2.44 and 3.031 Å are for the alternating short and long bond distances expected for  $\text{VO}_2(\text{B})$ .<sup>1</sup> . . . . . 78

35	XANES data of VO <sub>2</sub> (B) Bellcore film in a lithium-ion battery cell. Unfortunately, unlike the Powder data, there is a barium peak in the EXAFS region at 5640 eV, due to the presence of a barium impurity in the battery separator. This makes it impossible to analyse this region and obtain EXAFS data. The XANES profile is the same as the powder results (see Figure 34). . . . .	79
36	Experimental set-up of the battery cell at the B18 Quick EXAFS beamline at the Diamond Synchrotron source. The synchrotron radiation entered from the right hand side of the image, travelled through the cell and out the other side. . . . .	80
37	XANES data collected during a cycle, with (a)–(h) representing different points on the charge–discharge cycle (see Figure 39). The data show that there is a big change in the XANES region, most notably the first peak. . . . .	81
38	Highlighted XANES region of the V K-edge during the VO <sub>2</sub> (B) cycle. The data start at (a) and end with (h) and it can be seen that the initial peak goes from having a shoulder to being just one peak. (a) to (h) represent the spectra recorded for points on the corresponding charge–discharge curve. The change in peak positions and shape are due to changes in the VO <sub>2</sub> (B) structure, due to the movement of lithium atoms and electrons. . . . .	82
39	Charge–discharge cycle showing one dynamic cycle of the VO <sub>2</sub> (B) Bellcore film. The point on the curve related to XANES data collected during the cycle, which were shown in Figure 38. Data was collected at 3 minute intervals every 30 minutes. . . . .	83
40	XRD pattern of LiFePO <sub>4</sub> synthesised using microwave-assisted solvothermal methods. Comparison of this pattern with the reference pattern for LiFePO <sub>4</sub> showed a good correspondence in peak positions. <sup>4</sup> . . . . .	86

- 41 Scanning electron microscopy images displaying the morphology of  $\text{LiFePO}_4$ . (a) is least magnified at 60x. Here it can be seen that the sample looks almost powder-like in appearance. As the magnification increases, ((b) 250x) it can be seen that super-structures are being formed with a flocculant appearance. From this magnification they could be flakes or spherical aggregates. (c), 20kx, displays that the particles synthesised are nanoflake in morphology, with a width of approximately 0.5, length of 1 and a thickness of 0.1  $\mu\text{m}$ . . . . . 88
- 42 Cycling data for  $\text{LiFePO}_4$  showing charge-discharge patterns between 4.2 V and 2 V. The cycle starts at black by discharging before then charging. Cycling experiments were carried out by Dr S. Corr and associates in Amiens, France. . . . . 90
- 43 EXAFS and XANES data demonstrating the local structure of  $\text{LiFePO}_4$  and Fourier transform of the XANES data enabling bond lengths to be distinguished. The EXAFS and XANES spectra, (a), show that the pre-edge peak is at 7111 eV with two more peaks at 7126 and 7172 eV. The peak on the Fourier transform (b) at 1.533 Å shows Fe-O bonding and the peaks at 2.692 and 3.635 Å are associated with the higher shell bonding between the iron, phosphorus and oxygen . . . . . 91
- 44 X-ray diffraction pattern of  $\text{LiCoPO}_4$  synthesised using  $\text{Co}(\text{NO}_3)_2 \cdot 6\text{H}_2\text{O}$  and  $\text{LiH}_2\text{PO}_4$  dispersed in ethylene glycol, and solvothermally treated in a microwave oven at 300°C for 2 hours. Comparison of this pattern with the reference pattern for  $\text{LiCoPO}_4$  showed a good correspondence in peak positions.<sup>5</sup> . . . . . 93
- 45 Scanning electron microscopy images displaying the morphology of  $\text{LiCoPO}_4$ . The images reveal that a crystalline material has been formed. There is however a broad size distribution. . . . . 94

46	Cycling data for $\text{LiCoPO}_4$ showing charge–discharge patterns between 4.2 V and 2 V. The cycle starts by discharging displayed by the black line prior to being charged. Cycling experiments were carried out by Dr S. Corr and associates in Amiens, France. . . . .	95
47	EXAFS and XANES data demonstrating the local structure of $\text{LiCoPO}_4$ . Also showing the chi data and Fourier transform of the XANES data enabling bond lengths to be distinguished. On the EXAFS and XANES spectra, (a), the pre–edge can be found at 7710 eV, with the first peak at 7725 eV. (c), the Fourier transform, shows the bond lengths present. 1.477 Å shows the Co–O bonding where as 2.436 Å, 3.158 Å and 3.639 Å represent the bonding in the higher shells between the cobalt, phosphorus and oxygen. . . . .	96
48	X–ray diffraction pattern of $\text{LiMnPO}_4$ synthesised using $(\text{CH}_3\text{COO})_2\text{Mn}\cdot 4\text{H}_2\text{O}$ and $\text{LiH}_2\text{PO}_4$ dispersed in ethylene glycol, and solvothermally treated in a microwave oven at 300°C for 2 hours. Comparison of this pattern with the reference pattern for $\text{LiMnPO}_4$ showed a good correspondence in peak positions. <sup>6</sup> . . . . .	98
49	SEM images displaying the morphology of $\text{LiMnPO}_4$ at varying magnifications. (a) shows that the sample is clustered into structures with a poorly defined outline. (b) gives the appearance of a flake–like structure to the sample. (c) shows that the sample is more needle–like in morphology than flake–like. . . . .	99
50	Cycling data for $\text{LiMnPO}_4$ showing charge–discharge patterns between 4.2 and 2 V. Cycling experiments were carried out by Dr S. Corr and associates in Amiens, France. . . . .	100

- 
- 51 EXAFS and XANES data demonstrating the local structure of  $\text{LiMnPO}_4$ . Also showing the chi data and Fourier Transform of the XANES data enabling bond lengths to be distinguished. (a) shows the EXAFS and XANES data collected. The pre-edge can be found at 6540 eV with the main peak at 6552 eV and a second peak at 6560 eV. The Fourier transform is showed in (c). This shows the bonding within the  $\text{LiMnPO}_4$ . The peaks shown are at 1.617 Å, the Mn – O bond, and 2.612 Å, 3.220 Å and 3.705 Å represent the bonding in the higher shells between the manganese, phosphorus and oxygen. . . . . 101

## List of Tables

1	Amounts of sample added to boron nitride for EXAFS experiment pellets	47
2	Lattice parameters from the Rietveld refinement performed on VO <sub>2</sub> (B) synthesised over a 48 hour period using V <sub>2</sub> O <sub>5</sub> and formaldehyde as the reactants; the model uses data from Oka <i>et al.</i> <sup>1</sup> . . . . .	53
3	Lattice parameters from the Rietveld refinement performed on the VO <sub>2</sub> (B) synthesised over a 48 hour period in the Parr bomb cell and also by the 6 hour microwave oven run using V <sub>2</sub> O <sub>5</sub> and formaldehyde as the reactants. The model uses data from Oka <i>et al.</i> <sup>1</sup> . . . . .	62

# 1 Introduction

## 1.1 General introduction

The increased performance demands on current batteries continue to propel research on cathode materials to meet the needs of mobile technologies. Other areas of interest for rechargeable batteries include electric vehicles and renewable energies, where the generated power needs to be stored or it is lost. Batteries consist of one or more cells where chemical energy is converted into electricity, to be used as a power source. These electrochemical cells can be connected in parallel and or in series with each other to provide either the required capacity or voltage, respectively. The chemical reaction that occurs in the battery happens at two electrodes within the cell, a positive cathode and a negative anode. These electrodes are separated by an electrolyte solution, which enables the transfer of ions between the two electrodes due to the dissociated salts within it.<sup>7</sup> The conversion of chemical energy into electricity occurs once the two electrodes are connected externally via a load. Chemical reactions occur simultaneously at both of the electrodes through reduction and oxidation reactions ('redox'), releasing electrons and enabling a current which is then used to drive the load.<sup>8</sup> A load in this context is an object that requires a voltage and/or current and completes the circuit.

## 1.2 Types of battery

Primary batteries are the main type of battery in commercial use currently. This type of battery is a single use battery, which cannot be recharged. The main advantage of a primary battery is its convenience, as you can just place it in the device without worrying about charging it. However, whereas short term cost is low, they have a higher cost when compared with secondary batteries over the lifetime of a device. They are also not suitable for high drain products due to their short lifetime and they require constant replacement, causing far more waste than secondary batteries.

Secondary batteries are rechargeable batteries. Their main advantage over primary batteries is their cost effectiveness over the lifetime of the device they are powering. They have a lower capacity and initial voltage when compared to primary batteries, but display a flat discharge curve meaning that there is an even distribution of charge throughout the discharge process. A discharge curve is a graphical representation of the voltage level within a battery as it drops off through use. They are better for high drain products such as cameras and mobile phones, as they have a slower discharge and can be recharged when the battery runs low. High drain here refers to a load that requires a lot of power to function. The capacity of a cell is related to the amount of electrode material within the cell, the more of these there are, the greater the capacity of the cell.<sup>9</sup> Examples of secondary batteries include the lead–acid battery,<sup>10, 11</sup> nickel–cadmium batteries,<sup>12</sup> nickel–metal hydride batteries<sup>13,14</sup> and lithium–ion batteries.<sup>8,15–17</sup>

### **1.2.1 Lead–acid batteries**

Gaston Planté developed the lead–acid battery, which was the first type of rechargeable battery.<sup>18</sup> The battery consists of lead and lead(IV) oxide electrodes, with sulfuric acid as the electrolyte. This type of battery is most commonly associated with cars due to the high surge currents that it can create which is perfect for the starter motor. The main problems with lead–acid batteries are that they are big and bulky and contain lead which is highly toxic and can cause poisoning through ingestion.

### **1.2.2 Nickel–cadmium and nickel metal hydride batteries**

Nickel–Cadmium, or Ni–Cad, as the name suggests, uses nickel and cadmium as the electrodes. It was first reported in 1899 by Waldemar Junger. At the time, this was the only direct competitor to the lead–acid battery. Due to its smaller size and with minor improvements to the cathodes, Ni–Cad batteries soon rapidly increased their energy density to beyond that of lead–acid batteries and close to those of primary batteries.

Energy density is a term used to describe the amount of energy that is stored within a given region of space per unit mass.<sup>19</sup> One problem with nickel–cadmium batteries is however their toxic materials.

Nickel–metal Hydride (NiMH) first appeared on the market in 1989 and offered an increased energy density when compared to Ni–Cad and lead–acid batteries.<sup>14</sup> They work on the same principles as Ni–Cad, with nickel oxyhydroxide employed as the positive electrode. The cadmium is replaced with a hydrogen absorbing alloy for the negative electrode. It has been widely accepted that nickel–metal hydride are the interim step up to lithium–ion battery technology. NiMH batteries, when compared with lithium–ion batteries, have an far inferior nominal voltage and also they have a much higher rate of self discharge. Nominal voltage is the average voltage produced by the cell, and self discharge is the amount that a cell discharges charge on its own, without being connected to a circuit. Recent development of low self discharge NiMH batteries have aimed to tackle this, but at the cost of a lowered capacity.<sup>20</sup>

### 1.3 Development of lithium–ion (Li–ion) batteries

Battery chemistry has been improving rapidly to cope with the ever–increasing power demands of newly emerging devices including mobile phones, cameras and laptops.<sup>21</sup> Lithium–ion batteries have recently become the major source of power for the portable electronic market, since first released commercially by Sony in 1991.<sup>22</sup> They consist of a lithium containing metal oxide as the cathode and a carbonaceous anode, usually graphite. A few examples of metal oxides are  $\text{CoO}_2$ ,  $\text{Mn}_2\text{O}_4$  and  $\text{FePO}_4$ .<sup>23</sup> All of these can play host to lithium ions which may intercalate and de–intercalate into the metal oxide structure.

Current lithium–ion battery technology uses  $\text{LiCoO}_2$  cathodes (shown in Figure 1) but these only utilise around 50% of the theoretical capacity, as well as cobalt being both toxic and expensive.<sup>24</sup> It was initially thought that using a layered  $\text{LiNiO}_2$  would be best

for the cathode within a lithium-ion battery cell, due to it having a more favourable specific capacity than that of cobalt dioxide.<sup>25</sup> However, exothermic oxidation of the organic electrolyte, following the collapse of the NiO<sub>2</sub> structure post-delithiation, led to safety problems and the expectations could not be reached.<sup>16</sup>

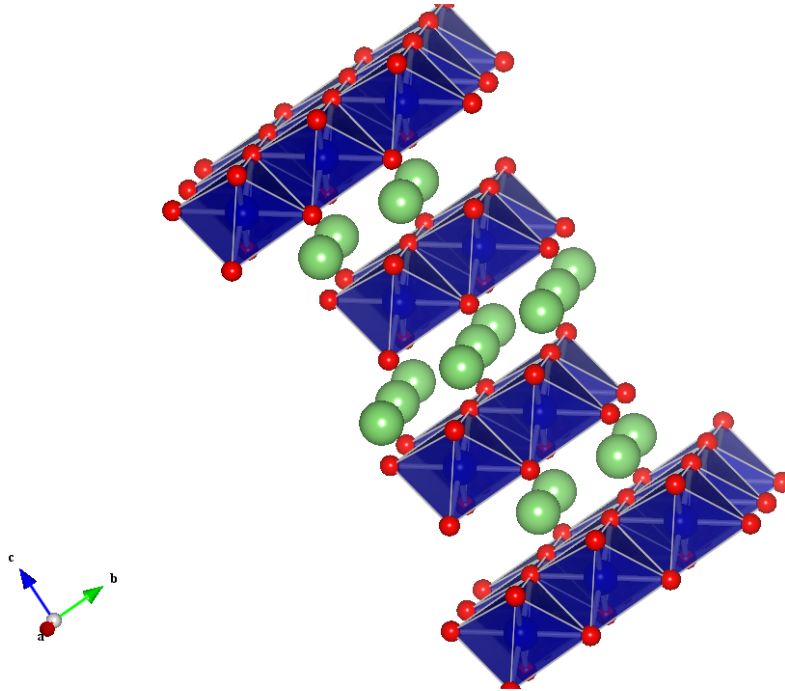
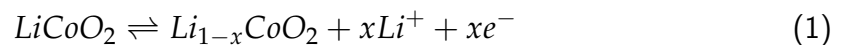


Figure 1: Crystal structure of LiCoO<sub>2</sub>, which is commonly used as a cathode material. The lithium ions, shown in green, occupy channels in the structure.

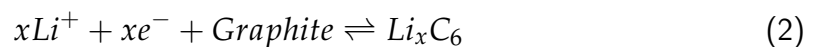
### 1.3.1 Charging and discharging processes

To use LiCoO<sub>2</sub> as an example, the charging and discharging processes can be displayed as half reactions at both the cathode and the anode. These are as follows:

Cathode half equation:



Anode half equation:



The top half equation shows the reaction at the metal oxide cathode, in this case  $\text{CoO}_2$ . The forward reaction is the charging process. During charging, lithium ions and electrons are extracted from the cathode and enter the electrolyte; the reverse happens during discharge. The second equation shows the reaction at the graphite anode. Again, the forward reaction is the charging process. The lithium ion and electron that have been liberated from the cathode in the previous reaction interact with the anode and intercalate with the carbon. During discharge, the lithium ions and electrons de-intercalate from the carbon anode and re-enter the electrolyte.

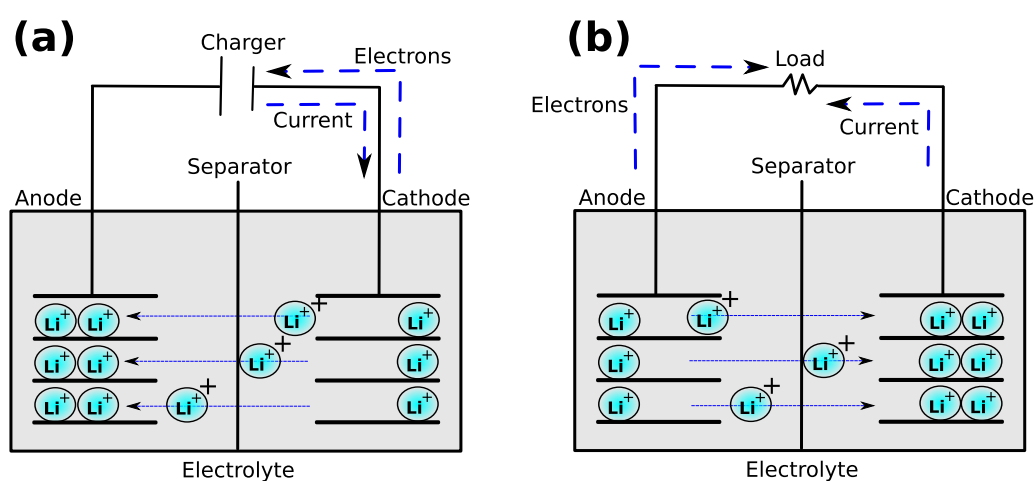


Figure 2: Graphical representation of the charging and discharging processes of a lithium-ion battery. As the battery is charged, (a), lithium ions and electrons leave the cathode and move towards the anode and charger respectively. During discharging, (b), the lithium ions and electrons leave the anode and move towards the cathode and load respectively.

### 1.3.2 Synthesis Methods

There are many methods of synthesising cathode materials for lithium-ion batteries, the most common of which are summarised below.

**1.3.2.1 Solid-state Synthesis** Solid-state synthesis is a solvent-less reaction. Starting materials are ground together and then sintered in a tube furnace at high temperatures.<sup>26,27</sup> This high thermal activation temperature is due to otherwise very low diffusion coefficients. As the materials begin to react, the product is formed at the reaction interface. As the reaction proceeds, the increase of product at this interface will limit the diffusion rate of the starting materials and slow down the reaction. Eventually, the reaction will have to be stopped, and the product reground, and placed back into the furnace to increase the contact between the remaining starting materials, as shown in Figure 3.<sup>27</sup>

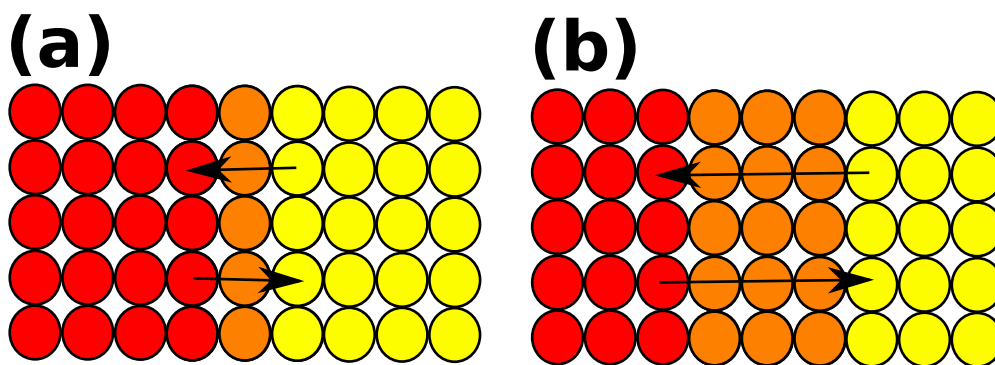


Figure 3: Schematic representation displaying the evolution of product over time during solid-state synthesis. (a) The interface (orange) where the product forms between the reactants (red, yellow) is small at the start of the reaction. (b) As the reaction progresses, the interface between the two reactants increases as the amount of product increases. This increase in interface and product slows down the reaction due to the increased distance that the reactants have to travel to interact with each other. To limit this, the synthesis is stopped, the sample reground, and placed back into the furnace.

**1.3.2.2 Solvothermal Synthesis** Solvothermal syntheses are carried out in closed systems, in many cases a PTFE-lined Parr bomb, which is then placed within an oven and heated. The starting materials are placed, along with a solvent, into the bomb and are allowed to react at elevated temperatures and pressures. Solvothermal synthesis permits

control over the size, shape, monodispersity and crystallinity of the products by variation of the experimental parameters (temperature, time, solvent, surfactant, precursor type, etc).<sup>28</sup> This synthesis requires lower temperatures than that of solid–state synthesis, and has shorter reaction and preparation times, however, due to thermodynamics, all products will still have some defects.<sup>28</sup>

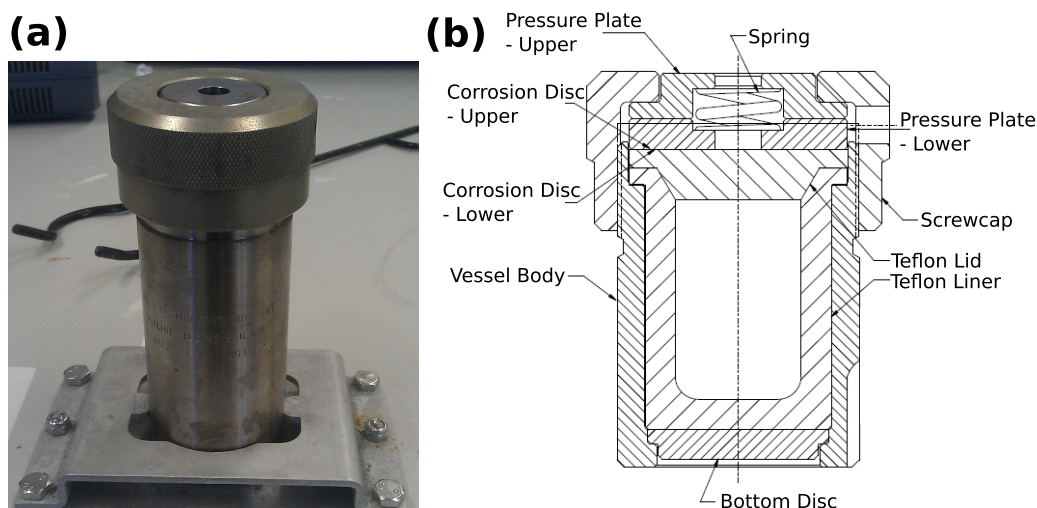


Figure 4: Graphical representation of (a) a solvothermal bomb and (b) the bomb components. The bomb is designed to allow pressure to build up, but also be released safely if it becomes too high. The reactants are placed within the PTFE liner and the lid placed upon it. Making sure the bottom disc is in correctly, the PTFE liner is then placed within the vessel body. The lower and upper corrosion discs are then placed on top of the PTFE lid and the lower pressure plate added onto that. To finish off, a spring is placed in with the upper pressure plate placed on it, and then the screw cap lid tightened on to maintain a tight seal for the Parr bomb.

**1.3.2.3 Microwave Synthesis** Microwave ovens may be used in conjunction with solvothermal synthesis, in a process known as microwave–assisted solvothermal synthesis. Instead of using an oven to heat the autoclave, the reactants are placed within a microwave oven boiling tube and placed within the microwave oven cavity. Microwave

energy, a type of electromagnetic radiation, possesses an electric and a magnetic component. The electric component interacts with water and organic molecules and creates heating in the reaction mixture. Microwave oven heating does not have sufficient local energy to make or break chemical bonds, but does have enough to affect molecular rotation. Microwave energy is not breaking or breaking bonds, but instead applying energy directly to the molecules.<sup>29</sup>

Microwave energy can be converted into heat through one of two mechanisms, dipole rotation and ionic conduction. The mechanism used in an experiment is dependent upon the the reactants that will be exposed to microwave radiation. If a molecule is exposed to microwave field and it has a dipole moment, then the dipole of the molecule will attempt to align itself with the electromagnetic field. As the dipoles align themselves, they cause heating through interactions with neighbouring molecules. This is dipole rotation.<sup>29</sup> If a sample contains ions in the reaction mixture, then the ions will move through the solution in the direction of the electric field, causing heat through friction as they pass. This is known as the ionic conduction mechanism.<sup>29</sup>

Heating through the use of microwave radiation is more efficient than thermal heating in a Parr bomb; as the microwaves can directly interact with different species within a reaction, the energy is transferred directly to the components of the reaction mixture. Thermal heating, however, requires the energy to pass through different media such as the reaction vessel and the solvent before interacting with the reaction components.<sup>30</sup>

There is also more control when using a microwave oven when compared to Parr bomb, as the radiation strength is easily changeable, and the temperature and pressure can also be monitored. It is also possible to stir the sample during the reaction, making sure that nothing settles and making the reaction more homogeneous and being more pure than solvothermal synthesis. With the addition of an auto-sampler, many runs can be carried out one after the other in like manner, increasing the throughput of samples for testing.<sup>30</sup> The use of a wave source for synthesis therefore allows the reaction time to be brought down further and purity of the product to be increased, whilst maintaining

the temperature and pressure of a normal conductive heating method.<sup>30</sup> Figure 5 shows an image of the microwave oven synthesiser employed in this thesis.



Figure 5: Image of the microwave oven synthesiser used for the experiments within this thesis.

### 1.3.3 Cathode materials for lithium-ion batteries

**1.3.3.1 Current technologies** For lithium-ion batteries, the most commonly used cathode in mass production is  $\text{LiCoO}_2$ .<sup>31,32</sup> This has a theoretical capacity of 272 mAh/g, although upon cycling between 3 and 4.2 V the reversible capacity is lowered to 140 mAh/g. This equates to around 0.5 lithium ions per  $\text{LiCoO}_2$  ( $\text{Li}_{0.5}\text{CoO}_2$ ). To increase the capacity, a voltage higher than 4.2 V is required, but, this can sometimes result in a rapid capacity loss.<sup>31</sup>

$\text{LiCoO}_2$  has a layered structure with rhombohedral symmetry (see Figure 1). The crystal structure contains a closely-packed arrangement of oxygen ion layers, alternately interspersed with lithium and cobalt ions layers occupying octahedral sites.<sup>33</sup> This permits

rapid lithium intercalation and de-intercalation into or from the  $\text{Li}_x\text{CoO}_2$  with  $x$  lying in the range 1 to 0.5.<sup>34</sup>

Thin film  $\text{LiCoO}_2$  electrodes can be prepared through various techniques such as radio frequency sputtering (rf),<sup>35–38</sup> pulsed laser deposition (PLD),<sup>34,39</sup> sol-gel coating,<sup>40</sup> chemical vapour deposition,<sup>41</sup> electrostatic spray deposition<sup>42</sup> and spin coating.<sup>43</sup> Of these, the most commonly used techniques for synthesising  $\text{LiCoO}_2$  are rf sputtering and PLD.<sup>39</sup>

**1.3.3.2 Olivine-based structures** Transition metal phosphates have been developed as a potential new class for cathodes in lithium-ion batteries (see Figure 6). Examples include  $\text{LiMPO}_4$  (where M is one of Fe, Mn, or Co),  $\text{Li}_3\text{V}_2(\text{PO}_4)_3$ ,<sup>44</sup> and  $\text{LiVPO}_4\text{F}$ .<sup>45</sup> These are promising materials since they all contain both mobile lithium ions and also redox-active transition metals, both within a rigid phosphate network. They also all show great stability both thermally and electrochemically, while maintaining equivalent energy densities when compared to metal oxide cathodes. There are a few problems, however, with transition metal phosphates. One of these is that they have poor electrical conductivity and this means that the migration kinetics of the lithium ions and electrons will be affected during the electrochemical reaction and hence influence the charging and discharging capabilities of the electrodes when tested.<sup>46</sup>

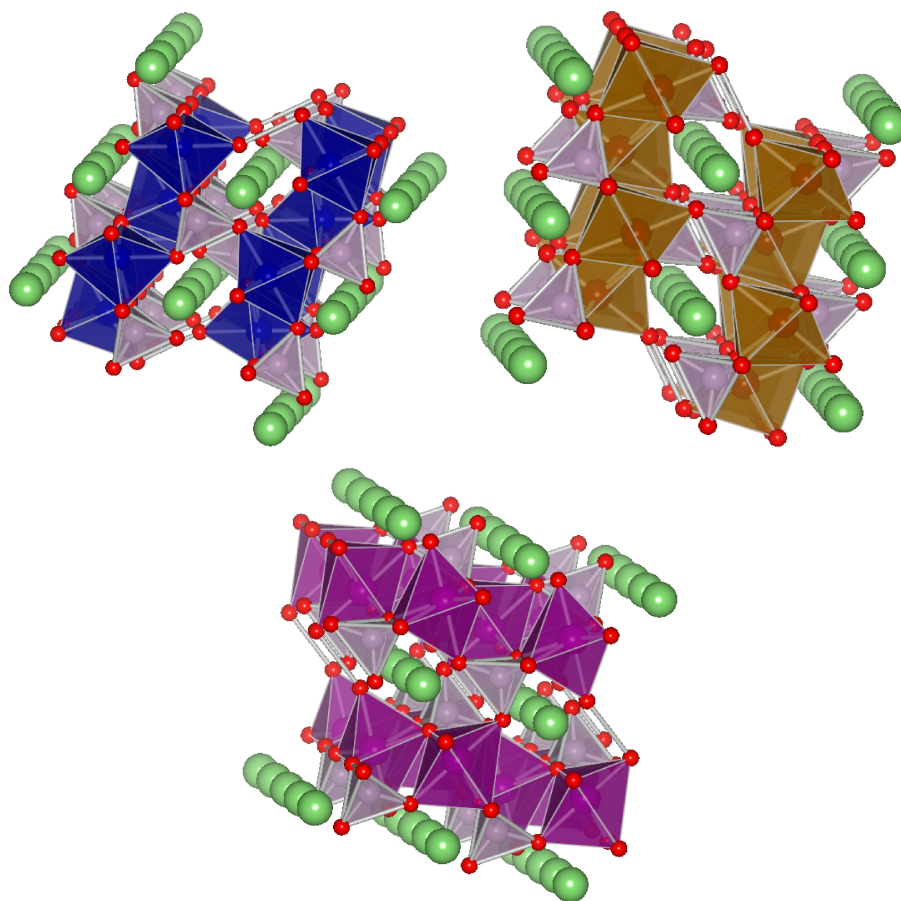


Figure 6: Structural representations of the olivine structures (a)  $\text{LiCoPO}_4$ , (b)  $\text{LiFePO}_4$  and (c)  $\text{LiMn}_2\text{O}_4$ , which are promising battery cathode materials. Common to each of these structures is an open framework, where the lithium ions (shown here in green) occupy channels in the structure.

Functional properties of lithium-ion battery cathodes are influenced by many factors. Having a 1-D nanostructure, if "pure", is advantageous due to improved charge transport.<sup>47</sup> This is an advantage that nanostructures have over materials with a bulk crystalline structure.<sup>8</sup> There are many other benefits to the use of nanostructures within a lithium-ion rechargeable battery when compared with bulk materials. One of these is the increased surface area created by having nanomaterials. With an increased surface area, there is more contact with the electrolyte, leading to greater electrode electrolyte interaction. There have also been reports of enhanced performance when dimensions

are reduced to nanoscale,  $\text{LiFePO}_4$  is an example of this.<sup>48</sup>  $\text{LiFePO}_4$  is a poor electronic conductor. When nanosized, it has a shorter diffusion path length for lithium-ion transport, which enhances the rate capability and power density. Nanostructured materials also have an improved life cycle due to improved support of the strain from lithium intercalation. Another advantage is the better electrochemical use of the materials due to their smaller size.<sup>48</sup>

Doping the metal oxide cathode material with a limited amount of a secondary phase is another route to improving cathode performance. Yang *et al.* did just this by doping  $\text{LiFePO}_4$  with ruthenium.<sup>49</sup> Their tests showed that through doping with ruthenium, a higher specific capacity can be achieved. It was also shown to have a preferable cycling performance. XRD patterns showed that the structure is then slightly constricted, but this was to be expected as it happens with all cases of doping. Data collected from cyclic voltammetry and electrochemical impedance spectroscopy showed that the Ru-doped  $\text{LiFePO}_4/\text{C}$  cathode had a more stable structure, enhanced diffusion coefficient and conductivity of  $\text{Li}^+$ ;  $\text{Ru}^{3+}$  is considered to act as support for the lattice, preventing the crystal from collapsing during charge-discharge cycling.

Cobalt doping has also been used in  $\text{LiNiO}_2$  and  $\text{LiMnO}_2$ .<sup>50,51</sup> When used with  $\text{LiFePO}_4$  however, high levels of cobalt doping led to a decrease in performance, and low-level doping led detectable improvements in capacity, performance and stability whilst cycling, as there is enhanced electronic capacity and increased mobility of the lithium ions.<sup>52</sup> Recent studies have been carried out by doping  $\text{Li}_3\text{V}_{2-x}\text{Co}_x(\text{PO}_4)_3$  with cobalt.<sup>53</sup> It was found that when the cobalt was added, the specific capacity initially dropped, but as the amount of cobalt within the structure was increased so did the specific capacity. When the  $\text{Co}^{2+}$  doping reached  $x=0.15$ , the capacity returned to that of the unsubstituted  $\text{Li}_3\text{V}_2(\text{PO}_4)_3$  phase. Following 50 cycles it was found that the cobalt doping did result in improving cell cycle-ability.

$\text{LiVOPO}_4$  was tested by Zhou *et al.* to see if it could rival the other transition metal cathodes.<sup>54</sup> Compared to  $\text{LiFePO}_4$ , which has a similar theoretical specific capacity,

$\text{LiVOPO}_4$  was found to have a higher charge–discharge plateau of around 4.0V when used as a cathode material. It was then compared to  $\text{Li}_3\text{V}_2(\text{PO}_4)_3$ , which has the highest theoretical of all the transition metal phosphates. It was found that  $\text{LiVOPO}_4$  has only one charge–discharge plateau, which can help its utilisation for practical use within lithium–ion batteries. The only problem is that it has a poor electrochemical performance due to the low lithium ion diffusion and electrical conductivity. It was then tested using carbon as a coating to try and improve the electrochemical performances, with little success. They then tried using  $\text{RuO}_2$ , which has been noted in other studies to increase performances of other lithium–ion battery materials, to create a  $\text{LiVOPO}_4/\text{RuO}_2$  composite. Their findings showed that electrical conductivity and lithium–ion diffusion were increased due to the presence of the highly electronic  $\text{RuO}_2$ .

**1.3.3.3 Vanadate structures** Vanadium and its oxides have also been considered as possible lithium–ion cathode materials. Vanadates are a very diverse family of compounds, with many oxidation states. These oxidation states enable vanadates to form a multitude of structure forms with various types of coordination polyhedra such as tetrahedra, trigonal bi–pyramids, square pyramids, regular octahedra, and distorted octahedra.<sup>55</sup> Each has its own benefits towards a different area of science, for example use within catalysis, lithium–ion batteries, chemical sensors and electrochemical and optical devices.<sup>56</sup> For example, bronze phase  $\text{VO}_2$  ( $\text{VO}_2(\text{B})$ ) is potentially a lithium–ion battery cathode due to its affinity for lithium intercalation,<sup>47,57</sup> whereas rutile  $\text{VO}_2$  ( $\text{VO}_2(\text{R})$ ) undergoes a metal–insulator transition at around 340K, which makes it ideal for optical switching devices.<sup>58,59</sup>

Vanadium oxides therefore represent a promising class of materials for battery applications, due to their low toxicity, high availability, low cost and multitude of oxidation states. Vanadium oxides are prone to structural collapses following repeated charges and discharges, and therefore to capacity deterioration.<sup>60</sup> Vanadium pentoxide ( $\text{V}_2\text{O}_5$ ) was one of the first cathode materials proposed for rechargeable lithium batteries.<sup>61</sup> Chung

*et al.* tested a modified version of  $V_2O_5$  by adding 3–3.5% of sodium orthosilicate. This was then heated and rapidly cooled to room temperature. The resulting material was then tested as an active cathode material for lithium batteries through charge–discharge tests. After the first discharge it developed an amorphous character, but upon further charging it showed excellent recharge–ability in the potential range of 1.5–3.9V.<sup>62</sup>

$VO_2(B)$  has a structure that is built up of distorted  $VO_6$  octahedra, which share both corners and edges.<sup>57</sup>  $VO_2(B)$  is a metastable phase. It has a layered structure which is ideal for a battery cathode as it is easier to lithiate. Tests have shown that  $VO_2(B)$  has a maximum reversible capacity of around 320 mAh/g, more than twice that of  $LiCoO_2$ , the current preferred lithium–ion battery cathode. This makes  $VO_2(B)$  a possible future cathode given its electrochemical, economical and environmental advantages.<sup>57</sup>

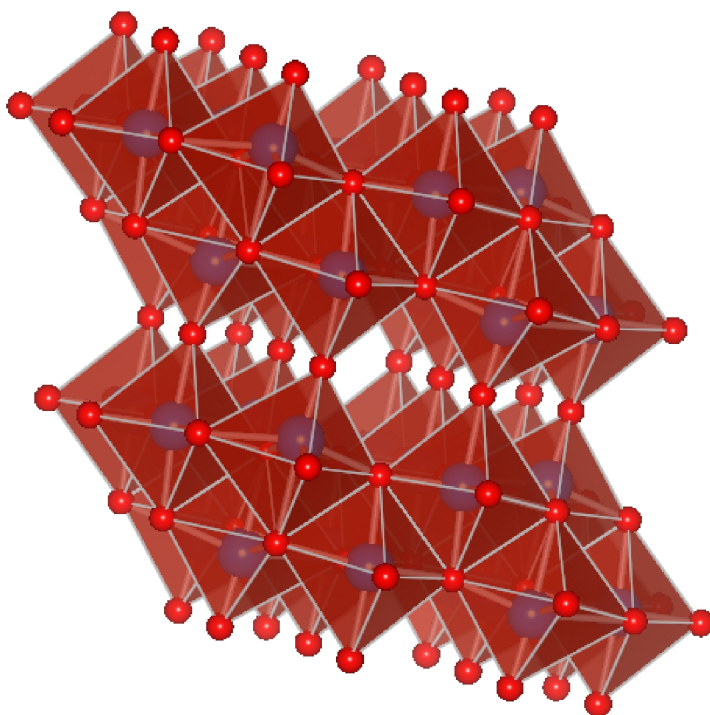


Figure 7: Structure of  $VO_2(B)$ . The red atoms represent oxygen and the blue vanadium atoms. The channels that can be seen within the structure are the pathways taken by lithium ions. Observing from different angles, there can be seen many pathways available for the lithium ions.<sup>1</sup>

Some methods of vanadium oxide synthesis include sol-gel reaction followed by hydrothermal treatment.<sup>56</sup> VO<sub>2</sub>(B) can also be synthesised through thermal reduction of V<sub>2</sub>O<sub>5</sub> by H<sub>2</sub> or SO<sub>2</sub> gas. This led, however, to the formation of only bulk VO<sub>2</sub>(B). More modern techniques have been able to synthesise VO<sub>2</sub>(B) with a 1-D nanostructure for example nanowires and nanorods, ideal for battery cathodes.<sup>57</sup>

Chen *et al.* used V<sub>2</sub>O<sub>5</sub> and cetyltrimethylammonium bromide (CTAB) and reacted them for 48 hours through solvothermal synthesis in an autoclave. The product, which was characterised to be VO<sub>2</sub>(B), was then cycled in the range 3.6 to 1.5 V and found to have a reversible capacity of around 306 mAhg<sup>-1</sup>, which corresponds to the insertion of 1 Li into Li<sub>x</sub>VO<sub>2</sub> and a reduction of some V<sup>4+</sup> to V<sup>3+</sup>. This is a lot better than VO<sub>2</sub> in bulk, which has a reversible capacity 160 mAhg<sup>-1</sup>. After 15 cycles the VO<sub>2</sub>(B) had a specific capacity of 245 mAhg<sup>-1</sup>, which then had a 35% capacity decline post 15 cycles. Therefore VO<sub>2</sub>(B) nanorods formed in this way can maintain 80% of its initial capacity, which is good cycling behaviour for a potential future lithium-ion rechargeable battery cathodes.

Another method, carried out by Pavasupree *et al.* in 2005, used laurylamine hydrochloride (LAHC), acetylacetone (ACA) and vanadium triethoxide oxide (VTO) in a solvothermal reaction over a duration of seven days. They performed the reaction, with and without the presence of ACA and also LAHC, to see if it would have an effect on the reaction.<sup>56</sup> VO<sub>2</sub>(B) formed without ACA displayed rod-like properties, whereas when ACA was added the rods were more uniform in shape and finer. The difference in the results is thought to be due to the ACA promoting the condensation reaction, meaning that the crystal growth occurs before the surfactant molecules were absorbed.<sup>56</sup> To see if LAHC was essential for the formation of the nanorods, the ratio of VTO to LAHC was altered. Without LAHC there were no vanadium nanorods and when it was 50:50 nano-microplates were obtained. From this it was deduced that lowering the molar ratio results in a loss of microemulsion function and that, even though the process is not fully understood, LAHC plays a critical role in the formation of vanadium nanorods (the rods

cannot otherwise be obtained under hydrothermal conditions).<sup>56</sup>

A final method, by Zhou *et al.*,<sup>57</sup> used  $\text{VO}_2 \cdot x\text{H}_2\text{O}$ , distilled water and polyethyleneglycol (PEG-10000); these were placed in an autoclave for 24 hours. The addition of PEG-10000 was thought to be a decisive factor in the creation of the  $\text{VO}_2(\text{B})$  nanorods, so the experiment was rerun without it. No solid products were obtained, which showed that by using this synthesis method, PEG-10000 was needed. PEG-10000 is thought to facilitate the formation of  $\text{VO}_2(\text{B})$  due to its strongly basic properties and the possession of a lone pair of electrons on the oxygen atom. It is also thought to aid the synthesis of  $\text{VO}_2(\text{B})$  due to PEG-10000 being a non-ionic polymer with many hydrophobic and hydrophilic side groups as well as a high degree of flexibility. This flexibility and also the ability to be an oxygen donor enables it to couple with the  $\text{VO}^{2+}$  and form a thermodynamically favourable polymer complex and induces growth of  $\text{VO}_2(\text{B})$  nanorods in hydrothermal conditions.<sup>57</sup> When placed in a battery cell, the initial discharge capacity of the products reached 310 mAh/g, which is close to the theoretical capacity of  $\text{VO}_2(\text{B})$  and is much better than currently used cathodes of  $\text{LiCoO}_2$  and  $\text{LiMn}_2\text{O}_4$ .<sup>57</sup> The cell was cycled 30 times, and the cathode was shown to hold around 80% of the initial discharge capacity, which indicates that the  $\text{VO}_2(\text{B})$  nanorods synthesised by this method can be used for applications like lithium-ion batteries. The cycled product was placed in an XRD and found to remain as  $\text{VO}_2(\text{B})$ , meaning that there is good structural stability through charge/discharge cycles.<sup>57</sup>

It is well known that nanoscale materials have the potential to, and often do, exhibit physical and chemical properties that are very different to the properties that would be shown if they are in bulk. Research was carried out by Huynh *et al.*<sup>63</sup> found that not only does the properties of batteries rely upon their structure, but also upon the morphology of the components within the electrode. It is possible to tailor the shape of a particle as a result of careful consideration and alteration of the surfactant or solvent used, for example ethylene glycol solvent. It is possible to form  $\text{VO}_2$  nanobelts through hydrothermal synthesis and using formic acid as the reducing and acidifying agent. These nanowire,

nanorod and nanobelt materials adopt the metastable  $\text{VO}_2(\text{B})$  structure, which exhibits a metal–semiconductor transition, but not of the same magnitude as with  $\text{VO}_2(\text{R})$ .<sup>64</sup> Kam and Cheetham<sup>64</sup> have reported the solvothermal synthesis of vanadate structures, whose structure and morphology may be tailored by varying the reaction conditions. By altering the starting solvent as well as the starting vanadate, they have reported the formation of platelets ( $\text{VO}_2$ ), nanowires ( $\text{VO}_2$ ,  $\text{V}_3\text{O}_7 \cdot \text{H}_2\text{O}$ ) and rods ( $\text{V}_2\text{O}_5$ ).

Vanadium oxide has also been used to coat other cathodes. Lee *et al.* used a vanadium oxide sol–gel to coat  $\text{LiCoO}_2$  in an attempt to improve its cycle–ability at high charge cut off voltages.<sup>65</sup> It was found that by using a vanadium oxide coating the cycle–ability of  $\text{LiCoO}_2$  was indeed increased. After 50 cycles, the bare  $\text{LiCoO}_2$  had reduced in capacity by around 25%, whereas three different variations of vanadium oxide coated  $\text{LiCoO}_2$  were all above 90% capacity still. This was due to the vanadium oxide preventing the cation mixing during cycling and also by reducing the amount of active surface area that is in contact with the electrolyte.

### 1.3.4 Other components for Li–ion batteries

Along with cathodes, there are other vital components for a lithium–ion battery: anodes, electrolytes and separators. Optimisation of these components are carried out along side cathode research. Separators are used to separate the cathode and anode from each other; if the two electrodes were allowed to touch then the circuit would be shorted. The separator has to be porous, so as to allow the lithium ions to pass through it in the electrolyte.

Electrolytes are available in two forms, solid and liquid. Liquid electrolytes are easier to obtain and use, but carry the added risk of being hazardous and potentially explosive. A solid electrolyte functions in the same way except it is a solid electrolyte and separator. The lithium ions are still allowed to pass through the structure, but there is an increase to the safety of the battery.

Current research into anodes is vast. In this thesis, carbon is used as the anode, although research into titanates is promising.

### 1.3.5 Current challenges

There are many challenges for lithium-ion batteries. One of these, doping, has already been mentioned in 1.3.3.2. Doping can lead to increased performance by altering the structure of the electrode to enable more lithium ions access due to a greater interactivity between the electrode and the electrolyte. Coating is another method of increasing the performance of a battery. This is where a layer of another compound is placed around the outside of the cathode. Amine *et al.* discussed the different roles that surface coating plays on cathode materials for lithium-ion batteries.<sup>66</sup> They state that there are three types of coating: rough coating; core shell; and ultra-thin film coating. As expected, the rough coating does not offer enough protection and aid to the cathode, whereas a core shell offers too much and can impede the access and egress of the lithium ions and electrons to the cathode. Ultra thin film coating is the better option, as it gives a tune-able thickness and complete coating allowing the passage of lithium ions and electrons. It can be achieved by Atomic Layer Deposition (ALD), or by a laser, or by plasma-assisted chemical vapour deposition (CVD).

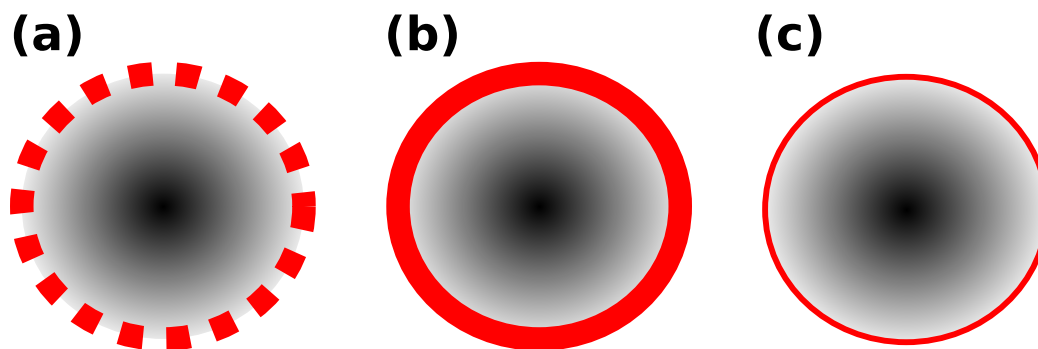


Figure 8: Image displaying the different varieties of coating. (a) shows rough coating, where it can be seen that there are areas where the particle is unprotected. (b) however shows core-shell coating. Here the coating is too thick and impedes the transport of electrons and lithium ions. (c) displays the best option of the three, where a thin, tuneable thickness provides protection for the cathode from the electrolyte and also allows the access and egress of lithium ions and electrons.

Coating with carbon has also been tested by Wei *et al.*<sup>67</sup> They coated carbon free  $\text{Li}_3\text{V}_2(\text{PO}_4)_3$  with a carbon coating of less than 100 nm thick. Under testing, this increased the electrical conductivity of the cathode by five orders of magnitude. The carbon coating also helped in preventing the formation of a solid electrolyte interphase film on the anode, decreased the resistance to charge transfer as well as increasing the diffusion coefficient of the lithium ions. All of the above factors put together helped to increase the overall electrochemical performance of the cathode.

A solid electrolyte interface is a layer that is formed instantaneously upon the electrode when contact between the metal and the electrolyte solution occurs.<sup>68,69</sup> This layer consists of reduction products made of electrolyte components, which are both insoluble and partially soluble. The layer acts as an interphase between the electrode and electrolyte and has the properties of a solid electrolyte with high electronic resistivity. The formation of this layer hinders access and egress of the lithium ions to and from the electrodes and electrolyte. Coating and doping are ways of overcoming problems such as poor performance, low conductivity or a solid electrolyte interface build up.

## 1.4 Aims and objectives

By the end of this research it is hoped that a better understanding about  $\text{VO}_2(\text{B})$  can be obtained with reference to its lithium-ion battery cathode properties and also to the effects of different means of synthesis. Different synthesis methods will be explored, including solvothermal and microwave synthesis methods. Through the use of a microwave oven synthesiser, reaction times can hopefully be reduced, with no detriment to the final product purity. Final reaction outcomes will be altered by variation of the starting materials, solvent and reaction conditions.

*In situ* x-ray absorption spectroscopy studies will also be conducted, in an effort to study the local structure changes occurring upon cycling the  $\text{VO}_2(\text{B})$  cathode.

Other cathode materials will also be studied using microwave-assisted solvothermal synthesis, these include lithium iron phosphate, lithium manganese phosphate and lithium cobalt phosphate, in an effort to provide new routes to these important materials.

All reaction products will be characterised fully, using x-ray diffraction, electron microscopy, XAS and charge-discharge cycling measurements.

## 2 Experimental

### 2.1 Characterisation techniques

Samples prepared were characterised using a number of techniques, including X-ray diffraction (XRD), X-ray absorption near edge structure (XANES), extended X-ray absorption fine structure (EXAFS) and scanning electron microscopy (SEM). These techniques are described below.

#### 2.1.1 X-ray Diffraction

X-ray based techniques include X-ray absorption, where the absorbed X-rays (see section 2.1.2) give local structure information, X-ray emission, where an electron beam causes the sample to emit X-rays which can be used for chemical analysis, and X-ray diffraction.

In 1895, a German physicist, Wilhelm Röntgen, discovered X-rays<sup>70</sup> and he was later awarded the Nobel Prize in Physics (1901) for this discovery.<sup>71</sup> Seventeen years later in 1912, Max von Laue postulated that X-rays might be diffracted when passed through a crystal, as he had realised that the wavelengths were comparable to the separation of lattice planes. He, along with Walter Friedrich and Paul Knipping, confirmed this theory and in 1914 Max von Laue won the Nobel Prize in Physics.<sup>72</sup>

X-rays are electromagnetic radiation with wavelengths in the order of  $10^{-10}$  m, or 1 Å and occur on the electromagnetic spectrum between  $\gamma$ -rays and ultraviolet radiation. X-rays are produced when high-energy electrons are accelerated into a metal. As the electrons decelerate due to travelling through the metal, they generate radiation of a continuous wavelength called Bremsstrahlung.<sup>73</sup> The electron will collide with electrons in the inner shell of the target atom, and both will then be expelled from the atom. An electron from a higher energy level will then drop down into the vacant space, and emit

excess energy as an X-ray photon<sup>74</sup> (see Figure 9).

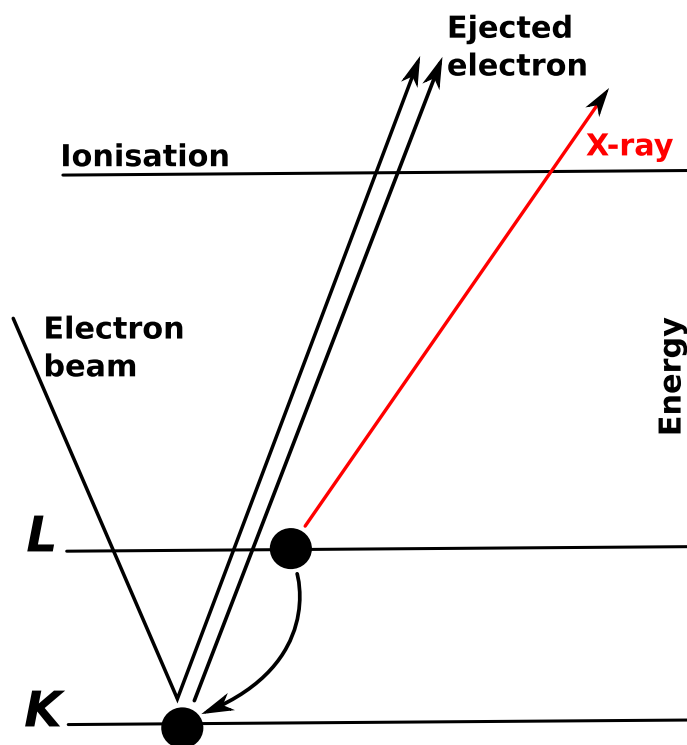


Figure 9: Generation of a Cu  $K\alpha$  X-ray. A 1s electron is ionised, a 2p electron falls into the vacancy in the 1s level and the excess energy is emitted as an X-ray photon.

Electrons emitted from the K-shell are classified as K-radiation, and similarly for L and M shells. The strong, distinct lines are labelled  $K_\alpha$ ,  $K_\beta$  and so on. Most experiments will require a monochromatic beam of X-rays instead of a continuum. The  $K\alpha$  line is the most intense for most metals, so the other wavelengths of X-ray are filtered out. A filter made from a thin metal foil from the adjacent element in the periodic table is required for this.<sup>29</sup>

Bragg developed a model in which diffraction is considered on reflection of X-ray beams for lattice planes.<sup>75</sup>

When the monochromatic X-ray beam of wavelength  $\lambda$  strikes the surface of a crystal, it may penetrate it and be reflected by one of many layers in the crystal (see Figure 10). If two parallel rays of the same wavelength reflect off two different, but adjacent, planes of the lattice, then the rays striking the lower layer must travel an additional distance (AB) before striking the plane below. When that ray is reflected it will also travel an extra distance (BC). The difference in the distances travelled between the two rays can be displayed as:

$$AB + BC = 2d\sin\theta \quad (3)$$

where  $\theta$  is the glancing angle. When the path-length distance is not an integer of the wavelengths, then they interfere destructively with each other. However if the path-length distance is an integer of the wavelengths ( $AB + BC = n\lambda$ ) then they interfere constructively. A reflection will be observed when the glancing angle satisfies Bragg's Law:<sup>75</sup>

$$n\lambda = 2d\sin\theta \quad (4)$$

where  $n$  refers to the reflection order and corresponds to the path-length differences, and  $d$  is the spacing between the planes in the atomic lattice.

Equation 4, along with Miller indices ( $hkl$ ), can be used to measure the cell dimensions ( $a, b, c$ ). For a simple cubic lattice, where  $a = b = c$  and using the three-dimensional form of Pythagoras' theorem, the perpendicular distances ( $d_{hkl}$ ) between planes are:

$$\frac{1}{d_{hkl}^2} = \frac{h^2}{a^2} + \frac{k^2}{b^2} + \frac{l^2}{c^2} \quad (5)$$

This only applies for systems with  $\alpha = \beta = \gamma = 90^\circ$ .

It is possible to substitute equation 4 into equation 5 to give the following:

$$\sin^2\theta_{hkl} = \frac{\lambda^2}{4a^2}(h^2 + k^2 + l^2) \quad (6)$$

The values for  $(h^2 + k^2 + l^2)$  are determined by various planes.

<i>hkl</i>	100	110	111	200	210	211	220	221	...
$(h^2 + k^2 + l^2)$	1	2	3	4	5	6	8	9	...

In order to calculate  $(h^2 + k^2 + l^2)$ , and therefore identify the *hkl* planes and crystal symmetry, the angle  $\theta_{hkl}$  needs to be known.  $\sin \theta_{hkl}$  can be calculated for a given value of  $(\lambda/a)$  (assuming a cubic unit cell). It should be noted that if two planes interfere with each other in a destructive way, then the diffraction line will be absent. An example are the (100) and (200) planes in a body centred lattice. As the (200) family will interleave and interfere with the (100) planes, there is no diffraction line, but as (100) does not interfere with the (200) planes, there will be a diffraction line at (200) (see Figure 11).<sup>75</sup>

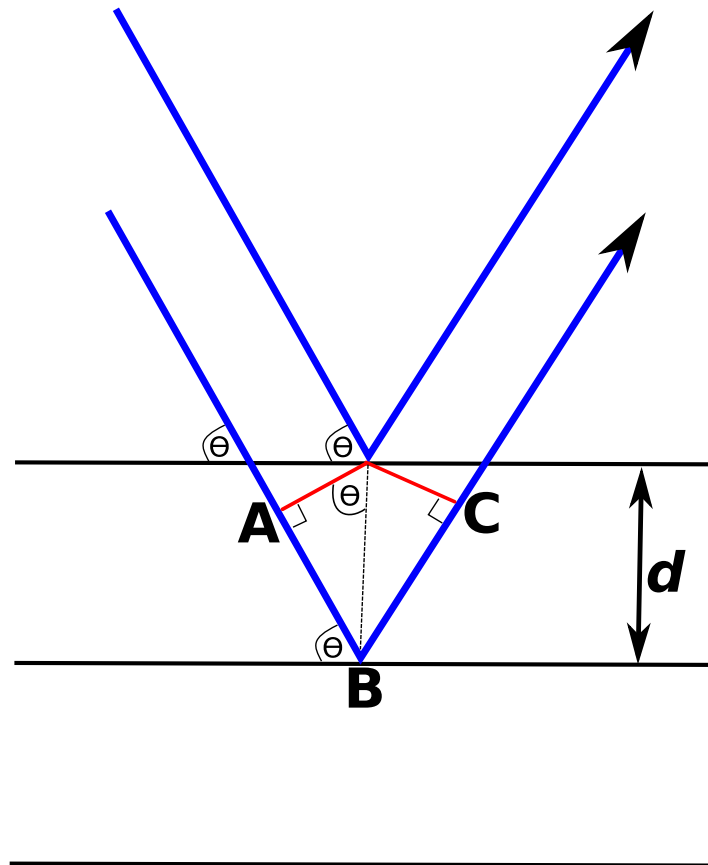


Figure 10: Visual representation of Bragg's law, showing the path-length difference  $AB + BC$ , which will depend upon the glancing angle,  $\theta$ . Constructive interference, or a reflection, will occur when  $AB + BC$  is equal to an integer number of the wavelength.

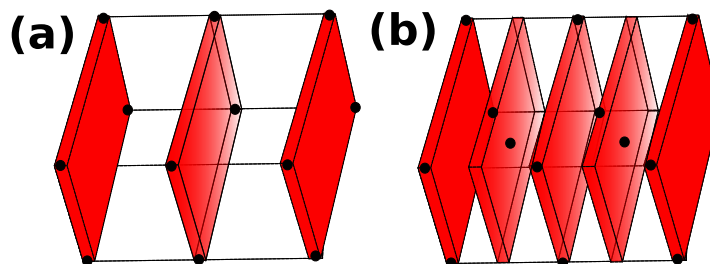


Figure 11: Miller indices for (a) simple cubic lattice and (b) body-centred cubic lattice displaying planes 100 and 200. The reflection from the 200 plane will interfere with that from the 100 plane, but not vice versa.

The X-ray pattern can be obtained and recorded using many methods, including powder and single crystal diffractions. A powder diffractometer will use a counter, which scans a range of  $2\theta$  values at a constant angular velocity. The angular range is usually 10 to  $80^\circ$ , with a scanning speed of  $2^\circ \text{ min}^{-1}$  ( $2\theta$ ). The aim is to use a sample which has a random arrangement of crystal orientations. If the crystal arrangement is not random then there is preferred orientation, which can induce errors in detected identities,  $I_{obs}$ .<sup>76</sup> Preferred orientation occurs when the crystals in a powder have a tendency to align in one direction. This can be due to the packing process into the X-ray diffraction sample holder or simply the axis that the crystals are formed along during synthesis.<sup>74</sup>

The X-ray source will strike the sample and reflected towards the detector (see Figure 12). Results are measured in intensities of X-rays received in a function of  $2\theta$ . Every compound has a different diffraction pattern, so this technique enables the identification of samples. From this it is possible to deduce aspects of the crystal structure.<sup>77</sup>

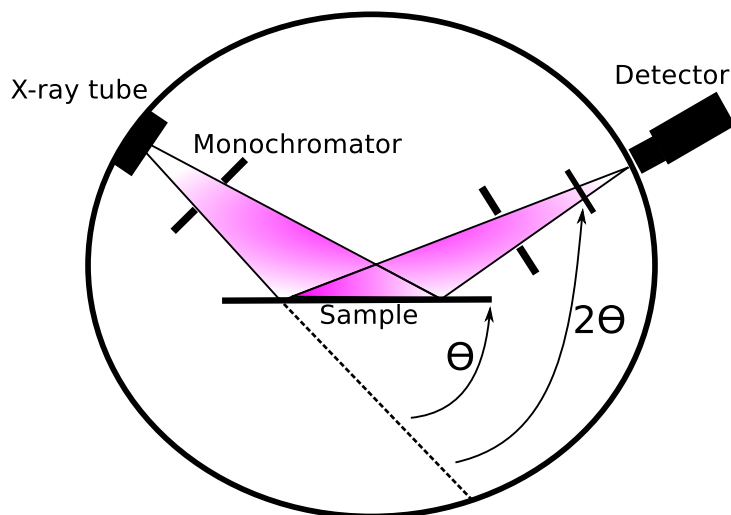


Figure 12: Arrangement of a sample, source and detector on the circumference of a circle. The X-rays will leave the source, be monochromated in a collimator, strike the sample and be reflected. The detector (and maybe also the source) will gradually move, increasing in  $2\theta$ , detecting the intensity of X-rays at each angle.

A Rietveld Refinement can be carried out on the data that is gained from an X-ray diffractometer. The process involves utilising a computer programme that assists the user to 'fit' their data to the modelled pattern calculated for the powder being examined. The technique removes the background noise from the data as well as making sure there is no shift in the data due to data collection errors in the instrument. It also allows easier identification of peaks that are in the data but not the model, as they stand out prominently in the difference curve. The use of Rietveld Refinement is a way to show lines in positions consistent with a proposed model.

### 2.1.2 Synchrotron Radiation

Synchrotron radiation is the electromagnetic radiation emitted by electrons moving at velocities through an external magnetic field along a curved trajectory with a large radius of curvature, for example in a synchrotron.<sup>78</sup> Any accelerated charged particle produces some electromagnetic radiation.

As the particles increase in energy, the strength of the magnetic field used to direct them must be altered with each turn to keep the particles moving in the same ring. The change in magnetic field must be carefully synchronised to the change in energy or the beam will be lost. To reach high energies, physicists sometimes use a sequence of different size synchrotrons, each one feeding the next, bigger one. Particles are often pre-accelerated before entering the first ring, using a small linear accelerator or other device.<sup>79</sup>

A synchrotron radiation source is a facility which employs a dedicated storage ring or synchrotron. Electrons are accelerated and then injected into the storage ring, where they are then kept at a constant energy. The electrons travel in a circular path with a circumference of up to several hundred metres, within the orbit of the accelerator through the use of a constant magnetic field.<sup>76</sup> Synchrotron radiation is tangentially emitted from the beam orbit into a very small angle called the photon opening angle.<sup>80</sup>

Storage rings and synchrotrons are very similar. They both consist of a roughly circular ring of magnets under a vacuum. Synchrotrons, however, are designed to rapidly accelerate groups of electrons from a low injection energy to around 10–100 times higher. This makes the electron energy, and therefore electron radiation, non-constant and will vary from where in the acceleration cycle the electrons are from one cycle to the next.<sup>81</sup>

Figure 13 is a schematic of a synchrotron. The circular ring is the synchrotron or particle accelerator, where the electrons are accelerated. The synchrotron emits synchrotron radiation, especially X-rays. These are sent into the various beam-lines around the synchrotron which are shown as the straight lines branching out of the synchrotron.

Each beam–line contains scientific instruments, experiments etc. and receives an intense beam of radiation.

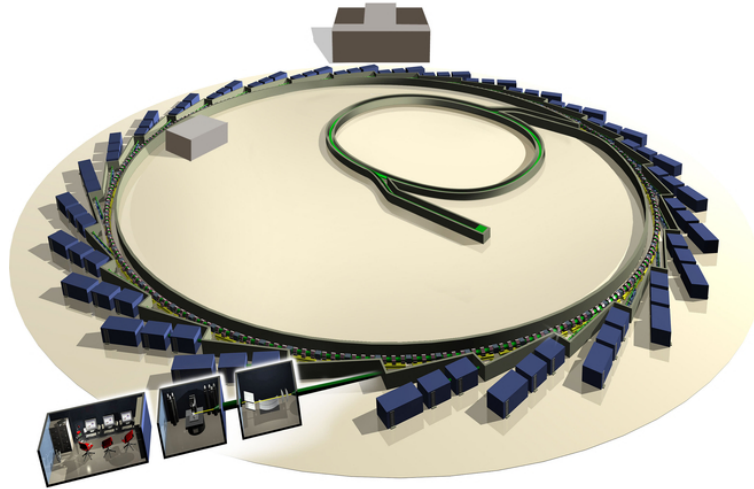


Figure 13: General diagram of Diamond Light Source Synchrotron based in Oxfordshire, England<sup>2</sup>

Synchrotron radiation was first observed, albeit accidentally, in 1947 at the General Electric 70–MeV Synchrotron in America.<sup>82</sup> The theory surrounding the radiation of charges in a circular motion originated in 1898 with the work of Liénard.<sup>83</sup> Much theorised work was carried out subsequent to this discovery<sup>84–88</sup> and in 1945, Blewett<sup>89</sup> observed the effects of the radiation on the electron orbit within electron accelerators.

There was a renewed interest in synchrotron radiation due to its observation in 1947, alongside the construction of electron accelerators in the post–war period. In the late 1940s research by Sokolov<sup>90</sup> and Schwinger<sup>91</sup> enabled the theory to be fully developed so that accurate predictions could be made with regards to intensity, spectral and angular distributions, polarisation etc.

Experimental investigations were performed by Pollack *et al.*<sup>92</sup> and since then have been

developed at numerous synchrotrons and storage rings throughout the world.<sup>93–96</sup> In 1974, the SPEAR storage ring at Stanford was converted into a synchrotron facility and was the first to have multiple experimental stations. This was important as it allowed more people access to the multi-GeV photons provided by the storage ring. Important early results led to the development of extended X-ray absorption fine structure (EXAFS) (further discussed in 2.1.2.2) as a broadly applicable structural tool.<sup>81</sup>

It was first thought that this radiation was just an annoyance resulting from a leakage of energy. However, it was later noted that there were some useful properties produced by synchrotron radiation including white light, high intensity, naturally collimated, polarized and periodic time structure, as well as high stability over long periods. The radiation was also many magnitudes more intense than that of a beam from a X-ray tube source. X-ray spectroscopy was almost exclusively carried out using these X-ray tubes prior to use of synchrotron radiation. Some laboratories do still use X-ray tubes, but the use of synchrotron radiation is preferred, as it is suited to high resolution work required for the study of small samples. This is because of the high intensity, collimation, polarisation properties and the high stability of the synchrotrons as a photometric source.<sup>81</sup> However, the radiation within the synchrotron is a very broad band and needs to be dispersed to a select and tune to a specific, monochromatic band.

Literature on monochromators is vast, but essentially monochromators use gratings as dispersive elements within the UV region and with photon energies of between 1000–1500 eV.<sup>97</sup> To achieve the X-ray band of the radiation, a holographically made transmission grating is used as the monochromator.<sup>98</sup> These intense photon beams, which are highly collimated, are very useful for applications within the photon and X-ray absorption spectra.<sup>81</sup>

Each beam-line station at a synchrotron is optimised for a particular experiment. For the work in this thesis, local structure studies were carried out using the B-18 beam-line at the Diamond Light Source, which is specialised for EXAFS and XANES data collection.

EXAFS and XANES are X-ray absorption techniques, they measure the absorption of X-rays by the samples, particularly at energies within the absorption edge regions. As the X-rays are absorbed, the absorbing atom promotes one of the core electrons to a higher unoccupied state, or into a free unbound state (photoelectric effect). They are utilised to investigate local structure but cannot usually be used in a normal laboratory as high energy X-rays are required.<sup>74</sup>(see Figure 14)

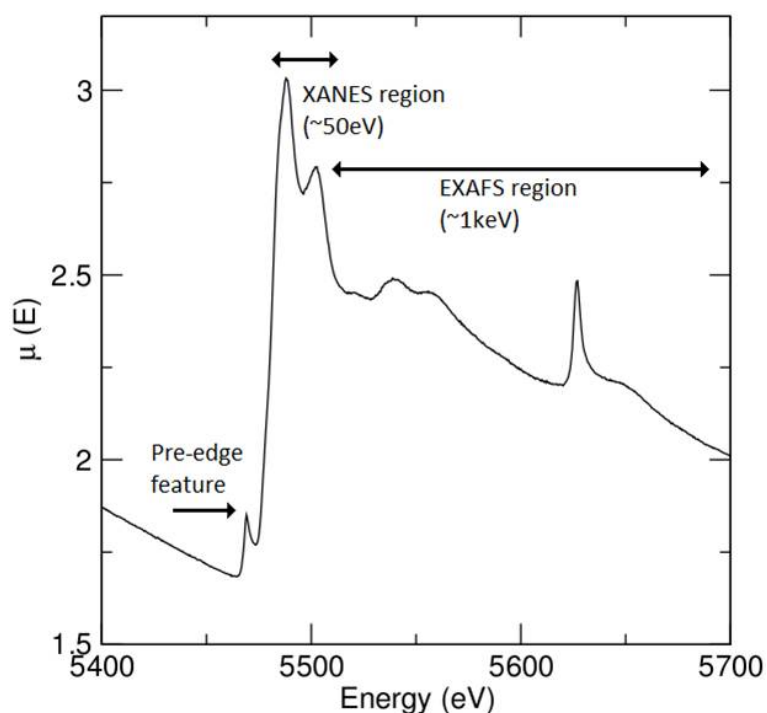


Figure 14: Example spectra showing the EXAFS and XANES absorption spectrum of vanadium dioxide. This shows the pre-edge, the XANES region, and the EXAFS region.

**2.1.2.1 XANES** XANES, or X-ray Absorption Near Edge Structure, is a technique used to look at fine structure associated with inner shell transitions within the absorption edge region. Atoms can give very characteristic X-ray absorption and emission spectra. This is due to the various ionisation and inter-shell transitions occurring (see Figure 15).

For the 1s electron in copper metal to be ionised almost 9 keV (or 1.380 Å) is required. To ionise an L shell electron, 2s or 2p, around 1 keV is needed, significantly less than for a 1s electron.

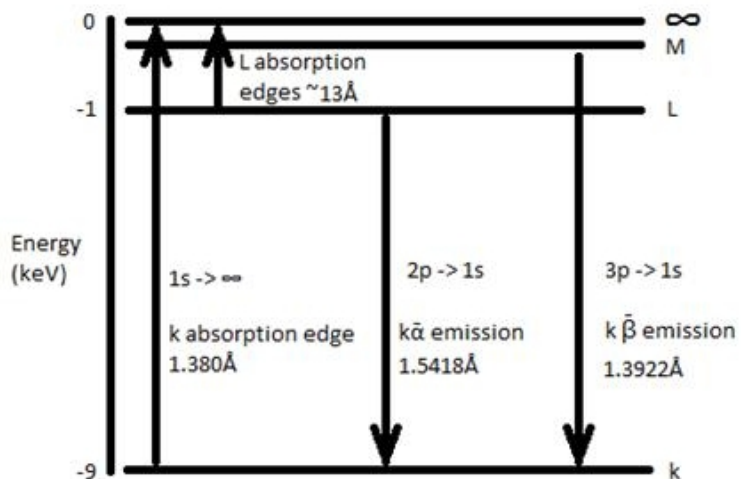


Figure 15: Schematic of electronic transitions responsible for emission and absorption X-ray spectra. Values included are those of copper.

The labelling of the absorption edge depends upon the core electron that it being excited. A K-absorption edge refers to the promotion of a 1s electron to a higher shell. The pre-edge feature in this case would be representative of the 1s promotion to a  $nd$  orbital, a forbidden transition. The rest of the XANES region is a measurement of the 1s orbital electrons being promoted in a  $(n+1)p$  orbital transition.<sup>74</sup>

For an L-absorption edge, this is an excitation of a 2s or 2p electron to a higher shell. This time however, there are 3 absorption edges (2s, 2p 1/2 and 2p 3/2). These will all have different minimum energies and so will occur at different points along the absorption curve (see Figure 16).

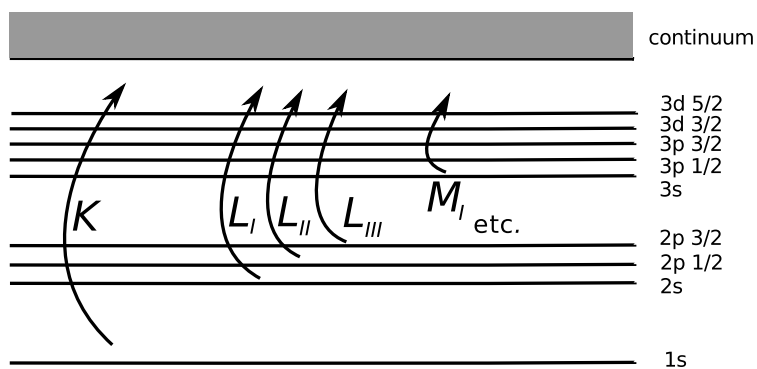


Figure 16: Figure showing the electronic transitions responsible for emission and absorption X-ray spectra.

The exact peak positions on the spectrum depend upon the oxidation state, surrounding ligands, site symmetry and the type of bonding present. It is therefore possible to use the absorption spectra to investigate the local, fine structure of the sample due to the high resolution available.<sup>74</sup>

**2.1.2.2 EXAFS** EXAFS, or Extended X-ray Absorption Fine Structure, is a structural technique that originated in the 1970s and is now used by many fields within physics, chemistry and biology. This technique can potentially provide information pertaining to the local environments of specific atoms within a material, such as bond distances to neighbours, coordination number and elements in the coordination shell around the atom.<sup>78</sup>

The oscillations in the EXAFS region of the absorption spectra can be explained by thinking of the electron being ejected as a quantum particle with wave properties. With this thought in mind, the photo-electron will move out of the excited atom as a spherical wave. When this wave interacts with a neighbouring atom, it will be reflected back upon itself. This backscattered wave can then undergo interference with the original outgoing wave. The waves can constructively or destructively interact with each other, depending

upon the distance between the two atoms and the wavelength of the photo-electron. Due to changes in the X-ray energy, and also the photo-electron wavelength, the interference will go through constructive-destructive cycles (see Figure 17).<sup>74</sup>

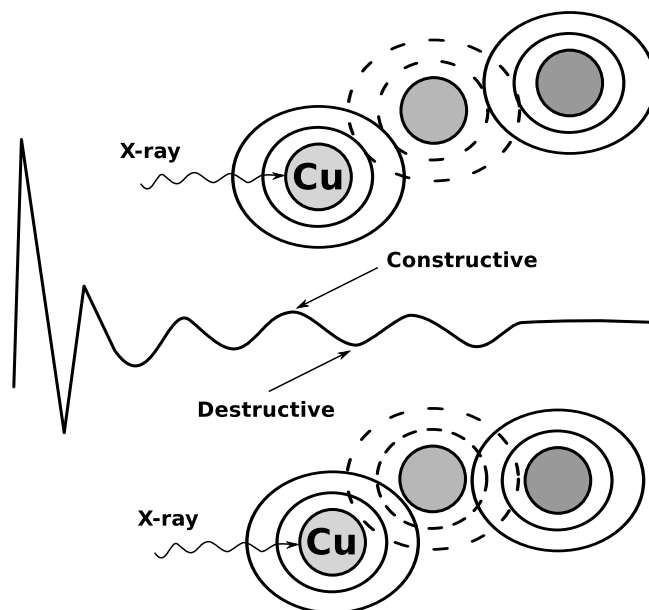


Figure 17: Schematic showing the interference from the outgoing electron and the backscattered electron. Constructive and destructive peaks and troughs occur in the absorption spectra due to these interactions.

This is a qualitative explanation of the EXAFS pattern, and so the wave must be a sine wave, meaning the time between the oscillations depends upon the distance between the photoelectron-emitting atom and the backscattering atom. Therefore EXAFS contains information on the bond length or the radii of the coordination shells. Also the amplitude of the oscillations will show how much backscattering is occurring, which will indicate how many neighbouring atoms there are around the original photo-electron emitting atom, giving a coordination number for it. Finally, a fraction of the outgoing wave

that will be backscattered is dependent upon the type of atom. An atom with a low atomic number will be a weaker scatterer than an atom with a high atomic number, or larger number of electrons. Therefore the amplitude of the backscattered oscillations will depend on the type of atoms surrounding the original atom; the interpretation of the spectrum gets more difficult with different atom types in the coordination shell of the atom being examined.<sup>80</sup>

Before analysing the spectrum, the data need to first be normalised. In the normalisation process, any data that are outside that which would be expected from a free atom are extracted.

The next step is to take the normalised EXAFS data and to Fourier transform them. This will give information on how many shells are contributing to the inner bonding and also rough estimates of bond distance between the atoms.

EXAFS is equally suitable for non-crystalline and crystalline materials. In the case of gels, glass and amorphous metals where other methods have difficulty gaining structural information, EXAFS can be utilised with success. The main advantage of EXAFS is that the absorption edge can be tuned to a specific element, and tested in turn to determine the local structure and the elements present. Conventional diffraction methods, in contrast, give only a single averaged coordination environment of all elements involved.<sup>74</sup>

### **2.1.3 Microscopy**

The human eye has a resolving power of around 0.1 mm. If we wish to observe objects smaller than this then we need a microscope. There are two major classes of microscope, optical and electron. Electron microscopes can then be subdivided again into scanning electron and transmission electron microscopes.

Since the samples in this thesis are up to several microns long, they are not observable by optical microscopy. Similarly they are too large for transmission electron microscopy.

Scanning electron microscopy is the preferred microscoping tool. Here each technique is described, with particular attention on scanning electron microscopy.

**2.1.3.1 Optical Microscope** An optical microscope, or light microscope, functions by using visible light and a system of lenses to magnify small samples. Light microscopes have a few advantages. Firstly they are relatively inexpensive, especially when compared to an electron microscope. They are also easy to use, again when compared with an electron microscope, and gaining an image of the sample is much simpler. They can also produce colour images. The major problem is, however, that they have a very limited magnification. Most optical microscopes can only magnify to around 1000x, with none being able to magnify over 2000x. This means that objects that are smaller than biological cells, for example viruses, atoms and molecules, cannot be seen.<sup>99</sup>

**2.1.3.2 Transmission Electron Microscope** Transmission electron microscopy is mainly used for looking at the inner structure of a specimen at high magnification. Transmission electron microscopes are composed of two or more condenser lenses, an electron gun, a specimen holder and a viewing screen. They work by shooting a beam of electrons from an electron gun, which is condensed multiple times. The condensers are basically magnets which are used to focus the beam. The beam then travels through the sample; only a few electrons pass through the specimen and are then recorded by the detector screen below the specimen. The image is recorded in two dimensions and only in grey-scale.

Transmission electron microscopes are capable of reaching magnifications of up to 50kx, and have a much higher resolving power when compared to optical and scanning electron microscopes. The sample has to be loaded into a specialised grid which sits midway in the instrument's column. Results are displayed on a fluorescent screen. Darker areas of the image indicate that less electrons were transmitted through the sample and that those areas are thicker. This makes transmission electron microscopes ideal for examination

of viruses, cells and tissues due to their ability to penetrate objects, as long as they are “electron transparent”. It can be a time consuming process to make the sample thin enough to examine, and risks damaging it.

**2.1.3.3 Scanning Electron Microscope** In 1935, the first scanning electron microscope image was obtained by Max Knoll, when he imaged silicon steel to show the electron channelling contrast.<sup>100</sup> Physical principles for the microscope and also the interactions of the beam and the sample were demonstrated by Manfred von Ardenne in 1937, and although he never made a working instrument, he produced a British patent.<sup>101,102</sup> Professor Sir Charles Oatley marketed the first working scanning electron microscope in 1965, the “Stereoscan”.<sup>103,104</sup>

Scanning electron microscopes are primarily used for observing the fine structure of a specimen surface at a high magnification. A scanning electron microscope works by scanning the surface of the sample using a finely converged electron beam, whilst inside a vacuum, and detects the signals emanating from the sample, and presents an enlarged image of the sample surface on a monitor screen.

Whilst irradiating the sample surface, a number of signals are produced, namely secondary electrons, backscattered electrons and characteristic X-rays. The microscope generally uses secondary electrons or backscattered electrons in the formation of the image (see Figure 18).

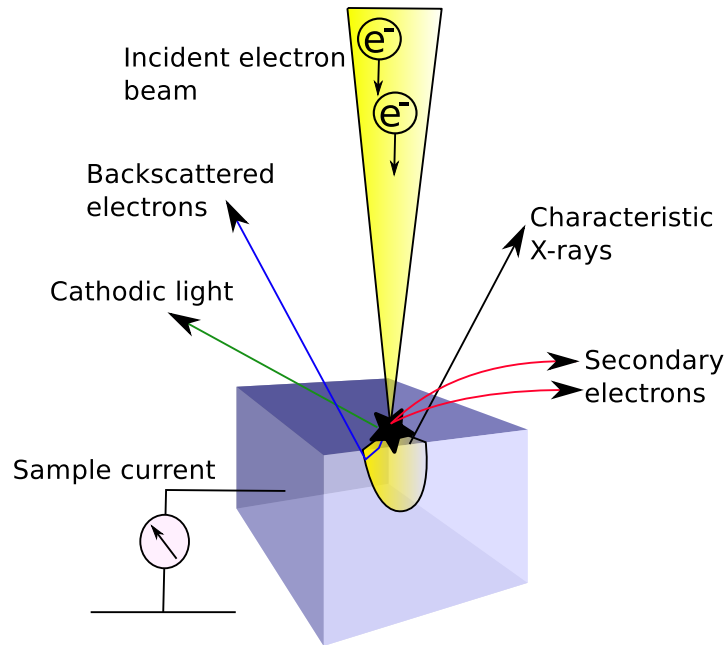


Figure 18: Figure shows the different signals produced from the sample being struck by the electron beam from the scanning electron microscope. Those used most commonly by scanning electron microscopes are secondary and backscattered electrons.

Secondary electrons, located near the sample surface, are released once the atoms absorb the electron fired at it. These give a sense of the fine topographical surface structure of the sample. Backscattered electrons are reflected away from the sample by the surface atoms. Different samples will reflect different amounts because of their composition. Due to this, a backscattered electron image will display the compositional distribution at the sample surface. These electrons can also be used for elemental analysis through the attachment of an X-ray analyser.

A scanning electron microscope is made up of many components (see Figure 19). The microscope consists of a column, specimen chamber, display and operating section. The interior of the column is kept under low pressure at all times. The electrons leaving the electron gun are converged through the use of electromagnetic condenser and objective lenses into a fine beam. Deflection coils then direct the beam across the sample. Inside

the specimen chamber, there is a detector for the secondary electrons, backscattered electrons and also an X-ray detector for the X-rays.

A scanning electron microscope is able to give the surface structure of a sample and can do so by giving very clear images. There is also a large depth of field which allows more of the specimen to be in focus at once. There is also a greater degree of magnification due to the use of electromagnets rather than lenses. The only real disadvantages of scanning electron microscopy are that there is no colour in the image, and that to get the best images available, the sample needs to be electrically conductive, which can be achieved with use of a sputterer to coat the sample in a thin gold film.

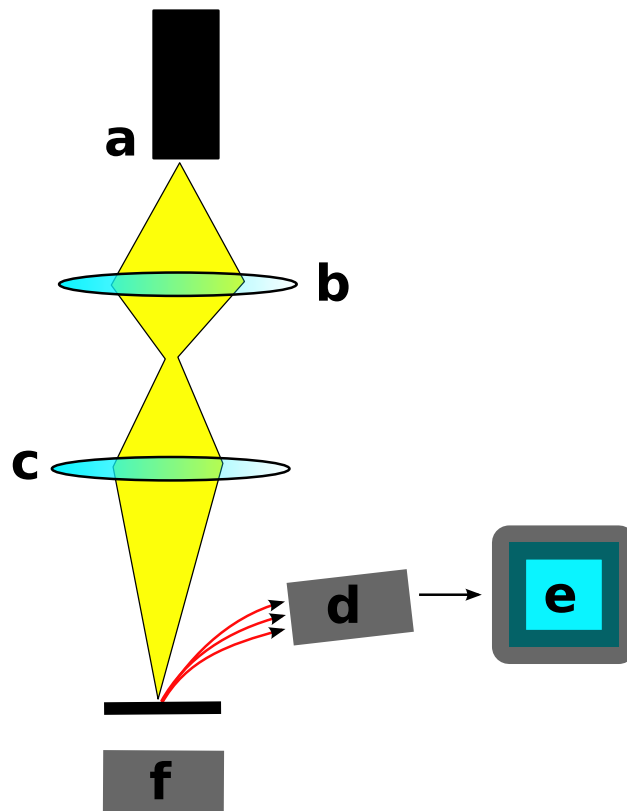


Figure 19: The path electrons take in a typical scanning electron microscope set-up to enable the magnification of small objects. The electron gun (a) emits and accelerates the electrons, the condenser lenses (b) then converge this beam to make it finer. The deflection coils then aim the beam at the sample whilst the objective lens (c) focus the beam. The electron beam then leaves the column and enters the sample chamber. The secondary electron detector (d) then detects the electrons emitted, amplifies them and converts them into an electrical signal and transfers this to a computer monitor (e) where the image can be seen. The vacuum pump (f) keeps the column under low pressure at all times.

### 2.1.4 Use of a Potentiostat

The potentiostat is used for electroanalytical experiments and allows the control of a three electrode cell for battery performance measurements. The system functions by maintaining the potential of the working electrode at a constant level. By adjusting the current at the auxiliary electrode, the potential can be maintained in respect to the reference electrode. Figure 20 is a schematic displaying the layout of both a 2 electrode and 3 electrode Swagelok<sup>TM</sup> cell.

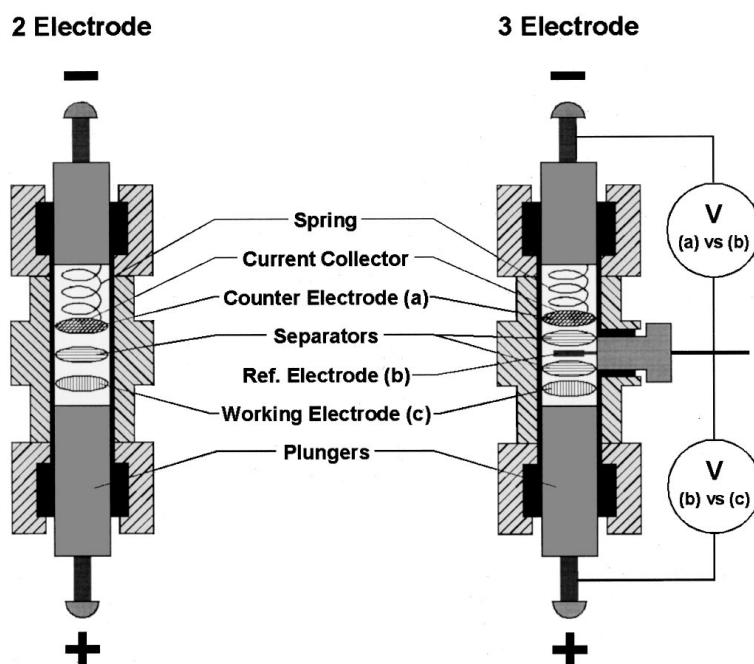


Figure 20: Schematic of a two and three-electrode Teflon Swagelok<sup>TM</sup> cell. The major difference between the two is the addition of a third electrode (b). This acts as a reference for the voltage at the other two electrodes as can be seen in the image. By maintaining the potential at the working electrode (c), that at the counter or auxiliary electrode (a) can then be adjusted with respect to the reference electrode (b). Image from Amatucci *et al.*<sup>3</sup>

The potentiostat is fundamental to modern electrochemical studies, especially for investigating reaction mechanisms related to redox chemistry. The data generated would be plotted depending upon the type of analysis. For example, in voltammetry, the electrical current (amps) is plotted against the electric potential (voltage). In a bulk electrolysis though, the total electrical charge (Coulombs) is plotted against time (seconds).

Most early potentiostats could function independently, outputting physical data. Modern potentiostats are designed to interface with a computer and operate through bespoke software. The software allows the user to quickly change between both experiments and experimental conditions. Data stored on a computer can also be more easily and accurately analysed than using earlier methods.

## 2.2 Starting Materials

Vanadium(V) oxide, ammonium metavanadate, formaldehyde, manganese(II) acetate tetrahydrate, cobalt(II) nitrate hexahydrate, iron(II) oxalate dihydrate, lithium dihydrogenphosphate and ethylene glycol were obtained from Sigma Aldrich. Acetone and ethanol were obtained from Fisher Scientific and were both of analytical reagent grade.

## 2.3 Experimental Procedures

Syntheses were carried out using both the traditional solvothermal synthesis method using a PTFE lined acid digestion Parr bomb cell and also using a CEM Discover – SP with active microwave for microwave synthesis (180–240  $V_{ac}$ , 50/60 Hz,  $P_{max}$  1100 W, Mag freq 2455 Hz and  $P_{max}$  microwave 300 W).

Products were characterised through X-ray diffraction and scanning electron microscopy, with selected samples being characterised through EXAFS and XANES as well as having electrical property measurements taken.

X-ray diffraction patterns were obtained using a Philips PW1730 X-ray diffractometer with Cu K $\alpha$  radiation (1.5418 Å) at a 30 kV accelerating voltage and 20 mA current.

Scanning electron microscopy images were obtained using a Hitachi 3400S Scanning electron microscope with a nominal resolution of 5 nm per pixel with a maximum magnification of 300k (maximum usable magnification of around 100k). The maximum single image resolution is 2048 x 1800. Samples were mounted on a carbon disc, maximum sample size being 10 x 10 x 2 cm and with a minimum X, Y, Z stepsize of 1 nm. The maximum beam voltage is 30 kV with a variable stepsize of 0.1 kV. It is fitted with Secondary, Backscatter (5 segment) and Oxford Instruments Xmax EDX detectors. There is also a variable backscatter mode, enabling the acquisition of backscatter images at a chamber pressure of up to 100 Pa.

EXAFS and XANES spectra were obtained from the B18 beam-line at the Diamond Synchrotron facility in Oxfordshire, England.

Charge-discharge measurements were obtained using a Bio-logic SAS VMP3 potentiostat (110–240 V<sub>ac</sub>, 50/60 Hz and P<sub>max</sub> 600 W).

### 2.3.1 Solvothermal synthesis of VO<sub>2</sub>(B) nanorods

#### 2.3.1.1 48 hour synthesis of VO<sub>2</sub>(B) nanorods using V<sub>2</sub>O<sub>5</sub> starting material

Vanadium(V) oxide (1.81 g; 0.01 mol) was dispersed in formaldehyde (37% aqueous solution, 30 mL) by stirring for 15 minutes. The resulting yellow suspension was then placed within a PTFE lined Parr bomb and solvothermally treated for 48 hours at 180°C. After cooling to room temperature, the resulting blue-black suspension was washed with water, ethanol and acetone before being allowed to dry overnight at 60°C in an oven.

#### 2.3.1.2 24 hour synthesis of VO<sub>2</sub>(B) nanorods using V<sub>2</sub>O<sub>5</sub> starting material

The same synthesis procedure was carried out as in 2.3.1.1 except the time of solvothermal treatment was altered to be 24 hours.

### 2.3.1.3 12 hour synthesis of VO<sub>2</sub>(B) nanorods using V<sub>2</sub>O<sub>5</sub> starting material

The same synthesis procedure was carried out as in 2.3.1.1 except the time of solvothermal treatment was altered to be 12 hours.

### 2.3.1.4 48 hour synthesis of VO<sub>2</sub>(B) nanorods using NH<sub>4</sub>VO<sub>3</sub> starting material

Ammonium metavanadate (0.31 g; 99%) was dispersed in formaldehyde (37% aqueous solution, 30 mL) by stirring for 15 minutes. The resulting pale yellow suspension was then placed within a PTFE lined Parr bomb and solvothermally treated for 48 hours at 180°C. After cooling to room temperature, the resulting blue–black suspension was washed with water, ethanol and acetone before being allowed to dry overnight at 60°C in an oven.

## 2.3.2 Microwave synthesis of VO<sub>2</sub>(B)

**2.3.2.1 Time variation study** Vanadium(V) oxide (0.30 g; 0.01 mol) was dispersed in formaldehyde (37% aqueous solution, 15 mL) by stirring for 15 minutes. The resulting yellow suspension was then placed within a microwave oven test tube and solvothermally treated in a microwave oven at 180°C for 1, 3 and 6 hours. After cooling to room temperature, the resulting suspensions (green–brown for 1 and 3 hours, blue–black for 6 hours) were washed with water, ethanol and acetone before being allowed to dry overnight at 60°C in an oven.

**2.3.2.2 Temperature variation study** Vanadium(V) oxide (0.30 g; 0.01 mol) was dispersed in formaldehyde (37% aqueous solution, 15 mL) by stirring for 15 minutes. The resulting yellow suspension was then placed within a microwave oven test tube and solvothermally treated in a microwave oven for 1 hour at 150, 180 and 200°C. After cooling to room temperature, the resulting green–brown suspensions were washed with water, ethanol and acetone before being allowed to dry overnight at 60°C in an oven.

**2.3.2.3 Synthesis of VO<sub>2</sub>(B) nanorods using V<sub>2</sub>O<sub>5</sub> and C<sub>2</sub>H<sub>6</sub>O<sub>2</sub> starting materials** Vanadium(V) oxide (0.30 g; 0.01 mol) was dispersed in ethylene glycol (99.8%, 15 mL) by stirring for 15 minutes. The resulting yellow suspension was then placed within a microwave oven test tube and solvothermally treated in a microwave oven synthesiser at 250°C over 60 minutes and 90 minutes. After cooling to room temperature, the resulting green–brown suspensions were washed with water, ethanol and acetone before being allowed to dry overnight at 60°C in an oven.

**2.3.2.4 Synthesis of VO<sub>2</sub>(B) nanorods using NH<sub>4</sub>VO<sub>3</sub> and CH<sub>2</sub>O starting materials** Ammonium metavanadate (0.15 g; 99%) was dispersed in formaldehyde (37% aqueous solution, 15 mL) by stirring for 15 minutes. The resulting pale yellow suspension was then placed within a microwave oven test tube and solvothermally treated in a microwave oven at 180°C for 6 hours. After cooling to room temperature, the resulting green–brown suspension was washed with water, ethanol and acetone before being allowed to dry overnight at 60°C in an oven.

### 2.3.3 Swagelok<sup>TM</sup> battery preparation

Olivine sample was mixed with 20% by weight carbon (Ketchen black) without any binder added. This was mixed and ground thoroughly using a ball mill for 15 minutes. The electrochemical cell consisted of 6 mg of mixed powder sample as the cathode material which was separated from a lithium foil (counter electrode) by a sheet of porous fibre-glass soaked in battery electrolyte LP30 (1 M lithium hexafluorophosphate in ethylene carbonate:dimethyl carbonate 1:1 w/w). Cycling experiments were conducted at 25°C using a Biologic potentiostat system at constant discharge rate of 1 Li/20 hour (C/20) (n decreases by 1). This was carried out by my supervisor and collaborators over in Amiens, France.

### 2.3.4 Bellcore film preparation for EXAFS experiments

VO<sub>2</sub>(B) (0.2264 g) was ground with carbon (0.0461 g) using a pestle and mortar. To make the film, Kynar polymer (0.0661 g) and dibutyl phthalate (0.0987 g) were dissolved in a few drops of acetone. The VO<sub>2</sub>(B)/C mixture was added to 1 mL acetone and allowed to stir for 30 minutes. The sample was spread over a glass plate to form a thin film and was allowed to dry. A disk of material was cut out and washed with diethyl ether (3 x 10 mL) to extract the dibutyl phthalate. The disks were dried in an oven at 70°C for 5 mins. The mass of active sample in each disk was calculated from the surface area and mass loss. For the disk cycled in situ, the density of active material was calculated to be 3.76 mg cm<sup>-2</sup>. The electrochemical cell consisted of a disk of sample as the cathode material which was separated from a lithium foil (counter electrode) by a sheet of fibreglass soaked in battery electrolyte LP30 (1 M lithium hexafluorophosphate in ethylene carbonate:dimethyl carbonate 1:1 w/w). Cycling experiments were conducted at 25°C using a Biologic potentiostat system at constant discharge rate of 1 Li/20 hour (C/20) (n in Li<sub>n</sub>VO<sub>2</sub> decreases by 1). This was carried out by my supervisor and collaborators over in Amiens, France.

### 2.3.5 Preparation of samples for EXAFS measurements

Boron nitride (0.140 g; 0.02 mol) was mixed with a varying amount of sample (see Table 1). The mixture was then pressed into a pellet of 20 mm in diameter under 10 tonnes of pressure in a pellet press. The pellets were then placed in a pellet holder within the beam line and X-rays were passed through them to gain EXAFS and XANES data on them.

Table 1: Amounts of sample added to boron nitride for EXAFS experiment pellets

Sample	Mass / g
Vanadium(V) Oxide	0.0040
Lithium Iron Phosphate	0.0105
Lithium Cobalt Phosphate	0.0100
Lithium Manganese Phosphate	0.0091

### 2.3.6 Microwave synthesis of olivine phosphates

**2.3.6.1 Preparation of  $\text{LiFePO}_4$**  Iron(II) oxalate dihydrate (0.36 g; 0.02 mol) and lithium dihydrogenphosphate (0.21 g; 99%) were dispersed in ethylene glycol (99.8%, 5 mL) by stirring for 15 minutes. The resulting suspension was then placed in a microwave oven test tube and solvothermally treated in a microwave oven synthesiser at 300°C for 2 hours. After cooling to room temperature, the resulting pale brown suspension was washed with water, ethanol and acetone before being allowed to dry overnight at 60°C in an oven.

**2.3.6.2 Preparation of  $\text{LiCoPO}_4$**  Cobalt(II) nitrate hexahydrate (0.36 g; 0.019 mol) and lithium dihydrogenphosphate (0.21 g; 99%) were dispersed in ethylene glycol (99.8%, 5 mL) by stirring for 15 minutes. The resulting suspension was then placed in a microwave oven test tube and solvothermally treated in a microwave oven synthesiser at 300°C for 2 hours. After cooling to room temperature, the resulting blue suspension was washed with water, ethanol and acetone before being allowed to dry overnight at 60°C in an oven.

**2.3.6.3 Preparation of  $\text{LiMnPO}_4$**  Manganese(II) acetate tetrahydrate (0.36 g; 0.016 mol) and lithium dihydrogenphosphate (0.21 g; 99%) were dispersed in ethylene glycol (99.8%, 5 mL) by stirring for 15 minutes. The resulting suspension was then placed in a microwave oven test tube and solvothermally treated in a microwave oven

synthesiser at 300°C for 2 hours. After cooling to room temperature, the resulting pale cream suspension was washed with water, ethanol and acetone before being allowed to dry overnight at 60°C in an oven.

## 3 New routes to vanadium oxides

### 3.1 Introduction

Vanadates, particularly bronze phase  $\text{VO}_2$ , have been touted as potential cathodes for lithium-ion batteries, due to their structure and their ability to access multiple oxidation states.<sup>55</sup> Bronze phase  $\text{VO}_2$  ( $\text{VO}_2(\text{B})$ ) has an affinity for lithium intercalation, making it a suitable lithium-ion battery cathode material.<sup>47,56,57</sup>

As well as the structure and multiple oxidation states of vanadates making them ideal cathode candidates, they are also low in toxicity and cost, yet highly available. Further research is, however, needed because the vanadate is prone to structural collapse following repeated charge and discharge cycles.<sup>60</sup>

Recent literature has pointed towards nanoscale  $\text{VO}_2(\text{B})$  as being suitable for use as a cathode. As functional properties of lithium-ion battery cathodes are influenced by many factors, a 1-D particle nanostructure is advantageous over bulk materials as there is an improvement in charge transport.<sup>8,47</sup> Other benefits to the use of nanostructures within a lithium ion rechargeable battery include the increased surface area made available by having nanomaterials. With the increased surface area, there is greater electrode-electrolyte interaction. One report of increased performance of nanoscale materials over bulk concerns  $\text{LiFePO}_4$ , which is a poor electronic conductor.<sup>48</sup> When nanosized,  $\text{LiFePO}_4$  has a shorter diffusion path length for lithium ion transport. This simple change enhances the power density and rate capability. Nanostructured materials also have an improved life cycle due to improved support of the strain from lithium intercalation.<sup>48</sup>

The nanoscale nature of a material is dependent upon the reactants and reaction process. There are many methods available to synthesise  $\text{VO}_2(\text{B})$ . One reported synthesis of the bronze phase of  $\text{VO}_2$  involves the solvothermal reduction of  $\text{V}_2\text{O}_5$  by formaldehyde.<sup>105</sup> A similar method has also been reported by Kam *et al.*,<sup>64</sup> using  $\text{NH}_4\text{VO}_3$  mixed with formic acid. For the work described here, similar solvothermal methods were employed,

particularly the use of  $V_2O_5$  and formaldehyde with a PTFE lined Parr bomb cell.

At the moment, there is a lack of literature looking at microwave oven synthesis of  $VO_2(B)$ , which this thesis addresses. There is no literature report on how  $VO_2(B)$  particle morphology and shape affects the cycling ability.

## **3.2 Preparation and characterisation of $VO_2(B)$ nanorods**

### **3.2.1 Solvothermal Synthesis of $VO_2(B)$ nanorods**

$V_2O_5$  was mixed with a 37% aqueous solution of formaldehyde and reacted in a Parr bomb at  $180^\circ\text{C}$  for 48 hours. The resulting blueish-black precipitate was washed, dried and characterised via X-ray diffraction and scanning electron microscopy. In addition to that, extended X-ray absorption fine structure (EXAFS) and X-ray absorption near edge structure (XANES) data were also recorded, as described in Chapter 4.

The method was altered to include different reaction times, starting vanadates, other reagents and solvents. The aim of this was to find out whether the alteration of these variables could be used to control the formation and morphology of  $VO_2(B)$ .

$V_2O_5$  and  $NH_4VO_3$  were used as the starting vanadates and the solvents were aqueous formaldehyde, ethylene glycol and oxalic acid. Reactions were all carried out over both 24 and 48 hour periods, as well as a select few over 12 hours.

### **3.2.2 Characterisation of $VO_2(B)$ nanorods made via solvothermal synthesis**

**3.2.2.1 X-ray diffraction** The X-ray diffraction patterns in Figure 21 show the formation of  $VO_2(B)$  prepared using solvothermal reduction of  $V_2O_5$  which was reduced by formaldehyde in a Parr bomb a range of times at  $180^\circ\text{C}$ .

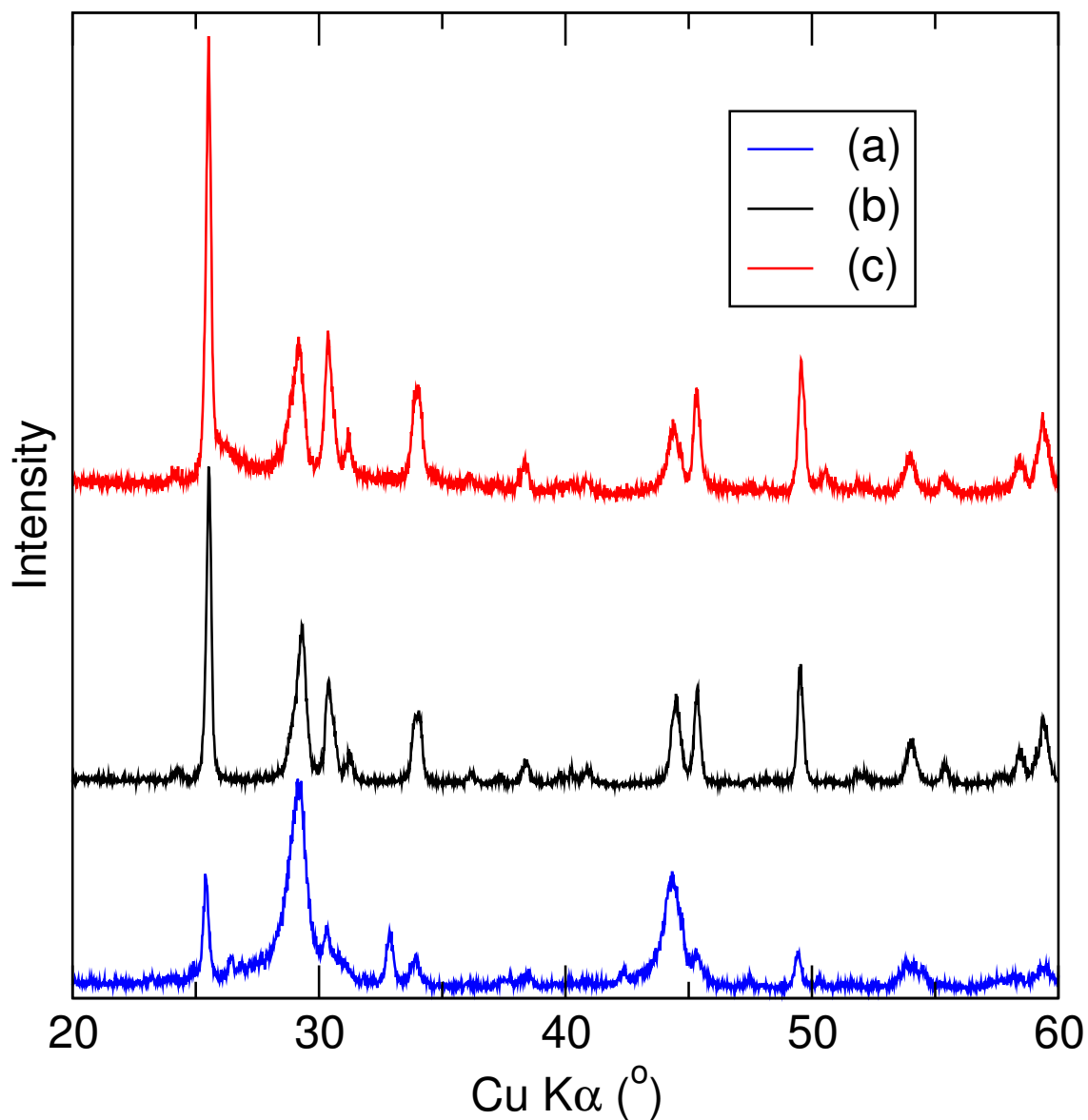


Figure 21: X-ray diffraction patterns for samples prepared through solvothermal synthesis. Samples were ground and mounted in an aluminium sample holder. Samples were prepared at 180°C for (a) 12 hours (b) 24 hours and (c) 48 hours. It can be seen that for the sample synthesised over 12 hours is very different from the other two data sets, indicating that 12 hours is not long enough at 180°C to produce VO<sub>2</sub>(B). The other two data sets show very little change indicating that VO<sub>2</sub>(B) can be synthesised after just 24 hours, rather than 48 hours.

The temperature and quantities of reactants were kept constant and the time the reaction was carried out over was varied. The selected times were 12, 24 and 48 hours. The 48 hour experiment was similar to a previously published method.<sup>105</sup> Data set (c) in Figure 21 is for the run carried out over 48 hours. The pattern obtained corresponds to that of previous literature,<sup>105-108</sup> and was selected for Rietveld refinement of the X-ray diffraction profile. The 24 hour run (b) shows very little difference, if any, from that of the data collected for the 48 hour product. This shows that the method does not necessarily need to run for over 48 hours to achieve VO<sub>2</sub>(B).

The data from the 12 hour experiment (a) is, however, not the same as samples (b) and (c); this is evident in the peak at 33° 2θ, which is absent from the other samples. This peak may be attributed to the V<sub>3</sub>O<sub>7</sub> phase. Also at 2θ=54°, there is a single, wide peak rather than the two peaks seen for VO<sub>2</sub>(B). This has been compared to diffraction by V<sub>6</sub>O<sub>13</sub>. At this point, V<sub>6</sub>O<sub>13</sub> has multiple peaks merged into one. Due to the resolution of the instrument used, it is possible that these multiple peaks cannot be resolved. These observations indicate that the sample contains multiple intermediate phases, and that the reaction has not yet gone to completion. The other peaks, although not as intense, do match that of VO<sub>2</sub>(B). The reaction therefore takes between 12 and 24 hours to reach completion.

Table 2: Lattice parameters from the Rietveld refinement performed on VO<sub>2</sub>(B) synthesised over a 48 hour period using V<sub>2</sub>O<sub>5</sub> and formaldehyde as the reactants; the model uses data from Oka *et al.*<sup>1</sup>

Lattice Parameters	Oka <i>et al.</i> <sup>1</sup>	48 Hour
a/Å	12.093	12.050
b/Å	3.7021	3.6900
c/Å	6.4330	6.4273
$\beta/^\circ$	106.97	106.94
R <sub>w</sub>	0.1060	0.1646

Figure 22 shows a plot of the data collected for the 48 hour experiment after Rietveld refinement using data from Oka *et al.*<sup>1</sup> as the structural model.

Table 2 displays the lattice parameters from the Rietveld refined of data collected and compared to the model structure; the values are seen to be very similar which shows a good fit of the data, (the R<sub>w</sub> value is slightly high).

The black circles in figure 22 represent the original data collected, whereas the overlying red line shows the model used to fit it against, in this case using data from Oka *et al.*<sup>1</sup> The blue curve underneath shows the difference between the data and the model. The difference plot was fairly flat, but there are some peaks remaining. These peaks can be attributed to intensity differences in the data, as the peaks do overlay, and their positions not different from one another. One possible reason for this difference is preferred orientation within the crystals when they were packed into the X-ray diffraction plate. Unfortunately there was not enough time to recheck this.

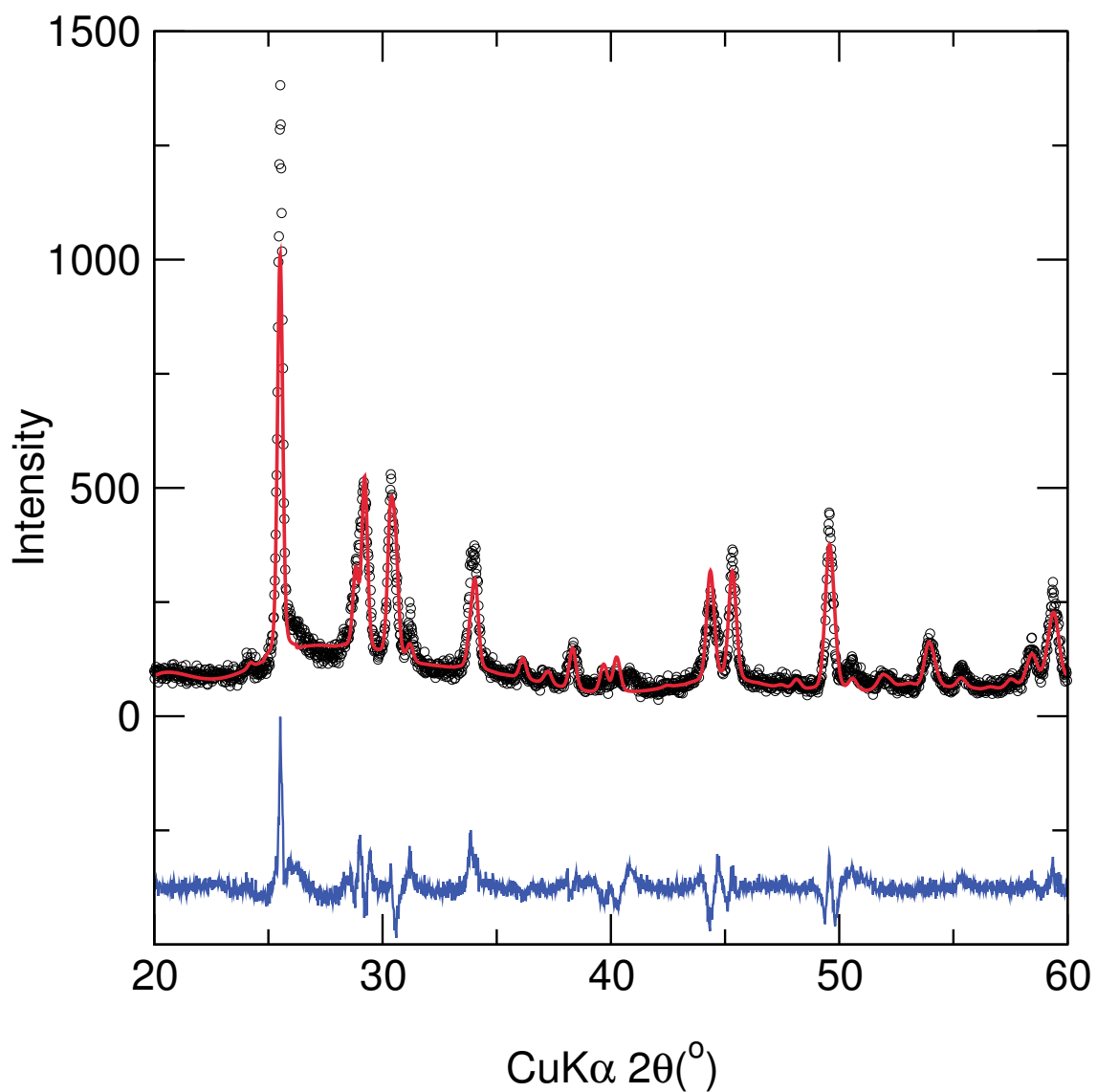


Figure 22: X-ray diffraction pattern of VO<sub>2</sub> prepared through solvothermal synthesis of V<sub>2</sub>O<sub>5</sub> which is reduced by formaldehyde in a Parr bomb for 48 hours at 180°C. Samples were ground and mounted in an aluminium sample holder. Rietveld refinement was performed on the data collected, using a structural model of Oka *et al.*<sup>1</sup> The black circles represent the data, the red curve represents the model the data were fitted to and the blue curve represents the difference between the data and the model.

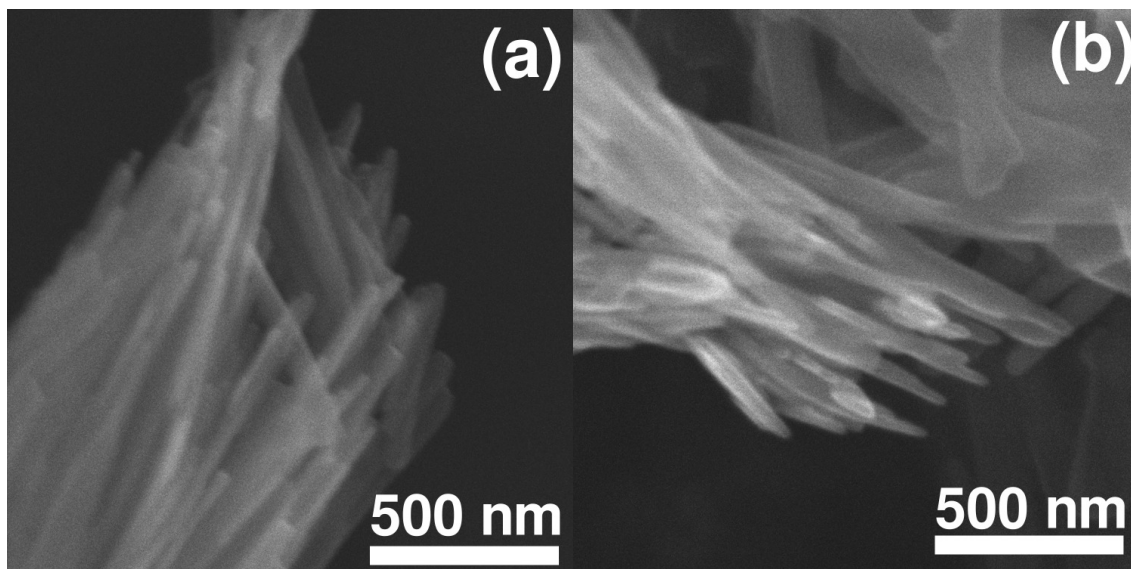


Figure 23: Scanning electron microscopy images of samples prepared via solvothermal synthesis at varying reaction times. Samples were synthesised at  $180^{\circ}\text{C}$  for (a) 24 and (b) 48 hours. There is a noticeable thickening of the rods with increasing time.

**3.2.2.2 Scanning Electron Microscopy** Figure 23 shows the scanning electron microscopy images taken of the samples prepared via solvothermal synthesis at  $180^{\circ}\text{C}$ . The first image (a) is for the sample synthesised over 24 hours and image (b) is that synthesised over 48 hours. It can be seen from these images that as the temperature is raised the product particle increases in thickness, changing from 75 nm for 24 hours to 100 nm for 48 hours; the length, however, remains around a micron ( $1\mu\text{m}$ ) in both cases.

### 3.3 Microwave synthesis of $\text{VO}_2(\text{B})$

Microwave synthesis routes were investigated in order to establish new, shorter duration reaction pathways to  $\text{VO}_2(\text{B})$  nanostructures. To begin with, the same reactants as used in solvothermal synthesis were employed ( $\text{V}_2\text{O}_5$  and formaldehyde), to allow the optimum reaction times and temperatures to be established. As a starting point, the

reaction temperature was held at 180°C and the reaction times were increased from 1 to 3 to 6 hours. Finally, a series of reactions where the temperature was varied and the time maintained at 1 hour were also carried out (150, 180 and 200°C).

### **3.3.1 Characterisation of VO<sub>2</sub>(B) made via microwave synthesis at varying reaction times**

**3.3.1.1 X-ray diffraction** Figure 24 is an X-ray diffraction pattern for VO<sub>2</sub>(B) samples that were prepared using microwave synthesis. For this synthesis, the temperature was kept constant, with aqueous formaldehyde used as the solvent. The reaction was carried out over three different time scales, (a) 1 (b) 3 and (c) 6 hours. As can be seen from the graphs, there is an obvious evolution of the products over time. There are some common features in all of them, with the peaks at around  $2\theta=38$  and  $45^\circ$  being the most noticeable. However, these peaks may be assigned to Al<sub>2</sub>O<sub>3</sub>. This could be easily explained, as the sample holder used in obtaining the X-ray diffraction pattern is made of aluminium, which will have an Al<sub>2</sub>O<sub>3</sub> surface film.

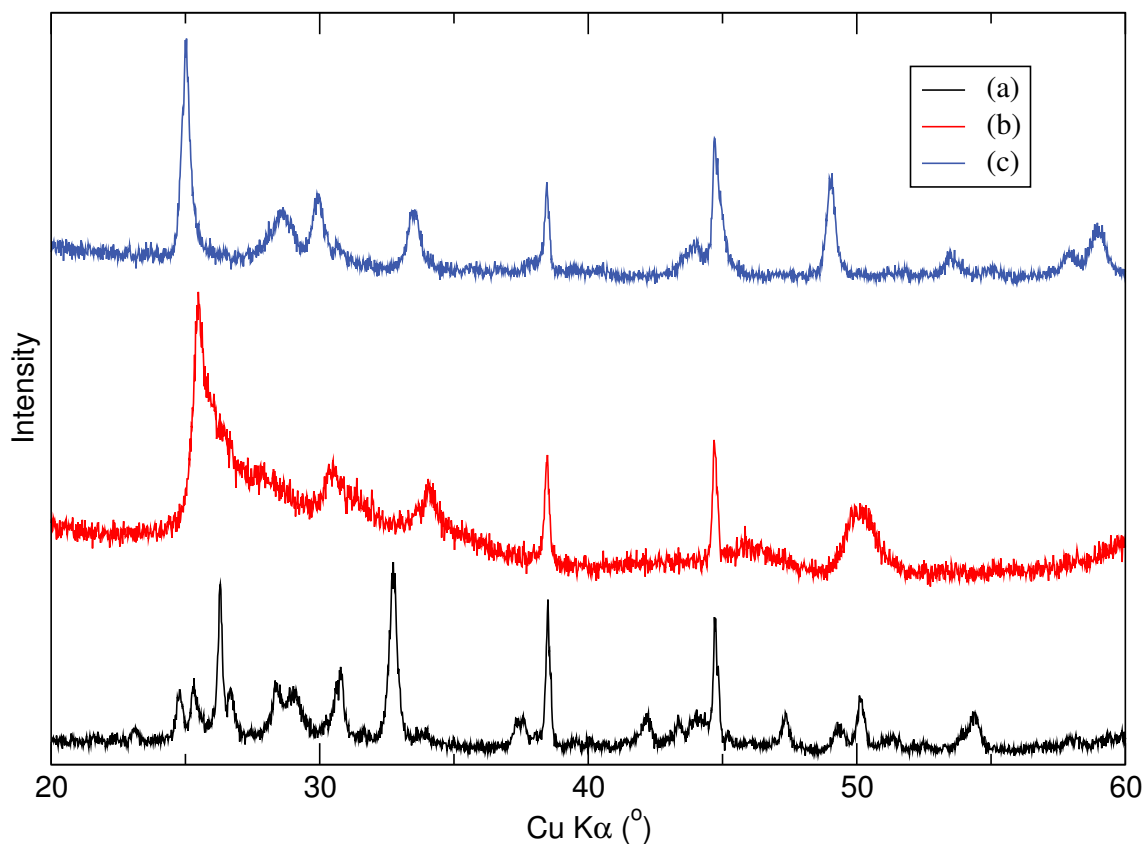


Figure 24: X-ray diffraction pattern of VO<sub>2</sub>(B) prepared via microwave synthesis using V<sub>2</sub>O<sub>5</sub> and formaldehyde at 180°C for (a) 1 hour (b) 3 hours and (c) 6 hours. Samples were ground and mounted in an aluminium sample holder. There is a noticeable change in the X-ray diffraction patterns as the time of the reaction is increased. The widening of the peaks within (b) could be due to it having a more nanosized phase than (a) and (c).

The bottom line, (a), has many peaks in it which indicates that the reaction has not gone to completion after 1 hour and that there are still starting materials mixed in with the product; several peaks may be attributed to either V<sub>2</sub>O<sub>5</sub> or V<sub>3</sub>O<sub>7</sub>.

The red line, (b), has fewer peaks for other phases, which indicates that the reaction is closer to completion after 3 hours. However, on comparison with the X-ray diffraction of the completed product from solvothermal synthesis (see Figure 25), it is clear that

the reaction has not finished (there are extra peaks). There is broadening of the peaks in the pattern, which is consistent with very thin nanoscale walls. There is also a clear asymmetrical sawtooth profile, suggesting that there is turbostratic disorder between the layers. Turbostratic disorder is a term given to disorder between differing layers, where there is different rotations with respect to an axis.<sup>109</sup> When compared, it was found that  $V_6O_{13}$  has two peaks in this same region, with the peak at the greater angle having a lower intensity (almost to an extent that it can resemble a shoulder on the main peak). It is possible that this is visible in the plot, although the sawtooth profile of the pattern makes it difficult to ascertain. This lack of clarity could possibly occur due to a poor resolving power, making the individual peaks difficult to see, or the particles being very small in size and therefore causing line broadening.<sup>110</sup> Observation under a scanning electron microscope would prove if the particles are indeed smaller in size.

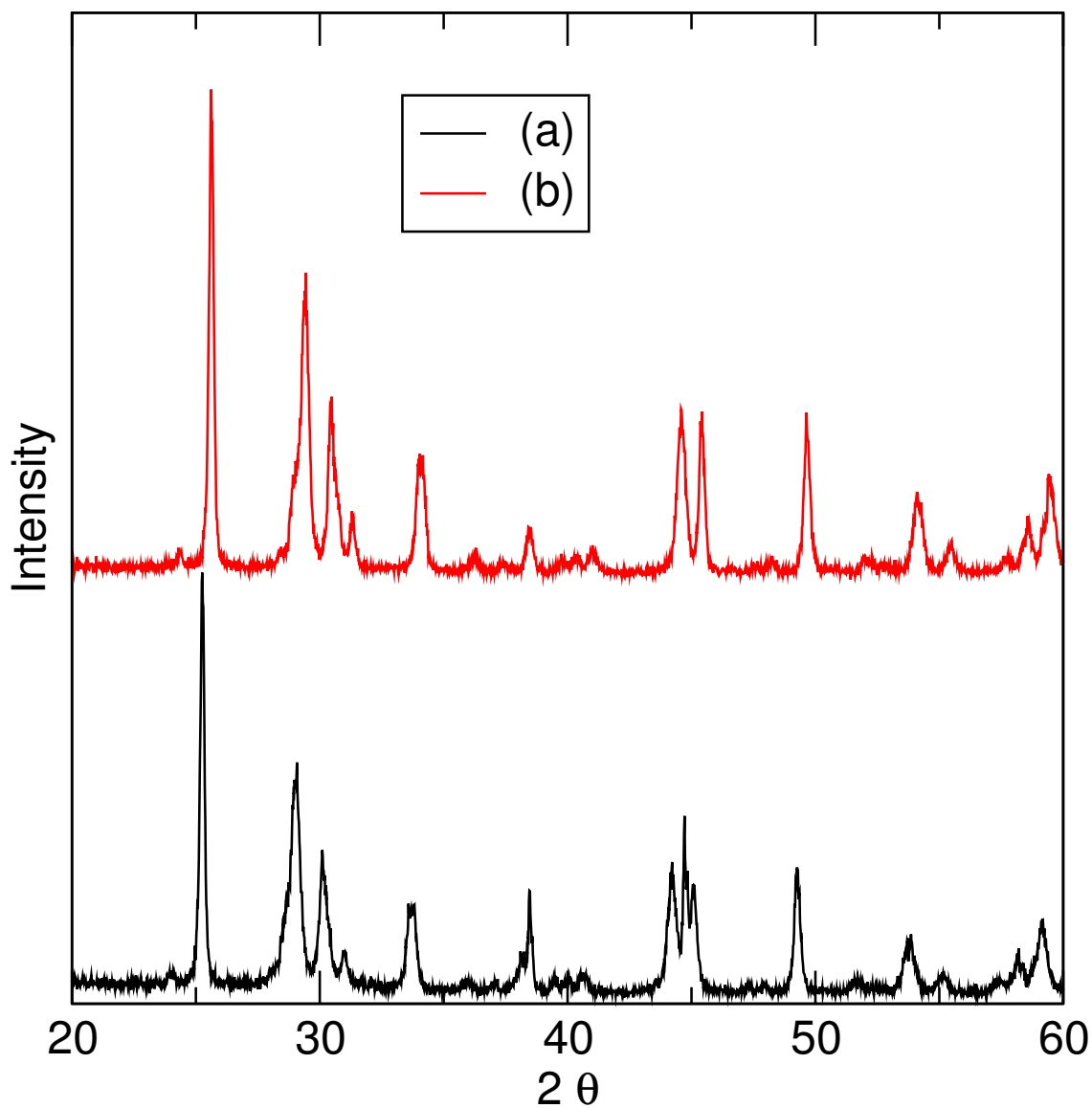


Figure 25: X-ray diffraction pattern of  $\text{VO}_2(\text{B})$  prepared via microwave and solvothermal synthesis using  $\text{V}_2\text{O}_5$  and aqueous formaldehyde at  $180^\circ\text{C}$ . Samples were ground and mounted in an aluminium sample holder. (a) is the 6 hour microwave synthesis run and (b) is the 48 hour solvothermal synthesis experiment. Both patterns appear very similar in appearance indicating that the 6 hour microwave synthesis run has produced  $\text{VO}_2(\text{B})$ .

The final pattern, (c) in figure 24, was for a product synthesised over 6 hours. This is the most promising as the profile is similar to that for samples prepared solvothermally over

48 hours (Figure 25). The peaks were found to be assignable to  $\text{VO}_2(\text{B})$ , indicating that this synthesis method had been successful, and that no contamination was discernible. The next steps are to look at the sample under a scanning electron microscope to examine any morphology differences.

Given that the 6 hour synthesis run gave a product almost identical to the solvothermal synthesis products, the data were then run through a Rietveld refinement (see Figure 26), using data from the model of Oka *et al.*<sup>1</sup> The black circles represents the original data used and the red line is the model profile. The blue curve is the difference plot, which displays a good correlation between data and model peak positions. Peaks in the difference plot are possibly due to preferred orientation of the crystals. The data show broad peaks, possibly due to particles being nanoscale in size.

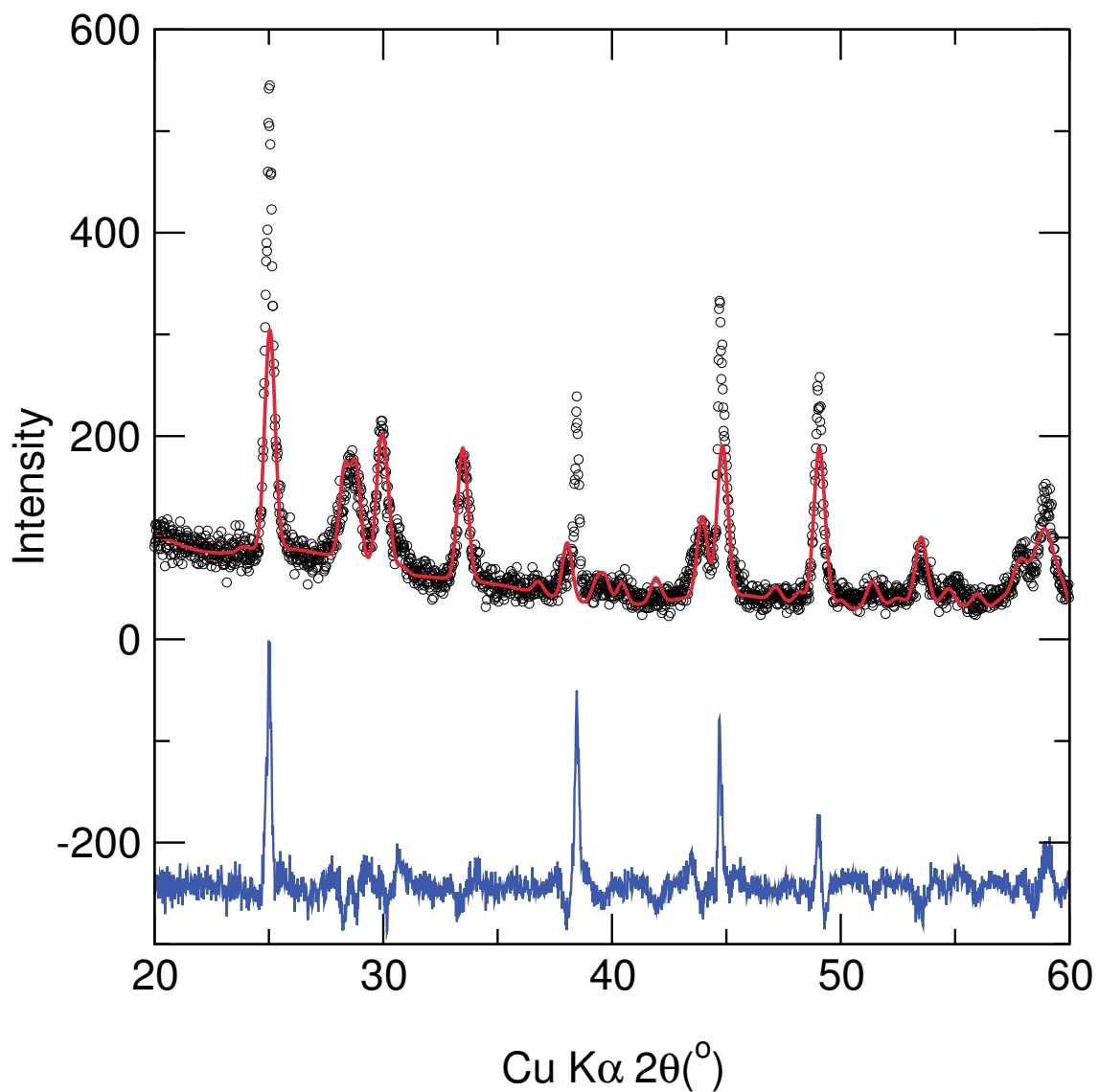


Figure 26: X-ray diffraction pattern of VO<sub>2</sub>(B) prepared via microwave synthesis using V<sub>2</sub>O<sub>5</sub> and aqueous formaldehyde at 180°C for 6 hours. Samples were ground and mounted in an aluminium sample holder. The data have been fitted using a Rietveld refinement, using the data from Oka *et al.*<sup>1</sup> as the model. The black circles represent the data, the red curve represents the model the data were fitted to and the blue curve represents the difference between the data and the model.

Table 3: Lattice parameters from the Rietveld refinement performed on the VO<sub>2</sub>(B) synthesised over a 48 hour period in the Parr bomb cell and also by the 6 hour microwave oven run using V<sub>2</sub>O<sub>5</sub> and formaldehyde as the reactants. The model uses data from Oka *et al.*<sup>1</sup>

Lattice Parameters	Oka et al. <sup>1</sup>	48 Hour	6 Hour
a/Å	12.093	12.050	12.053
b/Å	3.7021	3.6900	3.6990
c/Å	6.4330	6.4273	6.4408
$\beta/^\circ$	106.97	106.94	107.34
R <sub>w</sub>	0.1060	0.1646	0.2097

Table 3 shows a comparison of the lattice parameters from both the data and the model after the Rietveld refinement, as well as the data from the 48 hour bomb run discussed earlier. All the values are very similar upon comparison showing that there is a good fit of the data. The only major difference is a doubling of the R<sub>w</sub> value for the microwave oven experiment. This increase in the goodness of fit parameter may be due to a reduction in particle size.

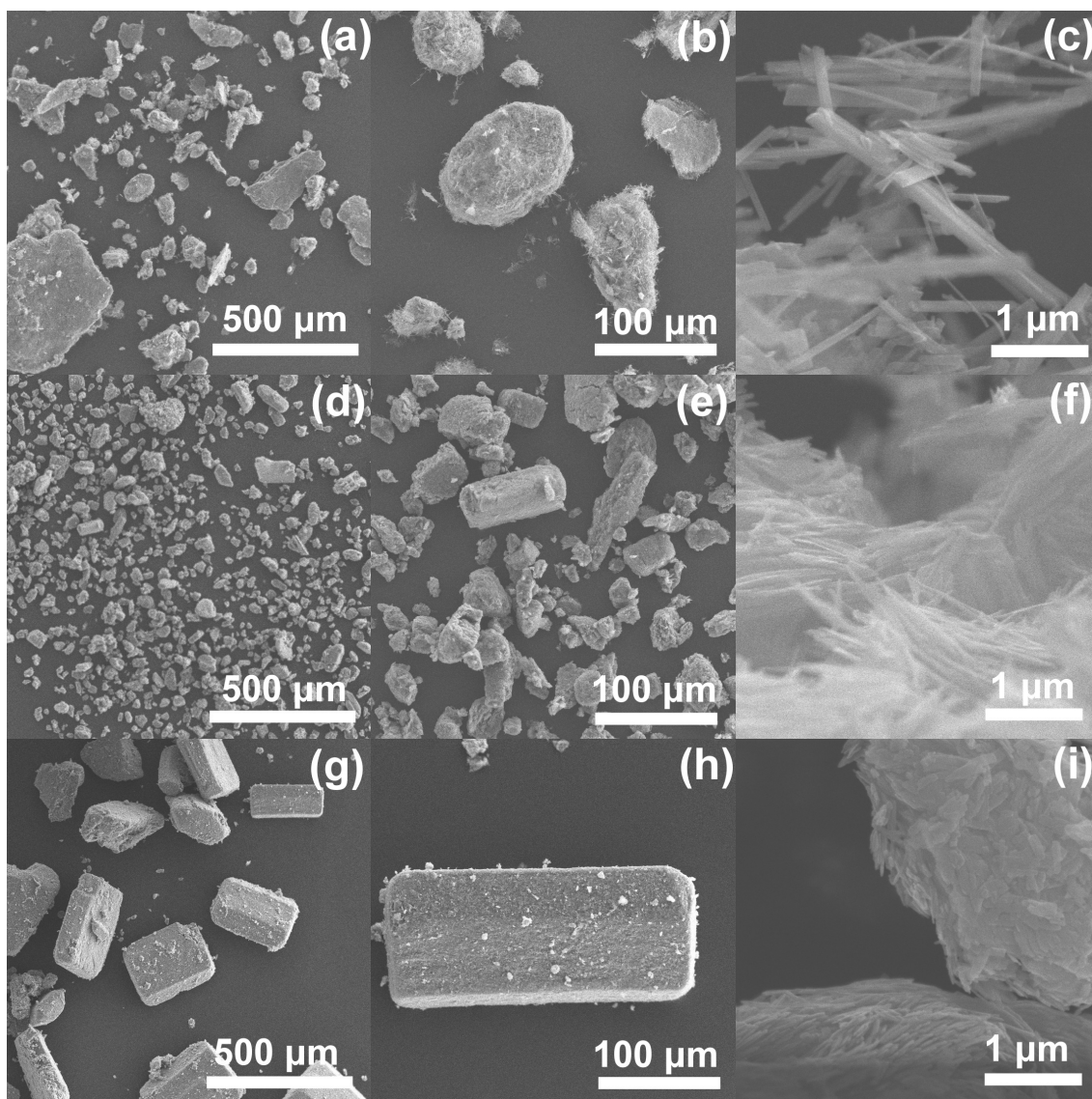


Figure 27: Scanning electron microscopy images of samples prepared via microwave synthesis at varying reaction times. Samples were prepared at 180°C for (a) – (c) 1 hour, (d) – (f) 3 hours and (g) – (i) 6 hours. There is a noticeable change in particle morphology and assembly with increasing time.

**3.3.1.2 Scanning Electron Microscopy** Figure 27 shows the scanning electron microscopy results for products synthesised at 180°C with increasing reaction times. The images increase in magnification from left to right. Images (a) to (c) are for the products of the 1 hour synthesis. Looking at (c), the highest magnification for this

product, the nanoparticles look rod-like in morphology, with a length of a few  $\mu\text{m}$  and width of 250 nm.

For the 3 hour product, at 150x magnification,(e), the nanoparticles are starting to assemble into symmetrical shapes rather than just clustering, as in (b). The nanoparticles in (f) are more needle-like in morphology rather as opposed to rod-like, with a typical width of around 50 nm and a length again of a few  $\mu\text{m}$ . This correlates with the X-ray diffraction pattern (see Figure 24), which indicated that the nanoparticles would be smaller in size than the other synthesis products.

Interestingly, for the 6 hour synthesis product ((g) – (i)), the nanoparticles have self-assembled into cuboid-like structures. Looking at the highest magnification, (i), it can be noticed that the nanoparticles are flake-like in appearance, yet have stacked themselves on top of each other to form the symmetrical cuboids. They are also shorter in length (around 500 nm) and are 100–200 nm in width. Future work would be to see how this could perform in a battery due to the assembly occurring during in the synthesis, but this would be destroyed by grinding to give a cathode disc.

In 2007, Tian *et al.*<sup>106</sup> described a new synthesis method for  $\text{VO}_2(\text{B})$ . Scanning electron images in their work appear very similar to product (6 hour run) presented here. The crystals again have self assembled into a three-dimensional superstructure. In their paper they describe a possible method of formation into this structure, where it is suggested that  $\text{VO}_2$  would nucleate in a low temperature area of the reaction vessel. Here the other molecules are then deposited on growth fronts from these nucleation sites, due to the balancing of local charge, total energy and structural symmetry. This would create a low energy surface, the flat surfaces. It is possible that this exact mechanism occurred due to the lower temperatures used in the method described in this study ( $180^\circ\text{C}$  Vs  $600^\circ\text{C}$ ).

The  $\text{VO}_2(\text{B})$  produced by Tian *et al.*<sup>106</sup> is around 200 nm in size larger than those synthesised in this study. The smaller particle size could be an advantage in battery

cycling, as it increases the surface area available for the interaction with lithium ions.

### 3.3.2 Characterisation of VO<sub>2</sub>(B) prepared via microwave synthesis at varying reaction temperatures

**3.3.2.1 X-ray Diffraction** Figure 28 shows the X-ray diffraction patterns for products from microwave synthesis over a period of 1 hour. The temperature was then changed for each run to see if there was an affect on the structure and morphology. From the previous pattern (see Figure 24), 6 hours is needed to synthesise VO<sub>2</sub>(B), and so running the experiment for 1 hour seems unlikely to form VO<sub>2</sub>(B) below 180°C. This was confirmed when the data were compared, all samples displaying peaks from V<sub>6</sub>O<sub>13</sub> and V<sub>3</sub>O<sub>7</sub>. The peak at  $2\theta=26^\circ$  can, however, be assigned to VO<sub>2</sub>(B) or V<sub>2</sub>O<sub>5</sub> or the precursor. It is, however, noticeable that there is a change in composition of the products, with an evolution from 150 up to 200°C. The 200°C product, when compared with X-ray diffraction patterns for the solvothermal products (see Figure 21), is the most advanced towards completion, which was to be expected.

It is possible, with the use of higher temperatures, that the reaction time can be brought down further. This was attempted, but due to pressure restrictions within the vessel and safety features built into the microwave oven the experiment was not taken above 200°C. Future work could investigate other higher boiling point solvents.

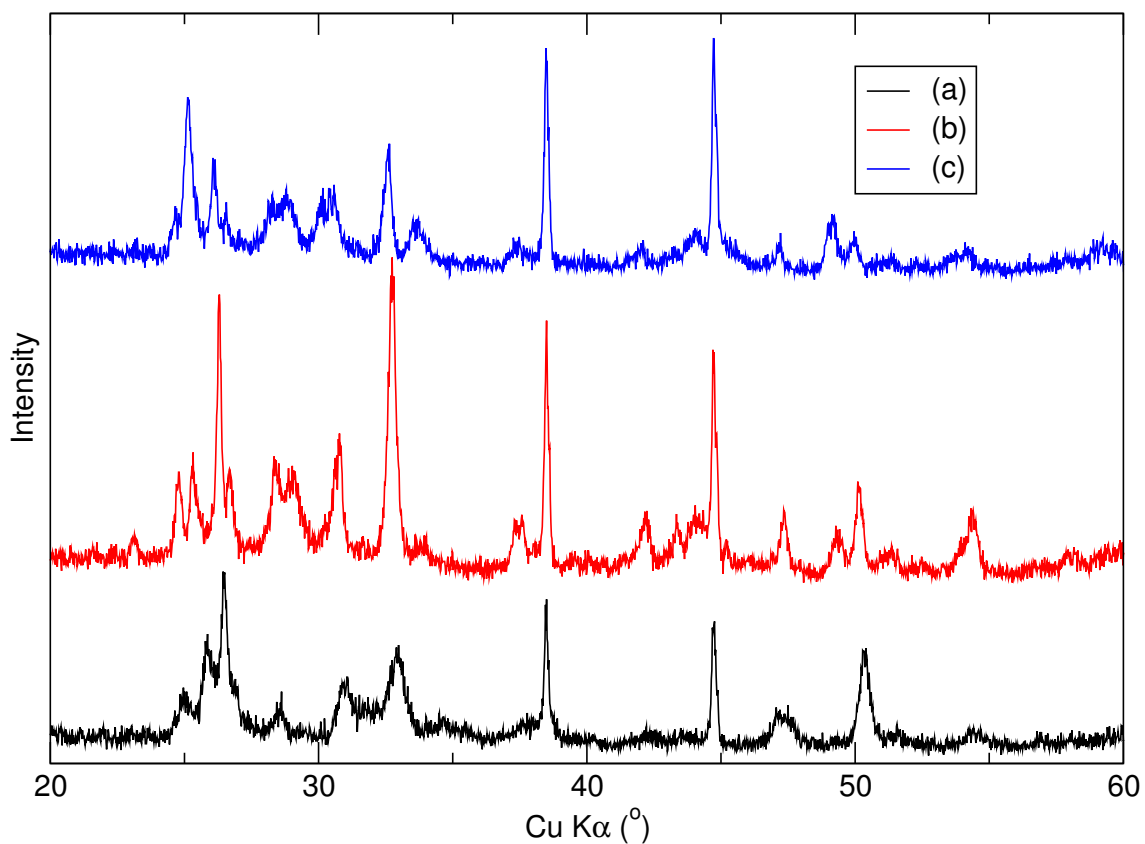


Figure 28: X-ray diffraction pattern of VO<sub>2</sub>(B) prepared via microwave synthesis using V<sub>2</sub>O<sub>5</sub> and formaldehyde for 1 hour at (a) 150°C (b) 180°C and (c) 200°C. Samples were ground and mounted in an aluminium sample holder. As the temperature increases it can be noticed that there is a change of phase present. (b) and (c) are more similar than that of (a) which shows that the reaction progresses quicker with a higher temperature.

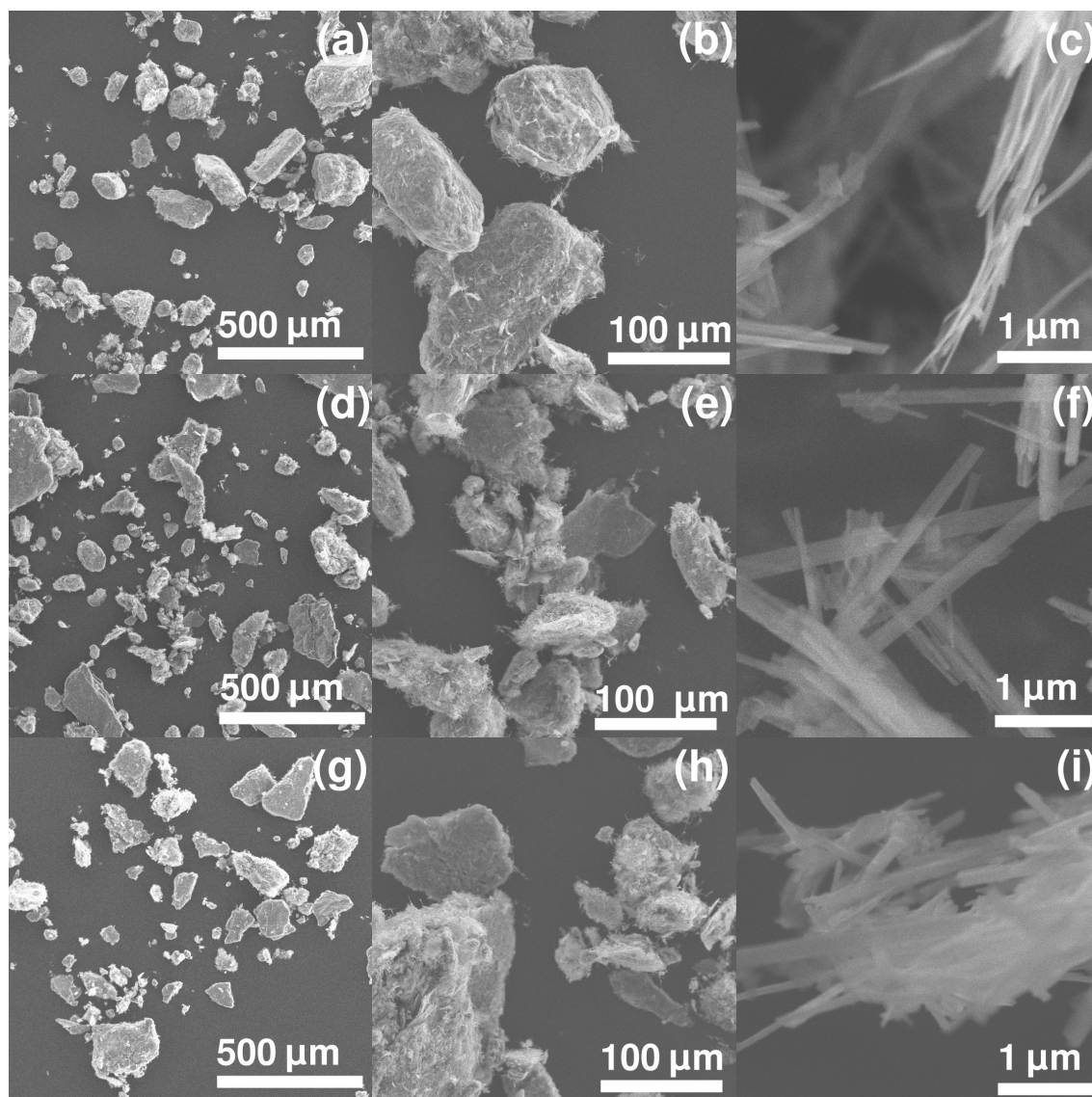


Figure 29: Scanning electron microscopy images of samples prepared via microwave synthesis at varying reaction temperatures. Samples were prepared over one hour at (a) – (c) 150°C, (d) – (f) 180°C and (g) – (i) 200°C. There is a noticeable change in particle width and length with increasing temperature.

**3.3.2.2 Scanning Electron Microscopy** Figure 29 shows scanning electron microscopy images taken of products from synthesis at varying reaction temperatures over 1 hour. Figures 29 (a)–(c) represent the run carried out at 150°C, (d)–(f) at 180°C and (g)–(i) at 200°C.

All of the samples look similar for the first two magnifications, and it is not until the highest magnification is looked at that there is a noticeable difference in the product samples. Figure 29 (c), which was made at 150°C for 1 hour, has a very fine needle-like morphology. The average width is roughly 50 nm with a length of 2 – 3 μm.

Figure 29 (f), for the product at 180°C, shows a slight increase in size of the nanorods, with a thickness increasing to around 250–300 nm, with the length staying the same at 2 – 3 μm in length.

In Figure 29 (i), the product at 200°C, the rods stayed around the same thickness and length as in the previous image (f). On referring back to the original X-ray diffraction pattern for the materials giving these scanning electron microscope images (Figure 28), there is little difference between the products made at 180 and 200°C.

### 3.4 Discussion

The goal of this work was to find new routes to synthesise vanadium oxides. By using microwave synthesis rather than solvothermal synthesis in an autoclave or Parr bomb, the aim was to reduce the reaction time. Shorter reaction times would enable more reactions to be carried out in an attempt to optimise VO<sub>2</sub>(B) for use as a cathode within rechargeable lithium-ion batteries. The current reaction time needed when using solvothermal synthesis is 48 hours, which is quoted in a number of papers.<sup>105,111–114</sup> From following one of these methods exactly,<sup>105</sup> it was ascertained that the reaction time to ensure complete reaction could be brought down to 24 hours without making any changes to the method (see Figure 21).

The reaction was then carried out in a microwave oven synthesiser to reduce the synthesis time further. There is no reported research mentioning the use of microwave assisted solvothermal synthesis in relation to VO<sub>2</sub>(B). The reaction temperature was kept at 180°C and the time was altered to optimise the experiment. Reaction times used were 1, 3 and 6 hours (see Figure 24). As the 6 hour method appeared to lead to completion,

the product standard was compared with the X-ray diffraction data gained from the earlier 48 hour solvothermal run (see Figure 25). The comparison shows that the sample has indeed reached completion as the two patterns are virtually indistinguishable. This means that the shorter reaction time allows complete synthesis of  $\text{VO}_2(\text{B})$ , which in turn means a more efficient synthesis process with a higher throughput. Further optimisation would allow the reaction time to be lowered even more, to between 3 and 6 hours through the use of microwave assisted solvothermal synthesis.

This reaction over 1 hour was examined at temperatures from 150 up to 200°C. The idea was, as mentioned, to observe the product evolution over a set time period, and to document what effect temperature would have on the product (see Figure 28). The patterns are all very different, with the 200°C looking closest to completion. Tests were carried out in an attempt to increase the temperature even more, but the pressure in the vessel became too high and the safety protocols built into the microwave oven prevented the experiment from continuing. This experiment could be continued by using a higher boiling point solvent to see if it is possible to synthesise  $\text{VO}_2(\text{B})$  at 300°C for example, over a 1 hour period.

Higher reaction temperatures would also lower the reaction times as Figure 28 shows; the figure indicates that there is an increased evolution of the sample towards the final product at higher temperatures, even over the short reaction time of 1 hour. Higher temperatures could be achieved with the use of a different solvent with a higher boiling point to prevent excessive pressures arising.

Upon looking at the scanning electron microscopy images, the microwave oven reaction carried out over 6 hours at 180°C shows a very interesting arrangement of the crystals. They seem to form plate-like structures which then become a regular shaped cuboid. This has already been noted by Tian *et al.*,<sup>106</sup> who used a tube furnace at 600°C, ammonium metavanadate and vanadium powder, and they have suggested a formation mechanism (briefly described in Section 3.3.1.2). Future work could see how these materials would function as a battery cathode given the three-dimensional superstructure

formation. Even the scanning electron microscopy images for the products if the 3 hour run, where the  $\text{VO}_2(\text{B})$  has the smallest particles, would be interesting due to the nanoneedle-like structure they are exhibiting, as well as a regular self-assembly like in the product after 6 hours.

From the work carried out so far, the optimal conditions have lowered the synthesis time period of 48 hours down to 6 hours, through using microwave synthesis as opposed to a more standard solvothermal synthesis methods. It will allow more cathodic material to be produced per unit of time for use in batteries if the product is proven to be useful inside a rechargeable lithium-ion battery.

### 3.5 Future work

Literature on this subject<sup>105,111-114</sup> reports that the final morphology of the product can be altered in many ways. The use of a microwave synthesiser to produce  $\text{VO}_2(\text{B})$  has been shown here to offer a new morphology, differing from that of the products of solvothermal synthesis in a Parr bomb. Another approach may be to alter the starting reactants. Figure 30 shows the XRD patterns obtained when the starting vanadate was changed from  $\text{V}_2\text{O}_5$  to  $\text{NH}_4\text{VO}_3$ . All reactions were carried out through solvothermal synthesis in a PTFE lined Parr bomb cell. The reaction times were altered to observe the evolution of the sample over a period of time. As can be seen, there is not a lot of difference between the XRD patterns of the samples and the final products are not  $\text{VO}_2(\text{B})$ .

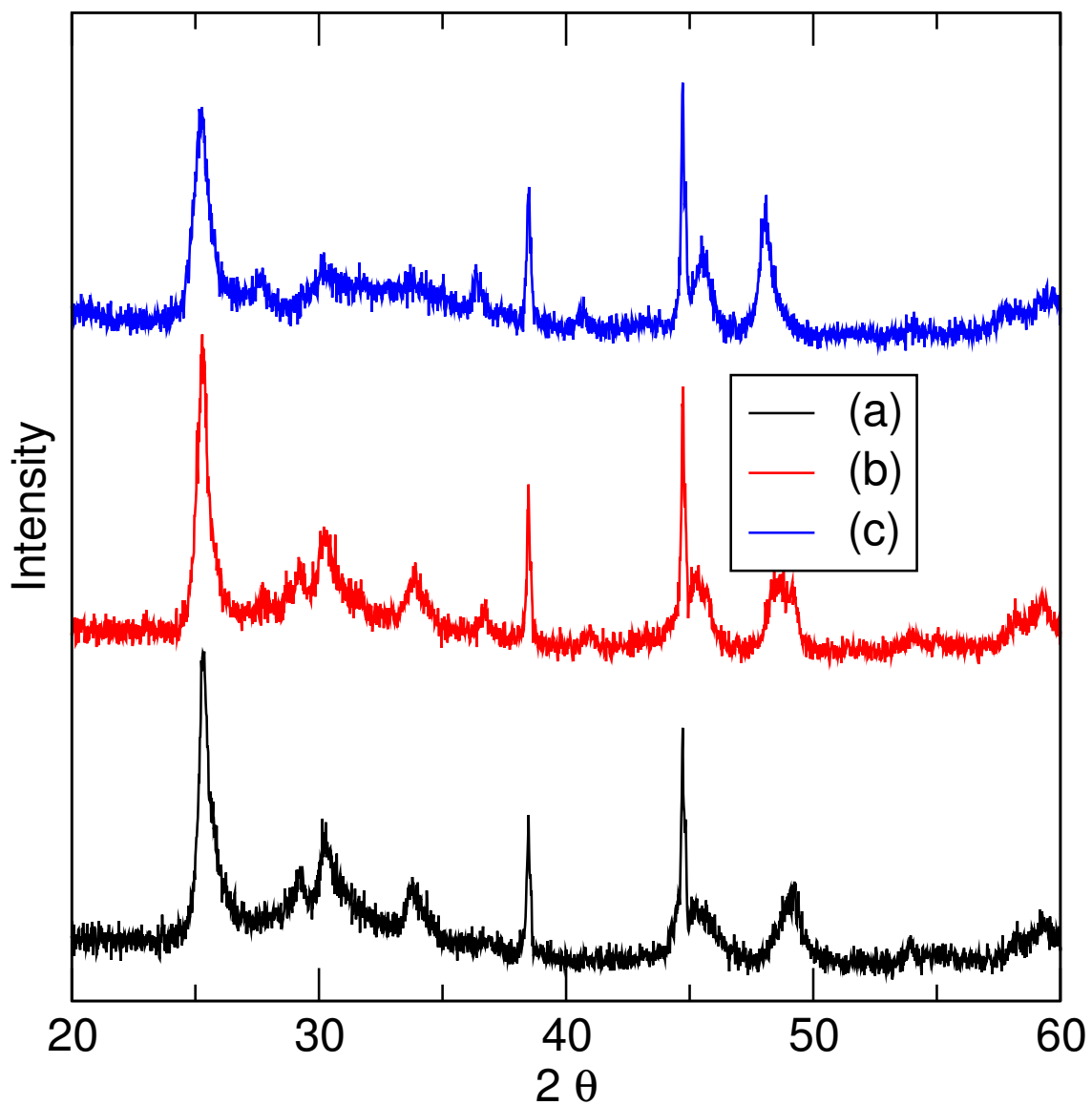


Figure 30: X-ray diffraction patterns showing products after  $\text{NH}_4\text{VO}_3$  being used as the starting vanadate and using formaldehyde. Samples were ground and mounted in an aluminium sample holder. Synthesis was carried out in a PTFE lined Parr bomb cell. The reaction times were varied to see if there was any significant difference. (a) refers to the run carried out over 12 hours, (b) is for 24 hours and (c) was carried out over 48 hours.

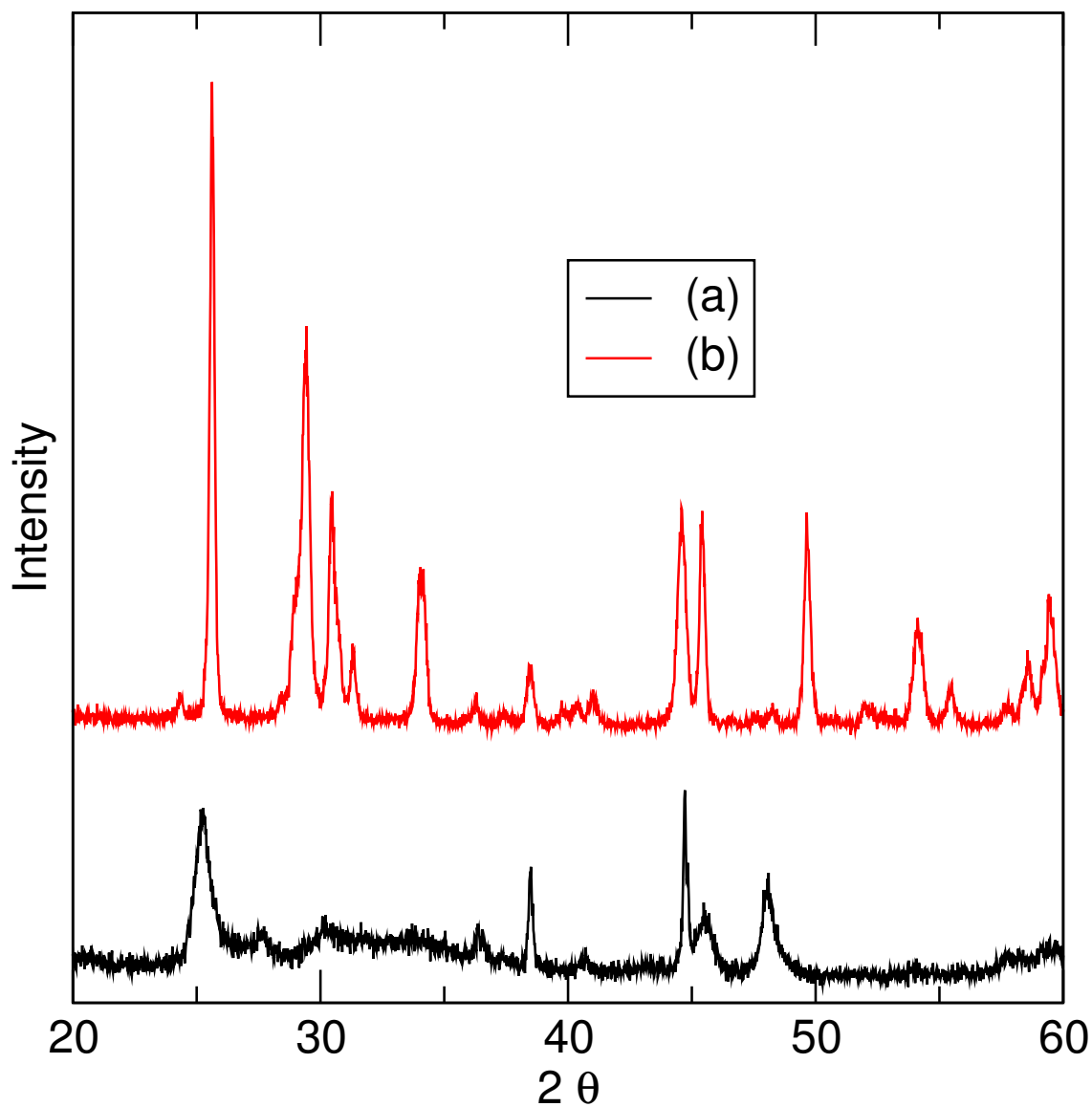


Figure 31: X-ray diffraction pattern of  $\text{VO}_2(\text{B})$  synthesised in a PTFE lined Parr bomb cell with aqueous formaldehyde. Samples were ground and mounted in an aluminium sample holder. Reactions were carried out with different starting vanadates,  $\text{V}_2\text{O}_5$  and  $\text{NH}_4\text{VO}_3$  being used, and the reaction times were both over 48 hours. (a) refers to use of  $\text{NH}_4\text{VO}_3$  and (b)  $\text{V}_2\text{O}_5$

Figure 31 shows the comparison between XRD patterns for products of the 48 hour runs using  $\text{V}_2\text{O}_5$  and  $\text{NH}_4\text{VO}_3$ , where the solvent was kept as aqueous formaldehyde. There

are a number of peaks missing from data set (a) when compared to (b), namely those at  $29^\circ$ ,  $31^\circ$ ,  $34^\circ$  and  $55^\circ$   $2\theta$ . This would suggest that further investigation is required to successfully prepare  $\text{VO}_2(\text{B})$ .

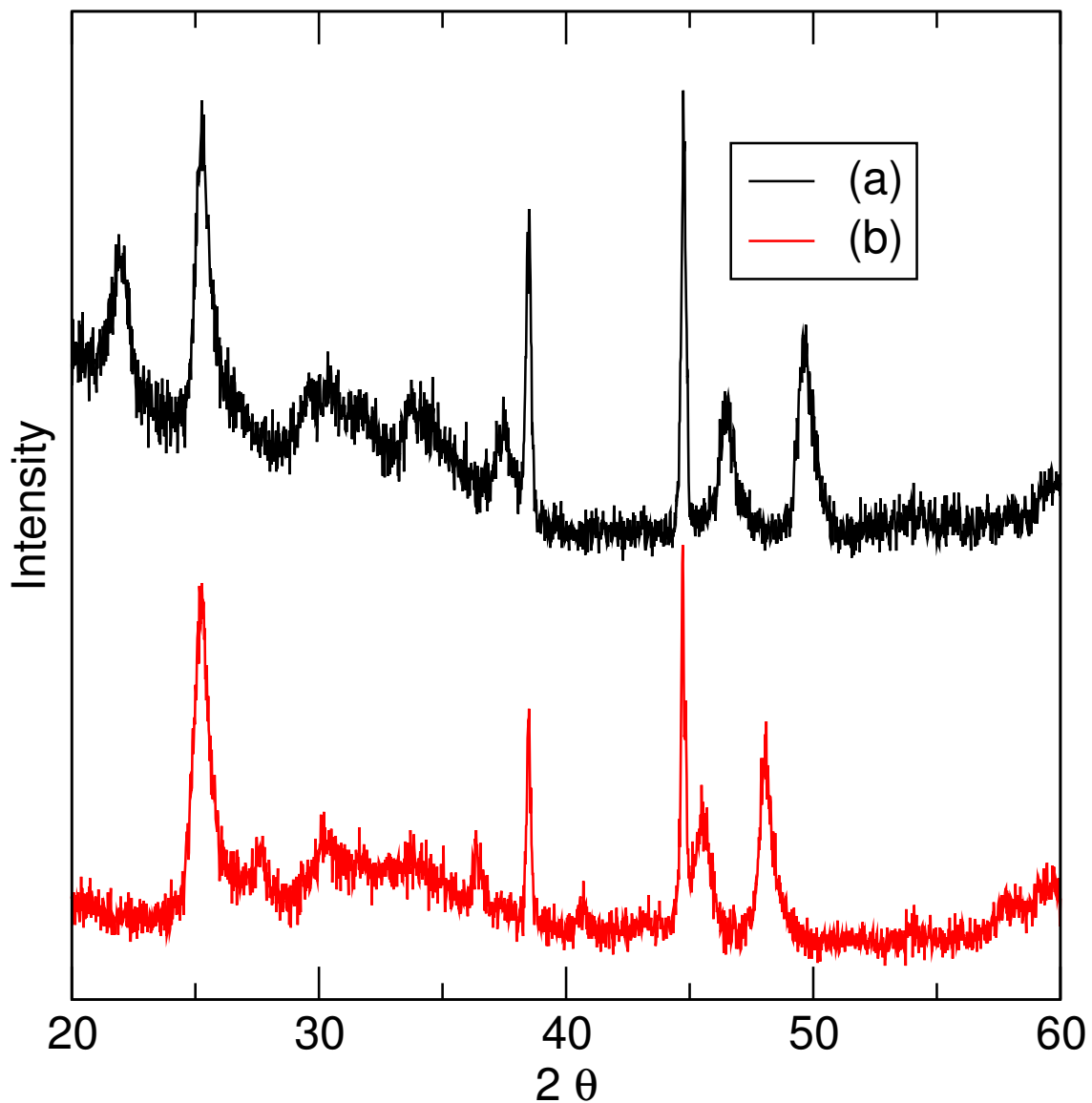


Figure 32: X-ray diffraction pattern of  $\text{VO}_2(\text{B})$  synthesised using  $\text{NH}_4\text{VO}_3$  and formaldehyde as the starting materials. Samples were ground and mounted in an aluminium sample holder. (a) was carried out using microwave synthesis for  $180^\circ\text{C}$  for 6 hours. (b) was carried out in a PTFE lined Parr bomb cell at  $180^\circ\text{C}$  for 48 hours.

Having carried out experiments under solvothermal and microwave synthesis with  $\text{NH}_4\text{VO}_3$  as the starting vanadate and use of formaldehyde, Figure 32 compares the resulting XRD patterns. Figure 32 (a) is the data for the microwave synthesis product prepared at  $180^\circ\text{C}$  for 6 hours, while Figure 32 (b) is for that under solvothermal synthesis conditions at  $180^\circ\text{C}$  for 48 hours. The patterns are very similar, yet there is an extra peak in the data for the microwave oven product at  $2\theta=23^\circ$ . This could be due to starting materials being present and further analysis would be needed to confirm this. Further testing needs to be carried out to optimise alternative synthesis of  $\text{VO}_2(\text{B})$ .

## 4 Battery Applications of Vanadate Materials

### 4.1 Potentiostat use in battery characterisation

EXAFS experiments have already been carried out on some lithium-ion battery cathodes, for example  $\text{LiFePO}_4$ .<sup>115</sup> Deb *et al.* studied the atomic and electronic structure of  $\text{LiFePO}_4$  and  $\text{FePO}_4$ , through the use of *in situ* X-ray absorption fine-structure spectroscopy (XAFS) measurements. The cell was tested at typical Li-ion battery operating voltages of 3.0–4.1 V versus  $\text{Li}/\text{Li}^+$ . XAS studies of the  $\text{LiFePO}_4$  electrode measured at the initial state of  $\text{LiFePO}_4$  showed iron to be in the Fe(II) state, which corresponds to the initial state of the battery at 0.0 mAh.  $\text{FePO}_4$  was also studied in the delithiated state and the iron in  $\text{FePO}_4$  was found to be in the Fe(III) state, which corresponds to the final charged state of 3 mAhh in the battery.

They found that for long periods of cycling, the iron ions are always octahedrally coordinated in an  $\text{Fe}^{+2}$  state, and also that the structure of  $\text{LiFePO}_4$  did not change. This therefore allowed them to theorise that  $\text{LiFePO}_4$  could be an excellent choice for long cycle life lithium-ion battery applications.

The electrochemical cell that was used for this experiment is one that has been recently designed for specific use with X-ray diffraction or X-ray absorption experiments at a synchrotron facility.<sup>116</sup> The cell was designed and tested by Morcette *et al.*, initially on  $\text{LiFePO}_4$ . The cell is based upon the commonly used Swagelok <sup>TM</sup> configuration, with the exception of it being available for use in XRD and XAS experiments. Figure 36 shows the cell *in situ* in the beam line ready for XAS experiments to be performed. As of yet, there have been no *in situ* studies carried out as to the near neighbour structure of  $\text{VO}_2(\text{B})$  nanorods throughout a discharge cycle.

Battery cell testing using a  $\text{VO}_2(\text{B})$  cathode prepared by solvothermal synthesis was carried out prior to X-ray spectroscopy (XAS) experiments. The battery was charged and discharged, using a BioLogic potentiostat, from 2.0 to 3.0 V under standard ambient

conditions. Figure 33 demonstrates that over 20 cycles  $\text{VO}_2(\text{B})$  has a reversible capacity of  $0.6 \text{ Li}^+$  at a  $\text{V}^{+4} / \text{V}^{+3}$  redox voltage throughout the cycling of  $2.5 \text{ V}$ , which can be read from the plateau in the figure. Vanadium (II) typically has a redox potential of  $2.85 \text{ V}$  vs Li and  $\text{VO}_2(\text{B})$  a insertion capacity of  $0.5 - 0.85 \text{ Li/V}$ .<sup>117,118</sup> This shows that the results obtained in this study are similar to reported values. Through coating, doping or alteration of reaction time and temperature, it may be possible to improve the reversible capacity in future studies. Redox potential, however, cannot be improved however due to thermodynamics.

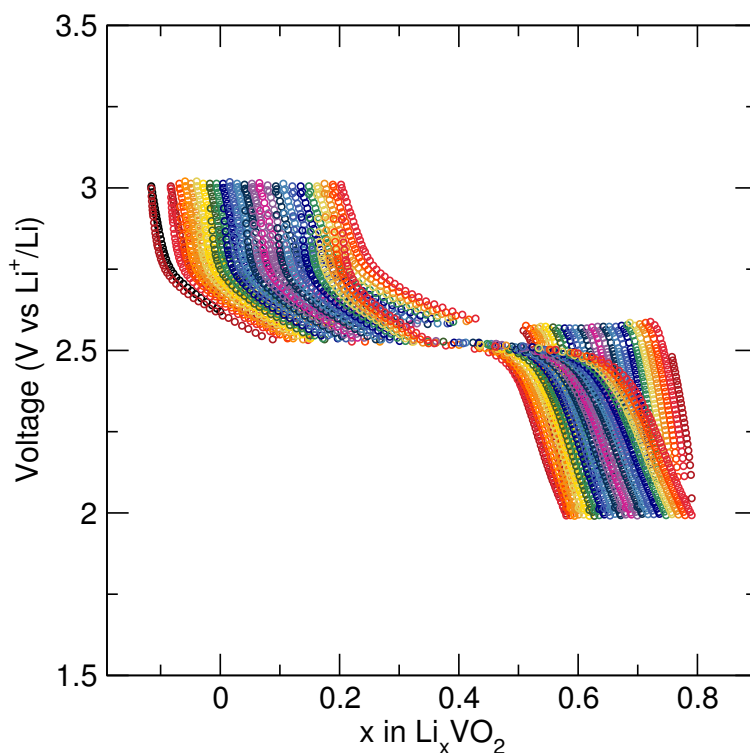


Figure 33: Charge and discharge curve for  $\text{VO}_2(\text{B})$  at a discharge rate of  $\text{C}/10$ . The battery was cycled from  $2.0$  to  $3.0 \text{ V}$  and the redox potential plateau lies at  $2.73 \text{ V}$ . Cycling was carried out under standard ambient conditions ( $25^\circ\text{C}$  and  $100 \text{ kPa}$ ). Colours are used to represent different cycles.

## 4.2 In situ X-ray spectroscopy (XAS) studies

### 4.2.1 Pure VO<sub>2</sub>(B) sample

XAS measurements were taken for VO<sub>2</sub>(B) before cycling. This sample was prepared via solvothermal synthesis, as detailed in chapter 2, and has a nanorod-like morphology. For the XAS experiments, 4 mg of VO<sub>2</sub>(B) was mixed with 140 mg of boron nitrate, which was pressed into a pellet. This was to allow the X-rays to pass through the sample, as boron nitrate is neutral to the beam and so would not affect the results. The sample was then placed in the beamline and XANES spectra were recorded on the V K-edge (see Figure 34).

Figure 34(a) shows the normalised XANES data obtained. The pre-edge absorption feature can be seen clearly at 5480 eV. At 5486 and 5489 keV, a doublet is noted, which is indicative of V<sup>4+</sup>.<sup>119</sup> A Fourier transform of the EXAFS data is shown in figure 34(c). At 1.500 Å there is a peak which may be attributed to the V–O bonds, as described by Andersson, who reported a V–O bond distance of 1.76Å.<sup>120</sup> The next two peaks, at 2.44 and 3.031 Å, represent the two different bond lengths that occur between the vanadium atoms in the VO<sub>2</sub>(B) phase. At low temperatures (below 300 K), this structure is characterised by a dimerisation of the V<sup>4+</sup>–V<sup>4+</sup> ions giving rise to the two bond lengths between V<sup>4+</sup>–V<sup>4+</sup>.<sup>1</sup>

### 4.2.2 VO<sub>2</sub> prepared as a Bellcore Film for in situ cycling

To make the Bellcore film, the VO<sub>2</sub>(B) was mixed with carbon black, dibutyl phthalate and Kynar polymer to make a thin film of material. This film, with a density of active material of 3.76 mgcm<sup>-3</sup>, was then placed in a Swagelok<sup>TM</sup> battery cell, with lithium acting as the anode and LP30 (1M LiPF<sub>6</sub> in ethylene carbonate–dimethyl carbonate (1:1 wt/wt)) as the electrolyte. The battery was placed on the B18 Quick EXAFS beamline at the Diamond Light Source and XAS data was collected as the battery cycled. First,

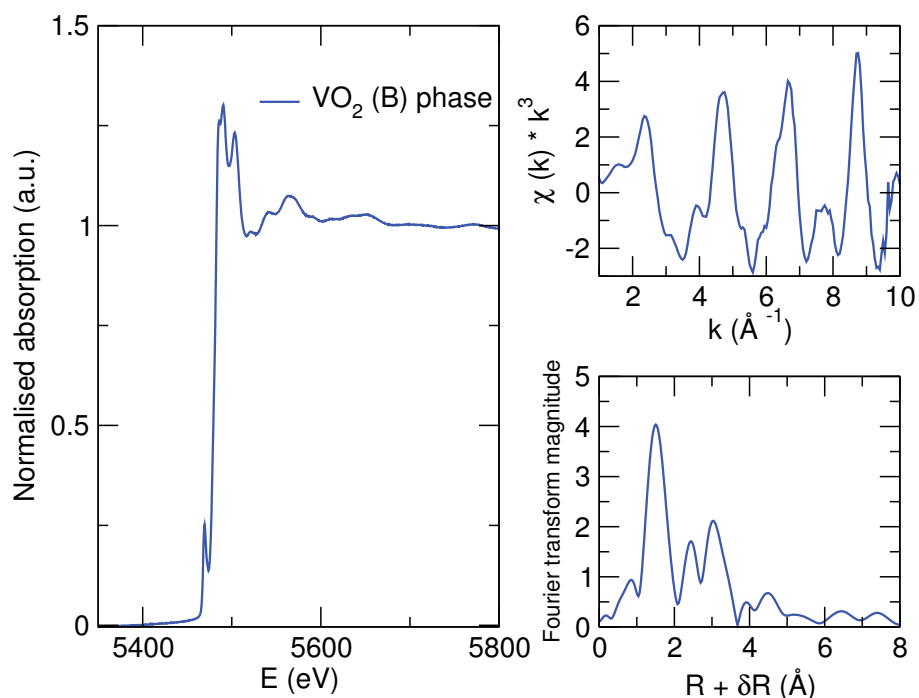


Figure 34: (a) XANES, (b) EXAFS data and (c) Fourier transform of EXAFS data for VO<sub>2</sub>(B). In (a), a pre-edge feature is located at 5480 keV. The doublet noted at 5486 and 5489 keV is a feature found for the V<sup>4+</sup> oxidation state. (b) shows the chi data extracted from the averaged EXAFS data, while (c) shows the Fourier transform of this data. The Fourier transform of the EXAFS (c) reveals nearest neighbour bond distances. Here, the peak at 1.500 Å is for a V–O bond, while the two peaks at 2.44 and 3.031 Å are for the alternating short and long bond distances expected for VO<sub>2</sub>(B).<sup>1</sup>

XANES data were collected for the cathode before cycling. This is shown in Figure 35.

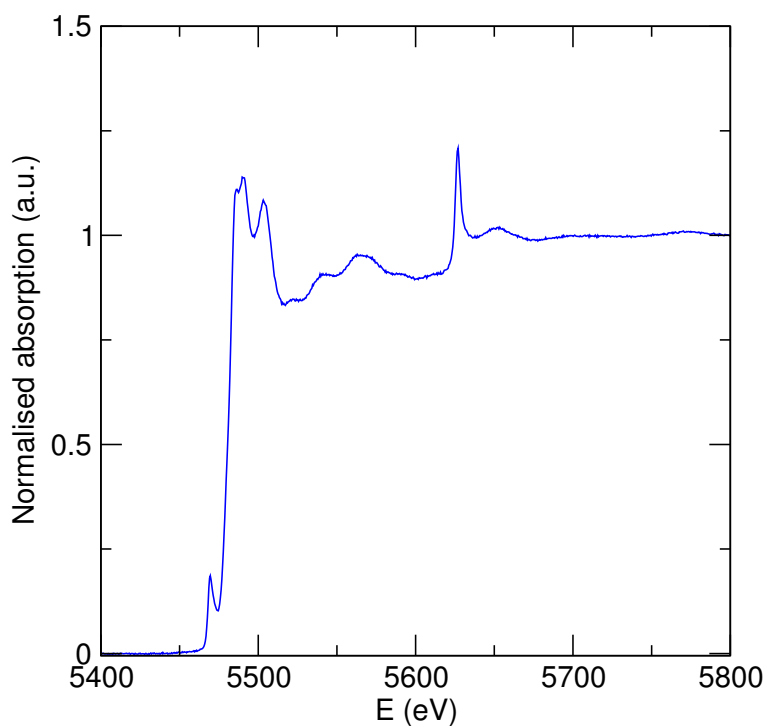


Figure 35: XANES data of  $\text{VO}_2(\text{B})$  Bellcore film in a lithium-ion battery cell. Unfortunately, unlike the Powder data, there is a barium peak in the EXAFS region at 5640 eV, due to the presence of a barium impurity in the battery separator. This makes it impossible to analyse this region and obtain EXAFS data. The XANES profile is the same as the powder results (see Figure 34).

The peaks for  $\text{VO}_2$  were again noted, but a new feature was seen at 5640 K. This has been attributed to a barium impurity in the glass mesh which acts as a separator between the cathode and the anode. Because of the location of these barium peaks, it is not possible to obtain EXAFS data for the *in situ* sample. However, useful information may be garnered from the XANES. Future experiments could be carried out using a polymer as the separator to eliminate the barium impurities.

### 4.3 In situ charge–discharge measurements

*In situ* measurements were taken of the VO<sub>2</sub>(B) sample and XANES spectra were recorded on the V K-edge as the battery cycled so that any structural transformations could be observed. A photograph of the experimental set-up is shown in Figure 36. The synchrotron radiation passed through the cell from the right hand side to the left hand side of the images while the battery was being cycled.

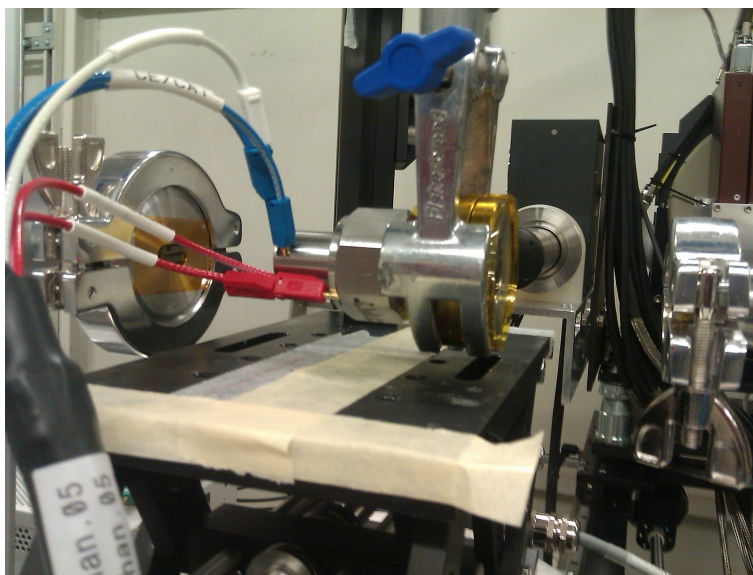


Figure 36: Experimental set-up of the battery cell at the B18 Quick EXAFS beamline at the Diamond Synchrotron source. The synchrotron radiation entered from the right hand side of the image, travelled through the cell and out the other side.

Figure 37 shows the XANES data obtained for one cycle. Each line on the graph relates to a point on the charge–discharge cycle. (a) is from the start of the discharge down to (f), where the battery started to charge again. The corresponding charge–discharge curve is plotted in Figure 39.

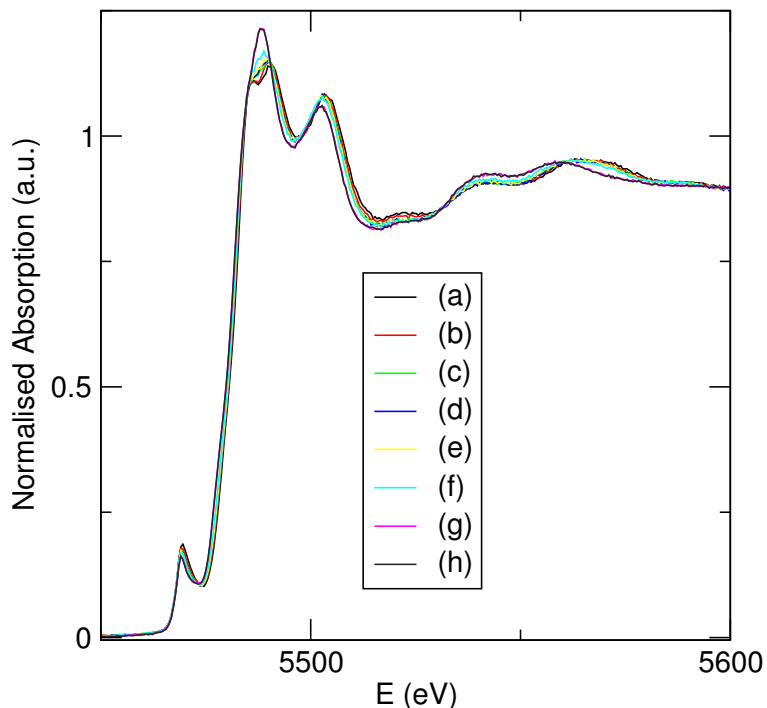


Figure 37: XANES data collected during a cycle, with (a)–(h) representing different points on the charge–discharge cycle (see Figure 39). The data show that there is a big change in the XANES region, most notably the first peak.

Figure 38 is the XANES region shown in greater detail. As can be seen from data set (a), there are two peaks present in the first major peak, one at 5486 eV and the other at 5490 eV. The interesting point to note is that as the battery discharges, these two peaks merge to become one peak as well as increasing in intensity. Data sets (e) and (f) show this disappearance of the dual peak. When the battery starts to charge again, as lines (g) and (h) show, there is an increase in peak intensity. This shift in energy and change in intensity can be attributed to the alteration of the  $\text{VO}_2(\text{B})$  structure to allow the access and egress of the lithium ions and electrons into it throughout the charge and discharge cycle. Wong *et al.* have previously carried out experiments looking at the K–absorption edges of vanadium compounds.<sup>119</sup> From comparison of their work with Figure 38, it is possible to establish the oxidation state of the vanadium ions. At (a) and (b), the sample is comparable to the K–absorption edges of  $\text{V}_2\text{O}_4$  and  $\text{VO}_2$ , due

to the peaks at 5486 eV and 5490 eV respectively. This indicates that the vanadium is in a  $V^{+4}$  oxidation state at the start of the discharge process as expected. Curves (g) and (h) from Figure 38 shows the same profile as  $V_2O_3$ .<sup>119</sup> From this, we can conclude that the vanadium in our sample is in a  $V^{+3}$  oxidation state at the end of the discharge process. This change in oxidation state can be explained by the uptake of lithium ions, and gain of electrons through the discharge process. Curves (d) – (f) have a similar profile to the mixed valence oxide  $V_4O_7$ , which possesses both  $V^{+4}$  and  $V^{+3}$  oxidation states. This can be seen on Figure 38 by the change of the first peak as seen in (a), to a shoulder of the second peak at 5490 eV.

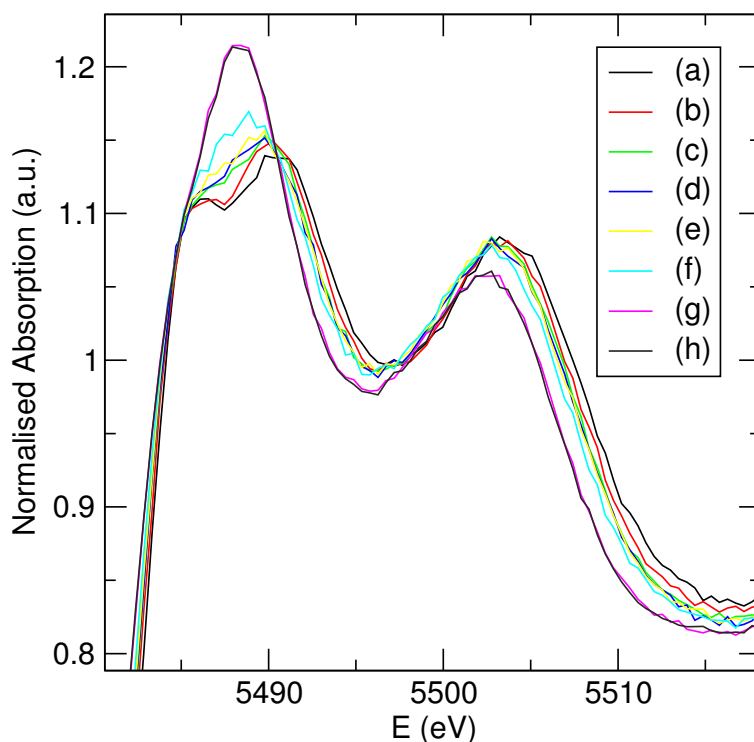


Figure 38: Highlighted XANES region of the V K-edge during the  $VO_2(B)$  cycle. The data start at (a) and end with (h) and it can be seen that the initial peak goes from having a shoulder to being just one peak. (a) to (h) represent the spectra recorded for points on the corresponding charge–discharge curve. The change in peak positions and shape are due to changes in the  $VO_2(B)$  structure, due to the movement of lithium atoms and electrons.

Figure 39 shows the data collected from the same cycling battery. The points on the curve relate to the individual data curves in Figures 37 and 38. The curve exhibits a slightly steeper middle section between points (b) and (d) than expected as the cell potential is ideally flat. It can also be seen that when Figure 39 is compared to Figure 38, that the single peak arises as the cell completes its discharge cycle and begins to recharge.

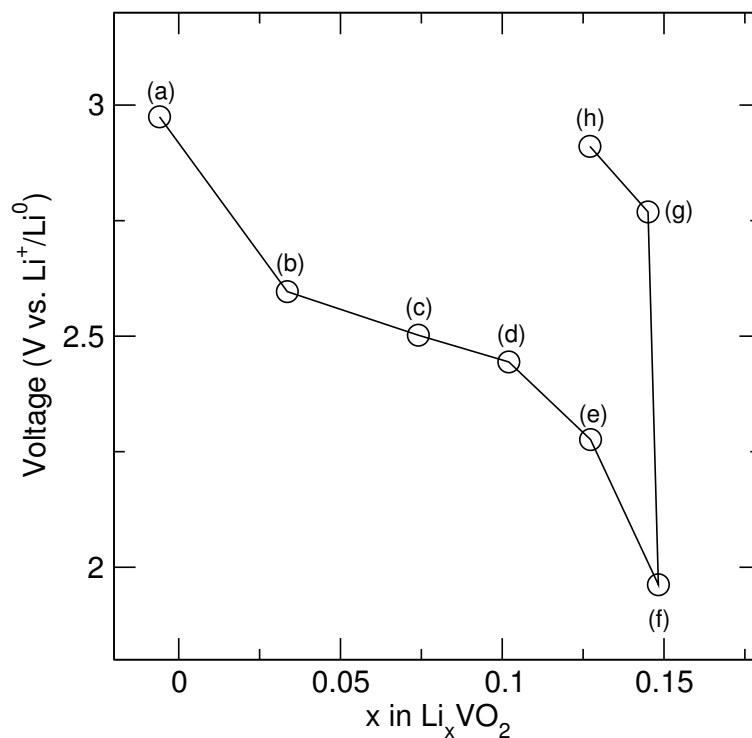


Figure 39: Charge–discharge cycle showing one dynamic cycle of the VO<sub>2</sub>(B) Bellcore film. The point on the curve related to XANES data collected during the cycle, which were shown in Figure 38. Data was collected at 3 minute intervals every 30 minutes.

#### 4.4 Conclusions and future work

As can be seen from Figure 33, the cycled VO<sub>2</sub> sample prepared using hydrothermal methods is very stable over 20 cycles between 2.0 V and 3.0 V. It will be interesting to carry out future cycling experiments on VO<sub>2</sub> samples prepared using microwave synthesis

reactions to compare the cycling stabilities. Due to the alteration in particle morphology, it is possible that differences in the cycling profiles may be observed. XANES and EXAFS experiments have revealed changes in local structure occurring in the material. In the case of the original VO<sub>2</sub>(B) sample, there are two vanadium–vanadium bond distances observed due to the local dimerisation in this compound. Data collected while the battery was being cycled shows very interesting changes in the XANES region. Looking at Figure 38, it can be seen that the peak heights and peak intensities change dramatically upon cycling, from a doublet corresponding to V<sup>4+</sup> to a single peak, corresponding to V<sup>3+</sup>. This is indicative of a change within the local structure during the cycling process, due to the the access and egress of the electrons and lithium ions into and out of the VO<sub>2</sub>(B) structure. These *in situ* techniques have given some valuable insight into the chemical changes occurring during cycling. This technique could also be applied to other cathode samples in an effort to better understand the cycling mechanisms occurring.

Future work could include re–running the *in situ* XAS experiment, but with a different separator, for example a polymer separator. This would allow for the EXAFS to be determined and give us further insight into the structural changes occurring in bonding during the cycling process. Other VO<sub>2</sub>(B) samples could also be studied in order to compare differences between the samples prepared using different synthesis pathways, for example solvothermal and microwave oven prepared VO<sub>2</sub>(B). This would also shed light on whether the morphology, varying with differing synthesis techniques, affects the battery cycling properties of the sample.

## 5 Olivine Phosphate Cathode Materials

### 5.1 Studies of Products of Microwave Synthesis

In addition to  $\text{VO}_2(\text{B})$ , preliminary microwave synthesis studies on olivine phosphate structures were also performed. Lithium cobalt oxide is the cathode currently used in commercial lithium-ion batteries. Olivine phosphate structures, however, have been accepted as excellent candidates for future cathodes, including application in hybrid electric vehicles and fully electric vehicles, due to the materials being inexpensive, non-toxic, and environmentally harmless when compared with lithium cobalt oxide.<sup>121–123</sup>

Olivine phosphate structures, in particular lithium iron phosphate, for lithium-ion batteries are typically synthesised through solid-state reactions<sup>122,124,125</sup> or solution chemistry, for example solvothermal synthesis.<sup>126–128</sup>

Previous work has also been carried out on the preparation of olivine phosphate structures using microwave assisted solvothermal synthesis and has resulted in much shorter reaction times.<sup>129–132</sup> This makes microwave synthesis an attractive, fast and cost-effective synthetic route for the preparation of cathode battery materials. The charge-discharge relevant olivine phosphates have the general formula  $\text{LiMPO}_4$ , where M here is Fe, Mn or Co. The particles here were prepared, characterised by XRD, SEM, XAS and preliminary cycling of batteries was performed.

### 5.2 Studies of Products of Microwave synthesis of $\text{LiFePO}_4$

The samples were prepared via microwave-assisted solvothermal synthesis. Briefly, iron(II) oxalate dihydrate and lithium dihydrogenphosphate were dispersed in ethylene glycol and placed in the microwave oven reactor for 2 hours at  $300^\circ\text{C}$ . Figure 40 shows the XRD pattern collected for the  $\text{LiFePO}_4$  sample obtained. This pattern was compared to  $\text{LiFePO}_4$  using the ICSD database.<sup>4</sup>

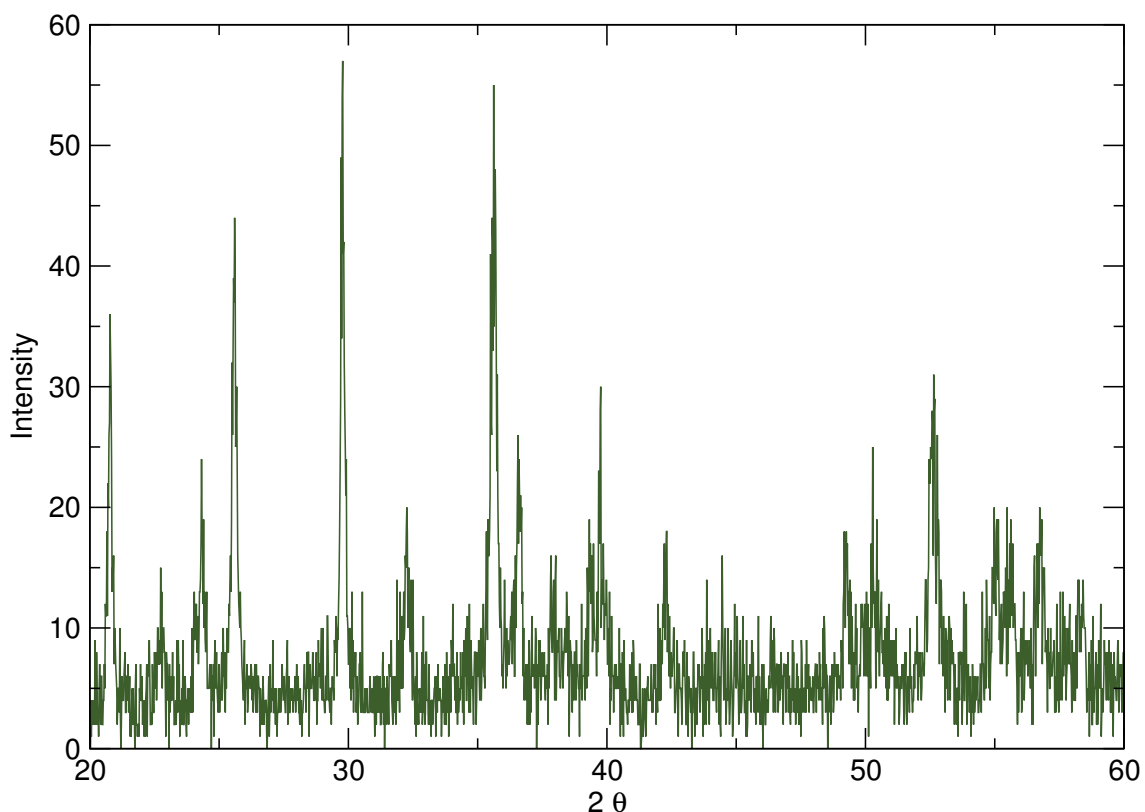


Figure 40: XRD pattern of  $\text{LiFePO}_4$  synthesised using microwave-assisted solvothermal methods. Comparison of this pattern with the reference pattern for  $\text{LiFePO}_4$  showed a good correspondence in peak positions.<sup>4</sup>

Scanning electron microscopy images were also obtained (see Figure 41). The particles are clustered and appear to have a flake-like appearance. Bauer *et al.*<sup>133</sup> and Shin *et al.*,<sup>134</sup> both synthesised  $\text{LiFePO}_4$  through solid state methods. They formed spherical aggregates, of around  $1\ \mu\text{m}$  for Bauer *et al.*<sup>133</sup> and around  $500\ \text{nm}$  for Shin *et al.*<sup>134</sup> Synthesis by Zhang *et al.*<sup>132</sup> was carried out in a microwave oven. Again, they synthesised spherical particles similar to those above. Upon comparison with the method described here, they appear similar to Figures 41(a) and (b). However, when compared with Figure 41(c), a higher magnification than (a) and (b), there is a distinct difference as flakes are seen at the higher magnification. Typical widths of  $0.5\ \mu\text{m}$ , lengths of  $1\ \mu\text{m}$  and thickness of  $0.1\ \mu\text{m}$  are present for these flakes. This could indicate that the  $\text{LiFePO}_4$

synthesised in this thesis potentially has a larger surface area than other methods which can aid in greater efficiency for a cathode. Specific surface area would have to be measured though to say for certain.

It is interesting to note that the morphologies of the resulting sample could play a large part in aiding cycling capabilities. Research carried out by Lu *et al.*<sup>135</sup> and Ellis *et al.*<sup>136</sup> looked at the cycling capabilities of different morphologies of  $\text{LiFePO}_4$ . Lu *et al.*, found that by increasing the synthesis time, the electrochemical reactivity is increased, which they ascribed to be due to enhanced ordering within the structure and the formation of a hollow structure. This hollow morphology increases the contact between the electrode and electrolyte, and therefore shortens the lithium-ion diffusion pathlength. As the reaction continues (post 15 hours), the structure begins to lose its hollow nature and the  $\mu\text{m}$  electrochemical reactivity falls, even though the particle size is decreasing.

Further research into the products synthesised here could lead to similar results to Lu *et al.*,<sup>135</sup> and an optimisation of the procedure.

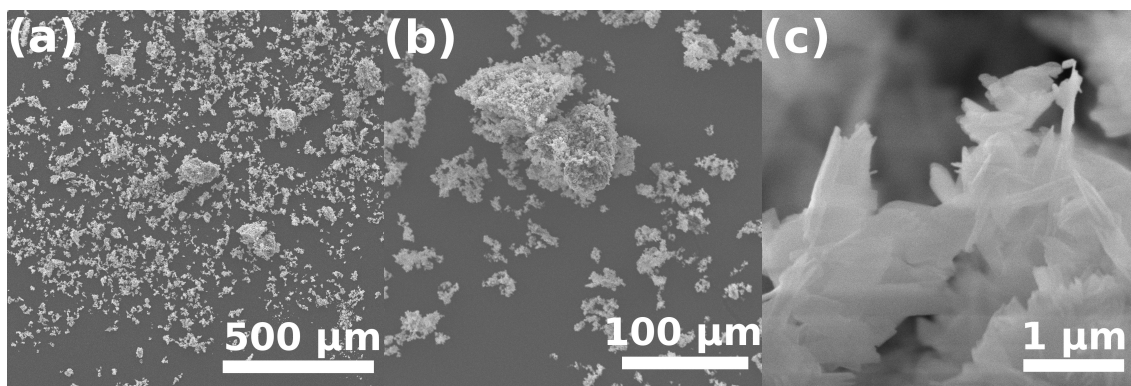


Figure 41: Scanning electron microscopy images displaying the morphology of  $\text{LiFePO}_4$ . (a) is least magnified at 60x. Here it can be seen that the sample looks almost powder-like in appearance. As the magnification increases, ((b) 250x) it can be seen that superstructures are being formed with a flocculant appearance. From this magnification they could be flakes or spherical aggregates. (c), 20kx, displays that the particles synthesised are nanoflake in morphology, with a width of approximately 0.5, length of 1 and a thickness of  $0.1 \mu\text{m}$ .

Cycling data for cells with  $\text{LiFePO}_4$  cathodes are shown in Figure 42. The cell was formed by using the  $\text{LiFePO}_4$  powder as the active component in the cathode and lithium foil as the anode, and placed within a Swagelok<sup>TM</sup> cell. This cell was then discharged to 2 V before being charged to 4.2 V. The cell was only run through a charge-discharge cycle 4 times. On both charging and discharging, the data formed a plateau with a redox potential of 3.4 V. The discharge slopes are also fairly steep, although could be made steeper with further work and potential doping or coating. The reversible capacity is  $0.5 \text{Li}^+$ .

Overall, Figure 42 shows that  $\text{LiFePO}_4$  synthesised through microwave-assisted solvothermal synthesis can produce a cathode material that maintains a good cycle curve due to the redox potential plateau at 3.4V and the fairly steep slopes either side. Future work could be carried out by cycling the cell more times to see if the structure holds its capacity as high and as long as possible.

$\text{LiFePO}_4$  was prepared for EXAFS and XANES analysis by mixing 10.5 mg of oxide with 140 mg of boron nitride and pressing into a pellet. The resulting spectra are shown in Figure 43. A paper by Zhou *et al.* looked at the resulting XAS spectra from the synthesis of  $\text{LiFePO}_4$  using solid state and hydrothermal syntheses methods, which took 18 and 2 hours respectively.<sup>137</sup> Comparing to the data from Zhou *et al.* with Figure 43, it can be seen that the XAS confirms the XRD data in that  $\text{LiFePO}_4$  had been synthesised. The pre-edge peak can be found at 7111 eV with the first major peak at 7126 eV and a second peak at 7172 eV.

The Fourier transform determines the radial structure function. Similar to the work of Zhou *et al.*,<sup>137</sup> there is a strong peak intensity at 1.533 Å. This is indicative of the first shell containing iron–oxygen bonding. The two smaller peaks later on at 2.692 and 3.635 Å can be assigned to the higher shells containing iron, phosphorus and oxygen.

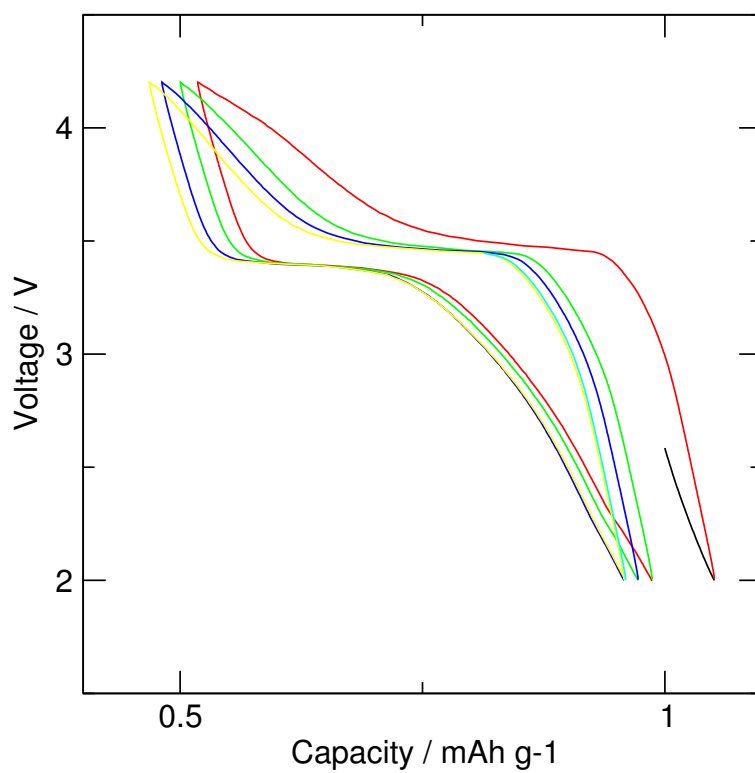


Figure 42: Cycling data for LiFePO<sub>4</sub> showing charge–discharge patterns between 4.2 V and 2 V. The cycle starts at black by discharging before then charging. Cycling experiments were carried out by Dr S. Corr and associates in Amiens, France.

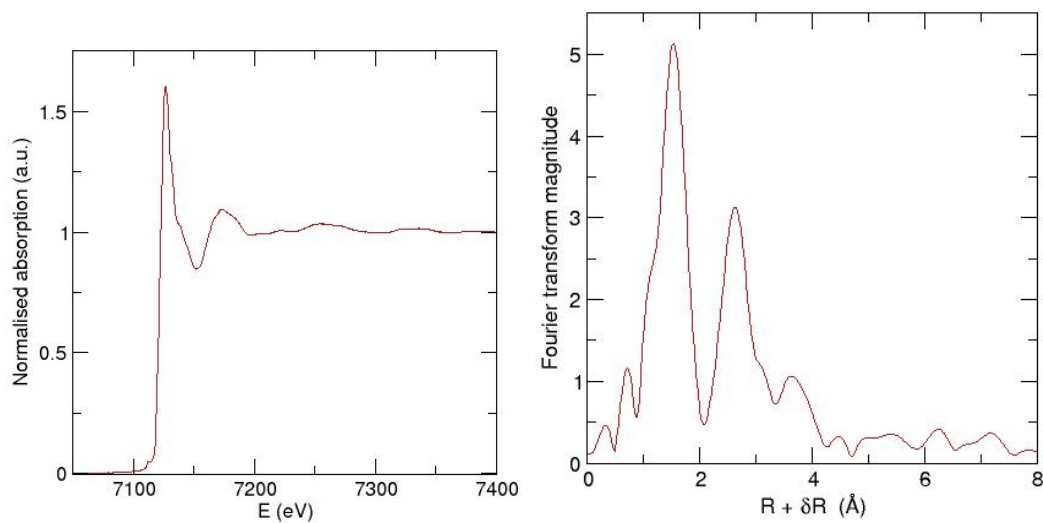


Figure 43: EXAFS and XANES data demonstrating the local structure of  $\text{LiFePO}_4$  and Fourier transform of the XANES data enabling bond lengths to be distinguished. The EXAFS and XANES spectra, (a), show that the pre-edge peak is at 7111 eV with two more peaks at 7126 and 7172 eV. The peak on the Fourier transform (b) at 1.533 Å shows Fe–O bonding and the peaks at 2.692 and 3.635 Å are associated with the higher shell bonding between the iron, phosphorus and oxygen

### 5.3 Studies of Products of Microwave synthesis of $\text{LiCoPO}_4$

$\text{LiCoPO}_4$  was synthesised through solvothermal synthesis in a microwave oven synthesiser in a similar manner to  $\text{LiFePO}_4$ , but using cobalt(II) nitrate hexahydrate as the cobalt source. The XRD pattern in Figure 44 is comparable to the database for  $\text{LiCoPO}_4$ .<sup>5</sup> The method described here is unique as there is no current literature available regarding the synthesis of  $\text{LiCoPO}_4$  solely through heating with microwaves. Current techniques involve calcination of either solid state<sup>138–144</sup> or soft–chemistry product.<sup>138,144–149</sup> These techniques involve 10 – 20 hours of calcination at temperatures of between 600 and 900°C.

Figure 45 shows the scanning electron microscopy images of  $\text{LiCoPO}_4$  and reveal a crystalline material is formed, but with a broad crystallite size distribution. Huang *et al.*,<sup>148</sup> who synthesised  $\text{LiCoPO}_4$  through solvothermal synthesis methods, obtained a crystalline structure as well, with a particle size of 1 – 6  $\mu\text{m}$ . Those orthorhombic prisms are more regular in shape, however, than the crystals formed through microwave synthesis.

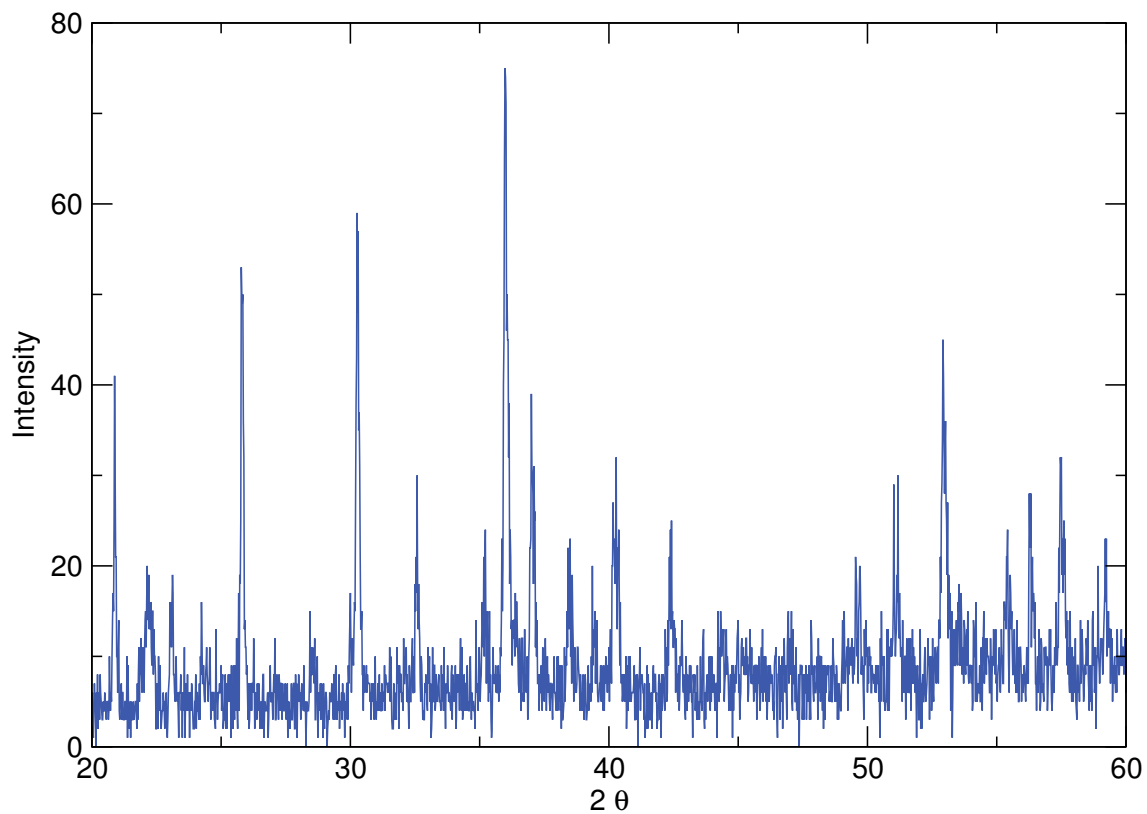


Figure 44: X-ray diffraction pattern of  $\text{LiCoPO}_4$  synthesised using  $\text{Co}(\text{NO}_3)_2 \cdot 6\text{H}_2\text{O}$  and  $\text{LiH}_2\text{PO}_4$  dispersed in ethylene glycol, and solvothermally treated in a microwave oven at  $300^\circ\text{C}$  for 2 hours. Comparison of this pattern with the reference pattern for  $\text{LiCoPO}_4$  showed a good correspondence in peak positions.<sup>5</sup>

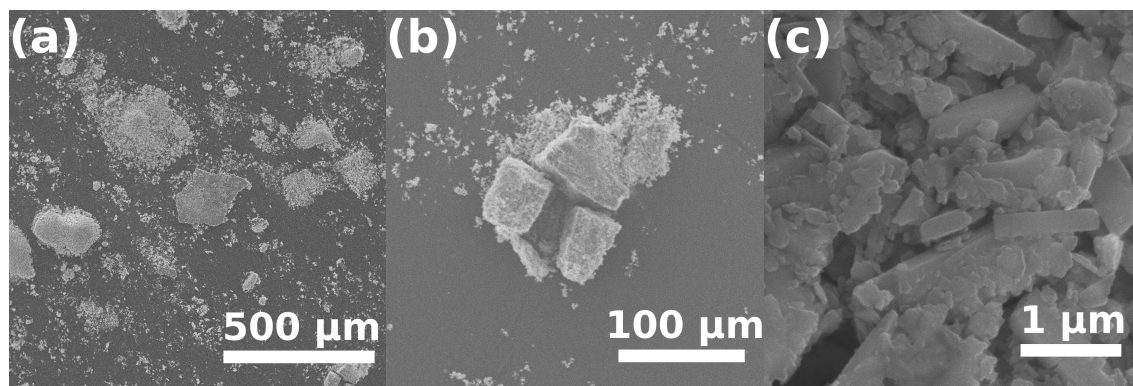


Figure 45: Scanning electron microscopy images displaying the morphology of  $\text{LiCoPO}_4$ . The images reveal that a crystalline material has been formed. There is however a broad size distribution.

The battery cycling data using  $\text{LiCoPO}_4$  can be found in Figure 46. The battery cell was formed by using the  $\text{LiCoPO}_4$  powder as the cathode, lithium foil as the anode and a Swagelok<sup>TM</sup> cell. The curve shows the uptake and discharge of lithium ions between 4.2 and 2 V. It was only cycled twice but the data show that there is a noticeable rise and fall of lithium-ion content in the structure of  $\text{LiCoPO}_4$  as the voltage is altered. This shows that it can be a viable cathode for a lithium-ion rechargeable battery. The only problem with the curve is, however, that there is no plateau occurring in the curve. This means there is no period of time within the cycle where a stable voltage is maintained while the lithium ions are leaving or entering the structure. Further cycling or alterations to the structure of  $\text{LiCoPO}_4$  through coating or doping could allow the cathode to maintain a constant voltage during charge or discharge. The reversible capacity, however, is only  $0.3 \text{ Li}^+$ .

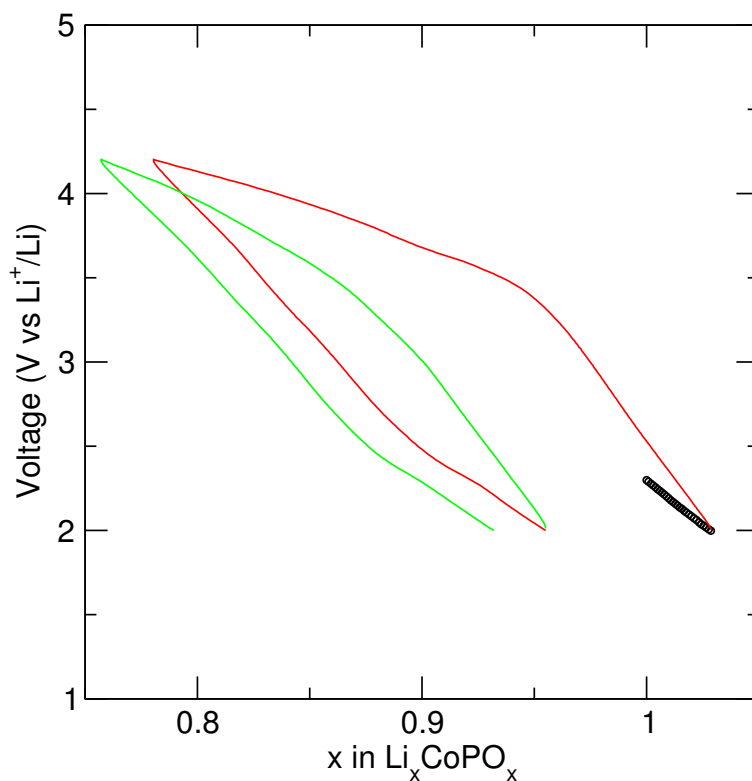


Figure 46: Cycling data for  $\text{LiCoPO}_4$  showing charge–discharge patterns between 4.2 V and 2 V. The cycle starts by discharging displayed by the black line prior to being charged. Cycling experiments were carried out by Dr S. Corr and associates in Amiens, France.

$\text{LiCoPO}_4$  was prepared for EXAFS and XANES analysis by mixing 10 mg of oxide with 140 mg of boron nitride and pressed into a pellet. The results can be found in Figure 47. The pre–edge can be found at 7710 eV, with the first peak at 7725 eV. The cobalt pre–edge and K–edge peaks according to Moen *et al.*<sup>150</sup> are at 7710 eV and 7725 eV respectively. This indicates, along with the X–ray diffraction data, that  $\text{LiCoPO}_4$  has been synthesised (or simply that Co is present).

The Fourier transform is displayed in Figure 47(c), which characterises the bond lengths present. The primary peak, located at 1.477 Å, has a similar location to that stated in the paper by Moen *et al.*<sup>150</sup> This peak displays the first shell, bonding of cobalt with oxygen. The later peaks at 2.436, 3.158 and 3.639 Å represent the bonding in the higher

shells containing the cobalt, phosphorus and oxygen.

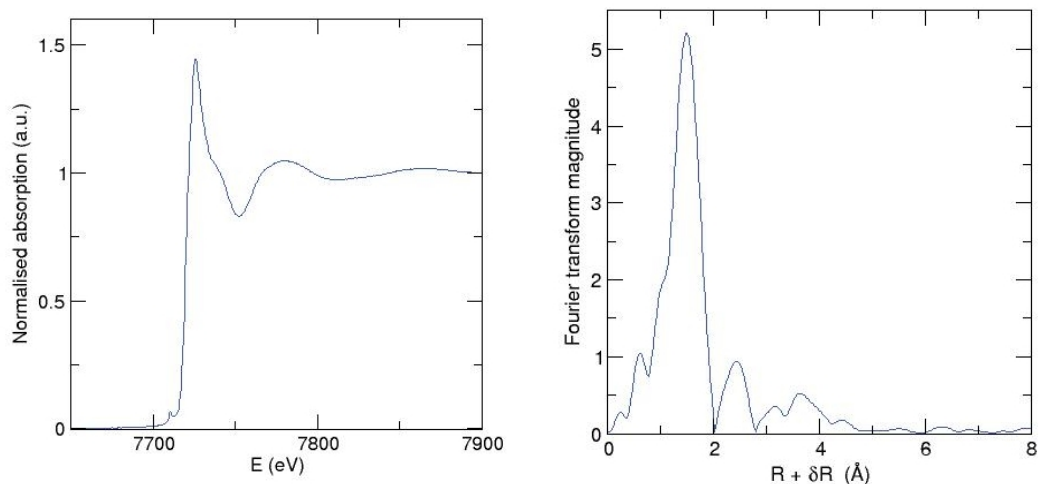


Figure 47: EXAFS and XANES data demonstrating the local structure of  $\text{LiCoPO}_4$ . Also showing the chi data and Fourier transform of the XANES data enabling bond lengths to be distinguished. On the EXAFS and XANES spectra, (a), the pre-edge can be found at 7710 eV, with the first peak at 7725 eV. (c), the Fourier transform, shows the bond lengths present. 1.477 Å shows the Co–O bonding where as 2.436 Å, 3.158 Å and 3.639 Å represent the bonding in the higher shells between the cobalt, phosphorus and oxygen.

## 5.4 Studies of Products of Microwave synthesis of $\text{LiMnPO}_4$

Samples were prepared again through microwave-assisted solvothermal synthesis. Manganese(II) acetate tetrahydrate was briefly mixed with lithium dihydrogenphosphate in ethylene glycol and then placed within a microwave oven at  $300^\circ\text{C}$  for 2 hours. Previous methods of synthesising  $\text{LiMnPO}_4$  have involved sol-gel synthesis (and subsequent calcination at  $900^\circ\text{C}$  for 10 hours),<sup>151</sup> or using solid state calcination ( $500^\circ\text{C}$  for 5 hours)<sup>152,153</sup> and a technique called ultrasonic spray pyrolysis.<sup>154–156</sup> According to Tan *et al.*, ultrasonic spray pyrolysis is preferred over solid-state calcination; it allows for slightly lower temperatures ( $400^\circ\text{C}$ ), lower reaction times (4 hours) and it is also better than soft chemistry techniques due to allowing fine control over the size and distribution of the final products.<sup>155</sup> The process, however, requires a specific and sophisticated piece of apparatus. Although microwave synthesis technique could be carried out in a domestic microwave oven,<sup>157</sup> we did not use one. It is not recommended because it is difficult to control variables such as the frequency and the wavelength of the microwaves. Because of this it is not possible to perform a controlled experiment under standard laboratory practice conditions.

The microwave synthesis technique described here produced  $\text{LiMnPO}_4$  in just 2 hours and at a temperature of  $300^\circ\text{C}$ . The product was characterised through X-ray diffraction (see Figure 48) and compared to  $\text{LiMnPO}_4$ .<sup>6</sup>

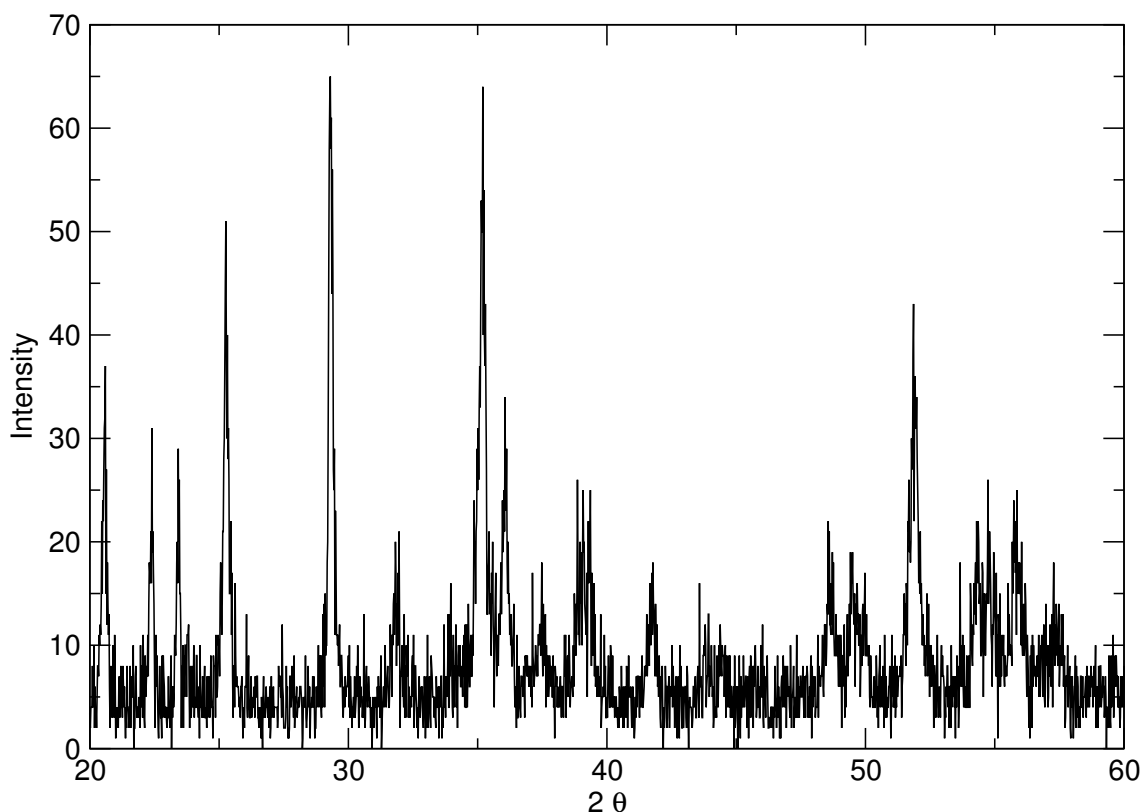


Figure 48: X-ray diffraction pattern of  $\text{LiMnPO}_4$  synthesised using  $(\text{CH}_3\text{COO})_2\text{Mn}\cdot 4\text{H}_2\text{O}$  and  $\text{LiH}_2\text{PO}_4$  dispersed in ethylene glycol, and solvothermally treated in a microwave oven at  $300^\circ\text{C}$  for 2 hours. Comparison of this pattern with the reference pattern for  $\text{LiMnPO}_4$  showed a good correspondence in peak positions.<sup>6</sup>

Upon looking at the scanning electron microscopy images of  $\text{LiMnPO}_4$ , Figure 49(a) shows that the sample has clustered into structures with poorly defined outlines. Figure 49(b) clarifies this and the appearance of a flake-like structure for the sample. It should also be noted that super-structures have been formed in the sample, with smooth edges. Figure 49(c) shows that the sample is not flake-like, but more needle-like in morphology. Other scanning electron images showed a more flake-like structure.<sup>151,152</sup> This is due to the speed of the reaction and temperatures involved as well as the starting materials. All these factors will alter the morphology of the final product. The needle-like structure

produced here does have the potential to be a good cathode due to an increased amount of needles and therefore a potentially increased surface area, allowing for more internal interaction with the  $\text{LiMnPO}_4$  cathode. The two differing structures, however, could mean that the sample contains two different phases. Further research would be to re-run the experiment to see if it is indeed two different phases and to see after what time period only one is present.

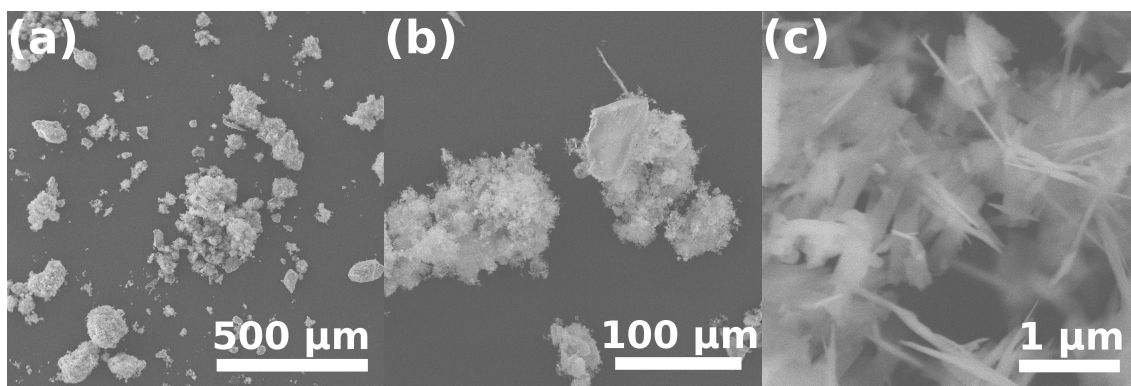


Figure 49: SEM images displaying the morphology of  $\text{LiMnPO}_4$  at varying magnifications. (a) shows that the sample is clustered into structures with a poorly defined outline. (b) gives the appearance of a flake-like structure to the sample. (c) shows that the sample is more needle-like in morphology than flake-like.

The cell for this curve was formed using the  $\text{LiMnPO}_4$  powder as the cathode and lithium foil as the anode, within a Swagelok<sup>TM</sup> cell. The charge-discharge cycle curve for  $\text{LiMnPO}_4$  (see Figure 50) shows cycling over 2–3 cycles between 4.2 and 2 V. The cycle indicates that the  $\text{LiMnPO}_4$  synthesised using microwaves is capable of accepting and releasing the lithium ions into its structure. Further testing would need to be carried out to see how many cycles the structure persists over.

However, as with the Co-containing olivine (see Figure 46), there is no plateau effect along the curve and so obtaining a stable voltage is difficult. This shows that there is no

maintaining of a constant voltage as the lithium ions pass into and out of the structure of the  $\text{LiMnPO}_4$ . Alterations to the morphology or conductivity of the material through coating, doping or changing the time or temperature of the reaction, could lead to a more beneficial charge–discharge profile. There is also a reversible capacity of only  $0.175 \text{ Li}^+$ .

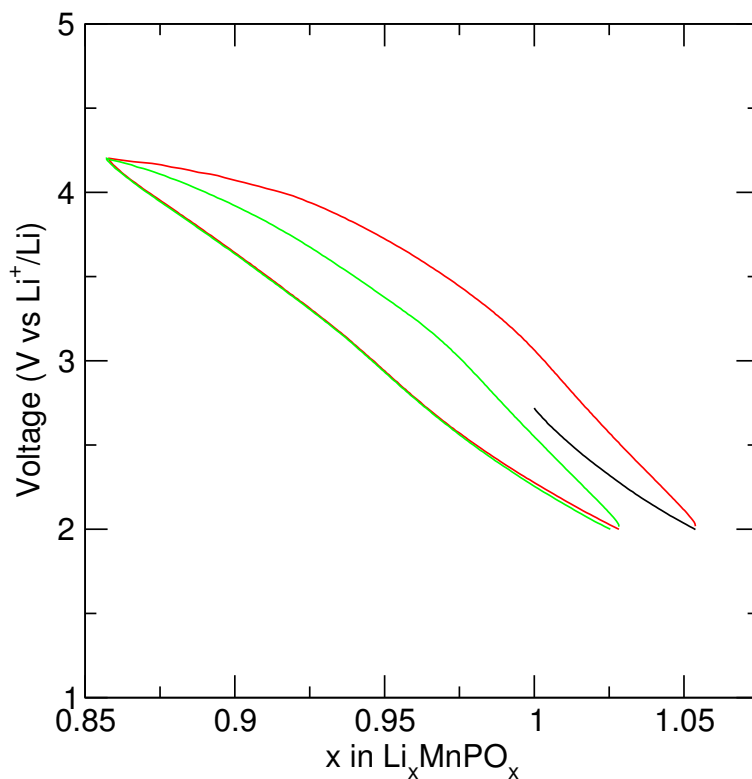


Figure 50: Cycling data for  $\text{LiMnPO}_4$  showing charge–discharge patterns between 4.2 and 2 V. Cycling experiments were carried out by Dr S. Corr and associates in Amiens, France.

$\text{LiMnPO}_4$  was prepared for EXAFS and XANES analysis by mixing 9.1 mg with 140 mg of boron nitride and pressed into a pellet. The results can be found in Figure 51. No papers were found specifically with EXAFS and XANES for  $\text{LiMnPO}_4$ . One paper, however, by

Hanson and Beeman,<sup>158</sup> used  $\text{Mn}_2\text{P}_2\text{O}_7$ . The pre-edge at 6540 eV and main peak at 6552 eV match up in both studies, as well as the slight bump of the secondary peak at 6560 eV.

The Fourier transform displays the radial distribution function. The Fourier transform is very similar to the others discussed here, with a primary peak at 1.617 Å. This shows the first shell bonding of the manganese with oxygen. The later peaks at 2.612, 3.220 and 3.705 Å represent the higher shells containing the manganese, phosphorus and oxygen.

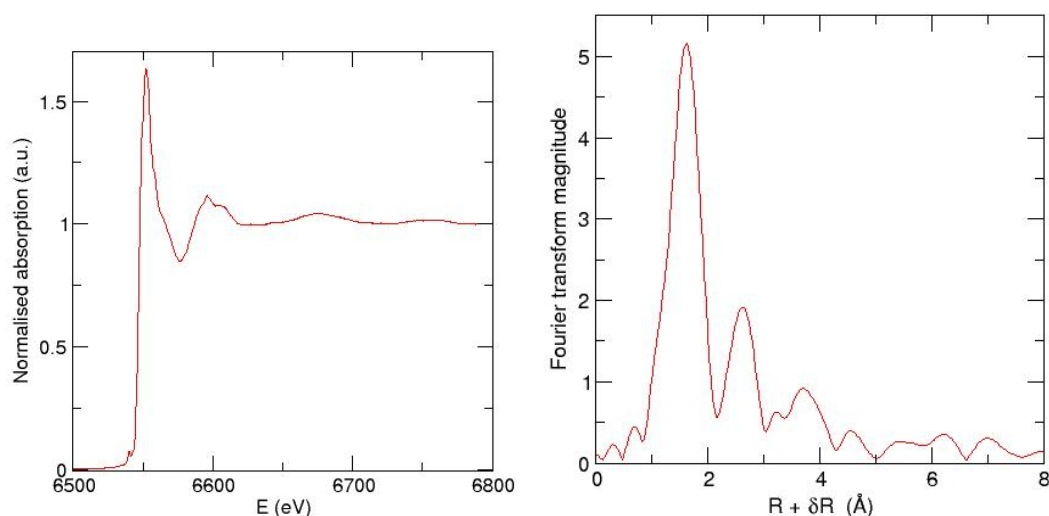


Figure 51: EXAFS and XANES data demonstrating the local structure of  $\text{LiMnPO}_4$ . Also showing the chi data and Fourier Transform of the XANES data enabling bond lengths to be distinguished. (a) shows the EXAFS and XANES data collected. The pre-edge can be found at 6540 eV with the main peak at 6552 eV and a second peak at 6560 eV. The Fourier transform is showed in (c). This shows the bonding within the  $\text{LiMnPO}_4$ . The peaks shown are at 1.617 Å, the Mn – O bond, and 2.612 Å, 3.220 Å and 3.705 Å represent the bonding in the higher shells between the manganese, phosphorus and oxygen.

## 5.5 Conclusions and Future Work

This microwave synthesis is a much more rapid reaction than traditional solid state or hydrothermal routes.<sup>159–162</sup> For example, Yang *et al.* report a Parr bomb synthesis which took 5 hours,<sup>163</sup> in contrast to 2 hours in this work using microwaves. Previously reported microwave-assisted methods have also had shorter synthesis times, highlighting the effectiveness of this method.<sup>129–132</sup> Some of these methods take only a few minutes.<sup>130,131</sup> Hence, there is great scope for further development of that synthesis strategy.

Overall, the methods described in this chapter for producing olivine phosphate structures look promising. The X-ray diffraction patterns and Fourier transformed EXAFS data shows that the reactions have reached completion and that the intended lithium metal phosphates have been successfully synthesised.

The reaction times and temperatures used are lower than previous techniques available. The cycling data show that, for the use of manganese and cobalt olivine phosphates, cathodes can hold and release the lithium ions and maintain a steady cycle curve for a few runs. Future studies need to be carried out to see how they fare with prolonged cycling. The iron phosphate olivine structure looks even better, with the fact that it plateaus and allows a steady release of lithium ions whilst maintaining a constant voltage. Again, longer cycling with possibly coating and or doping could ascertain if this method will synthesise cathode materials.

All the scanning electron microscopy images show that flakes and/or needles have been formed. Either would be a good quality for a lithium-ion battery cathode to possess, due to the increased surface area available for the interaction with the electrolyte. This would then allow more interaction with the cathode, increasing its capacity. Further research into different reaction times and temperatures, as well as coating and doping may change the morphology.

## 6 Conclusions and Future Work

With levels of research and interest rising in renewable energies, lithium-ion battery capabilities have been highlighted and accepted for their potential uses in electric vehicle technologies and also possibility for energy storage. This thesis outlines various new synthesis techniques and results for  $\text{VO}_2(\text{B})$ , an exciting and potentially new lithium-ion battery cathode material. Work was also carried out into reducing the reaction times for synthesis of common olivine phosphate structures through the use of microwave synthesis. Current techniques rely upon long duration synthetic methods, via solid state and soft chemical synthesis. Through use of a microwave oven reactor for the synthesis process, reaction times have been decreased.

### 6.1 Summary

The first chapter of the thesis began with a brief history behind rechargeable batteries and how they charge and discharge during use. An account was also given about current lithium-ion battery technology, in which  $\text{LiCoO}_2$  is primarily used. Olivine phosphate structures are a promising class for the future, and an in-depth analysis is given for these along with vanadium dioxide, focusing upon its bronze(B) phase, which is the main focus of this thesis. Three different synthetic techniques were also outlined, with two of them (solvothermal and microwave-assisted solvothermal synthesis) used throughout the thesis. Chapter 1 then concluded with a brief look at the other components within a lithium-ion battery and also the aims and objectives of this thesis.

Chapter 2 outlined the background behind the different characterisation techniques used and also an in-depth look at how the samples were prepared via solvothermal and microwave-assisted solvothermal synthesis.

Chapter 3 outlines  $\text{VO}_2(\text{B})$  as a potential lithium-ion battery cathode material. Samples were synthesised through both solvothermal and microwave-assisted solvothermal

synthesis and then characterised using XRD, SEM and XAS. A range of samples were synthesised, with alterations to the temperature and time (to optimise both solvothermal and microwave synthesis methods). Further research could see if the reaction times can be further reduced.

Some samples were also used in charge–discharge studies in Chapter 4. One VO<sub>2</sub>(B) sample cell should be noted as having been charged and discharged *in situ* within the B18 beamline and its evolution characterised through XAS. This allowed the near neighbour structural changes to be observed and recorded during cycling.

Olivine phosphate structures containing iron, manganese or cobalt were also prepared through microwave synthesis and are discussed in Chapter 5. Again, the samples were characterised through the use of XRD, SEM, XAS and charge–discharge cycling. A two hours duration technique for synthesising LiFePO<sub>4</sub> appears the most promising due to having a redox potential plateau at 3.4 V and steep slopes either side during charging and discharging.

## 6.2 Conclusions

The main aim of this thesis was to find a new route to synthesise vanadium oxides through the use of microwave–assisted synthesis, lowering the preparation time while maintaining the purity and phase of the product. Faster synthesis times allow more reactions to be carried out over a set period. These reactions could include alterations to the time, temperature, or starting solvent, or coating or doping of the sample. Shortening reaction times allows the process of optimisation to be reached sooner. As mentioned in Chapter 3, current literature synthesis methods for VO<sub>2</sub>(B) take 48 hours within a solvothermal bomb. By reducing the reaction time to 24 hours, the same results were achieved by this method.

Microwave synthesis was then used to reduce the time further. On comparison of microwave runs of differing time, it was found that a 6 hour method formed VO<sub>2</sub>(B)

(characterised through XRD and SEM). Altering the temperatures for a 1 hour period suggested that temperature can also affect reaction rate; it can be hypothesised that the reaction could be optimised further through higher temperatures and / or different solvents to aid the reduction of the synthesis / reaction time, although subsequent research would be required to confirm this.

The 48 hour solvothermal PTFE lined Parr bomb synthesis product was characterised before being cycled. The results showed that  $\text{VO}_2(\text{B})$  can make an effective cathode, but that further testing would need to be carried out to see if it can withstand extended cycling ( $\approx$  20 cycles). The cathode, having been placed within a battery cell, was then cycled *in situ* in the beamline of a synchrotron to enable XAS to be obtained during cycling. This enabled the identification of the structural changes occurring during a discharge/charge cycle. It was shown that the V in the  $\text{VO}_2(\text{B})$  cathode changes from a  $\text{V}^{4+}$  oxidation state to a  $\text{V}^{3+}$  oxidation state during the gain of lithium ions and electrons. It was also confirmed that  $\text{VO}_2(\text{B})$  has alternating V–V separations due to the dual  $\text{V}^{4+} - \text{V}^{4+}$  peaks seen on the Fourier transform gained from the EXAFS data.

Finally, olivine phosphate structures were also produced through the use of microwave-assisted synthesis. Iron, manganese or cobalt lithium phosphates were all synthesised over 2 hours. Research has shown that lithium iron phosphate can be synthesised in 5 minutes, and so it is possible that through improvements to the synthetic process the reaction time could be reduced this dramatically. The cycling data for the lithium iron phosphate product were encouraging, showing that it could be used in a lithium-ion battery cathode. However, further cycling studies would be needed to test this.

This is the first report that lithium cobalt phosphate can be successfully synthesised in a microwave oven. This material was characterised through XRD, SEM and XAS and again has the potential to be further optimised. Lithium manganese phosphate was also synthesised in a microwave oven and characterised. Both manganese and cobalt containing materials were tested to see if usable cycling would occur and was successful for both samples. However, no plateau in cell voltage occurred. Further research would

be required to optimise the reaction time and to improve the electrochemical properties of these two cathode materials, so as to not breakdown as easily from intercalation, to hold more  $\text{Li}^+$  and to allow for a steady release of these ions.

Overall the data gained from this thesis can hopefully aid in the faster production of lithium-ion battery cathodes. The reaction times of 4 samples through 5 reactions were reduced, increasing the speed at which optimisation of the electrochemical properties of the cathodes can be carried out, and later on, manufactured.

### 6.3 Future Work

This thesis explored altering the solvent reductant and starting vanadate to try to influence the final morphology and to reduce the overall reaction time. The results of these can be found in the future work in Chapter 3. The starting vanadate was changed to ammonium metavanadate, with the solvent staying as formaldehyde. Through the use of solvothermal synthesis, the reaction times were differed. However, after characterisation of the products, it was found that  $\text{VO}_2(\text{B})$  had not been formed. Further research would need to be carried out to see if a different solvent or higher temperatures can bring about the synthesis of  $\text{VO}_2(\text{B})$ .

The 6 hour method of synthesising  $\text{VO}_2(\text{B})$  within a microwave oven could also be further optimised to possibly further reduce the reaction time, or to coat or dope the sample to aid electrical conductivity. Also cycling could enable analysis as to whether the new morphology affects the cycling capabilities in a positive way.

If the cycling does prove that the material can be used in a cathode, then *in situ* EXAFS is also a possibility, to see if the same reaction mechanism is occurring as with the  $\text{VO}_2(\text{B})$ .

Turning to the olivine phosphate materials that have been synthesised in this paper, further optimisation could be carried out to reduce the reaction times. Alteration of the

starting reactants or solvent could aid in this, as higher boiling points could result in achieving higher temperatures and possibly making the reaction more rapid. It would also be interesting to cycle  $\text{LiFePO}_4$  more to see how long the structure maintained itself. Cycling whilst gaining EXAFS data would also be interesting and give us information on the changing structure throughout the discharging process.

$\text{LiMnPO}_4$  and  $\text{LiCoPO}_4$  need further optimisation and stability as the cycle curves, although showing lithium-ion uptake and release, do not have an optimal plateau which would show an even voltage being maintained whilst lithium ions enter and leave the structure. Possible alterations to the starting materials, or approaches such as coating the cathode in carbon or adding a dopant may enable the cathode to perform better.

## References

- [1] Oka, Y.; Yao, T.; Yamamoto, N.; Ueda, Y.; Hayashi, A. *J. Solid State Chem.* **1993**, *105*, 271–278.
- [2] *Diamond Light Source*, <http://diamond.ac.uk/Home/Media/images.html>, Accessed: 1/10/2011.
- [3] Amatucci, G. G.; Badway, F.; Pasquier, A. D.; Zheng, T. *J. Electrochem. Soc.* **2001**, *148*, A930–A939.
- [4] Sanchez, M.; Brito, G.; Fantini, M.; Goya, G.; Matos, J. *Solid State Ionics* **2006**, *177*, 497–500.
- [5] Kubel, F. *Z. Kristallogr.* **1994**, *209*, 755–755.
- [6] Geller, S.; Durand, J. *Acta Crystallogr.* **1960**, *13*, 325–331.
- [7] Baker, J. *Energy Policy* **2008**, *36*, 4368–4373.
- [8] Tarascon, J.-M.; Armand, M. *Nature* **2001**, *414*, 359–367.
- [9] Burke, A.; Miller, M. *Electrochim. Acta* **2010**, *55/25*, 7538–7548.
- [10] Planté, G. *C. R. Acad. Sci.* **1860**, *50*, 640–642.
- [11] Kurzweil, P. *J. Power Sourc.* **2010**, *195*, 4424–4434.
- [12] Beck, F.; Rüetschi, P. *Electrochim. Acta* **2000**, *45*, 2467–2482.
- [13] Vucht, J. V.; Kuijpers, F.; Bruning, H. *Philips Res. Rep.* **1970**, *25*, 133–140.
- [14] Cuevas, F.; Joubert, J.-M.; Latroche, M.; Percheron-Guégan, A. *Appl. Phys. A* **2001**, *72*, 225–238.
- [15] Croce, F.; Appetecchi, G.; Persi, L.; Scrosati, B. *Nature* **1998**, *394*, 456–458.

- [16] Reddy, C. S.; Jr., E. H. W.; Sr., S. W.; Williams, Q. L.; Kalluru, R. R. *Curr. Appl Phys.* **2009**, *9*, 1195–1198.
- [17] Amatucci, G.; Tarascon, J.; Klein, L. *J. Electrochem. Soc.* **1996**, *143*, 1114–1123.
- [18] Shukla, A.; Kumar, T. P. *Current Science* **2008**, *94/3*, 314–331.
- [19] Young, H. D.; Freedman, R. A. *University Physics*; Pearson Education: San Francisco, **1996**, Ch: 21–32.
- [20] Conte, M.; Prosini, P.; Passerini, S. *Mater. Sci. Eng., B* **2004**, *108*, 2–8.
- [21] Gies, A.; Pecquenard, B.; Benayad, A.; Martinez, H.; Gonbeau, D.; Fuess, H.; Levasseur, A. *Thin Solid Films* **2008**, *516*, 7271–7281.
- [22] Ding, N.; Feng, X.; Liu, S.; Xu, J.; Fang, X.; Lieberwirth, I.; Chen, C. *Electrochem. Commun.* **2009**, *11*, 538–541.
- [23] Bazito, F. F. C.; Torresi, R. M. *J. Braz. Chem. Soc.* **2006**, *17*, 627–642.
- [24] Kannan, A.; Manthiram, A. *Solid State Ionics* **2003**, *159*, 265–271.
- [25] et al, D. *J. Electrochem. Soc.* **1991**, *138/8*, 2207–2211.
- [26] Rao, C. N. R. *J. Mater. Chem.* **1999**, *9*, 1–14.
- [27] Kanatzidis, M. G.; Poeppelmeier, K. R. *Prog. Solid State Chem.* **2008**, *36*, 1–133.
- [28] Recham, N.; Armand, M.; Tarascon, J.-M. *C.R. Chim.* **2010**, *13*, 106–116.
- [29] Smart, L.; Moore, E. *Solid State Chemistry: An introduction; 2nd Edition*; Nelson Thornes: Cheltenham, **1996**; pp 79–111.
- [30] Murugan, A. V.; Muraliganth, T.; Manthiram, A. *J. Phys. Chem. C* **2008**, *112*, 14665–14671.
- [31] Mizushima, K.; Jones, P. C.; Wiscman, P. J.; Goodenough, J. B. *Mater. Res. Bull.* **1980**, *15*, 783–789.

- [32] Ohzuku, T.; Ueda, A. *Solid State Ionics* **1994**, *69*, 201–211.
- [33] Orman, H. J.; Wiseman, P. J. *Acta Cryst.* **1984**, *40*, 12–14.
- [34] Xia, H.; Lu, L.; Ceder, G. *J. Power Sources* **2006**, *159*, 1422–1427.
- [35] Bates, J. B.; Dudney, N. J.; Neudecker, B. J.; Hart, F. X.; Jun, H. P.; Hackney, S. A. *J. Electrochem. Soc.* **2000**, *147*, 59–70.
- [36] Lee, J.; Lee, S.; Baik, H.; Lee, H.; Jang, S.; Lee, S. *Electrochem. Solid-State Lett.* **1999**, *2*, 512–515.
- [37] da Fonseca, C. P.; Davalos, J.; Kleinke, M.; Fantini, M.; Gorenstein, A. *J. Power Sources* **1999**, *81–82*, 575–580.
- [38] Liao, C.; Fung, K. *J. Power Sources* **2004**, *128*, 263–269.
- [39] Xia, H.; Lu, L.; Ceder, G. *J. Alloys Compd.* **2006**, *417*, 304–310.
- [40] Kim, K.; Woo, S.; Choi, K.; Han, K.; Park, Y. *Solid State Ionics* **2003**, *159*, 25–34.
- [41] Lee, S.; Lee, J.; Kim, D.; Baik, H. *J. Electrochem. Soc.* **1996**, *143*, 268–270.
- [42] Yoon, W. S.; Ban, S. H.; Lee, K. K.; Kim, K. B.; Kim, M. G.; Lee, J. M. *J. Power Sources* **2001**, *97–98*, 282–286.
- [43] Maranchi, J. P.; Hepp, A. F.; Kumta, P. N. *Mater. Sci and Eng. B* **2005**, *116*, 327–340.
- [44] Saidi, M.; Barker, J.; Huang, H.; Swoyer, J.; Adamson, G. *J. Power Sources* **2003**, *119–121*, 266–272.
- [45] Li, Y.; Zhou, Z.; Gao, X.; Yan, J. *J. Power Sources* **2006**, *160*, 633–637.
- [46] Guo, Y.-G.; Hu, Y.-S.; Sigle, W.; Maier, J. *Adv. Mater.* **2007**, *19*, 2087–2091.

- [47] Chen, W.; Peng, J.; Mai, L.; Yu, H.; Qi, Y. *Chem. Lett.* **2004**, *33*, 1366–1367.
- [48] Manthiram, A.; Murugan, A. V.; Sarkar, A.; Muraliganth, T. *Energy Environ. Sci.* **2008**, *1*, 621–638.
- [49] Wang, Y.; Yang, Y.; Yang, X. H. Y.; Shao, H. *J. Alloys Compd.* **2009**, *481*, 590–594.
- [50] Lee, S.-W.; Jung, B.-Y.; Han, K.-S.; Lee, Y.; Kim, D.; Kim, M.-G.; Ryu, K. S.; Kang, E.-Y.; Jeong, J.-H. *Electrochim. Acta* **2004**, *50*, 479–483.
- [51] Armstrong, A. R.; Robertson, A. D.; Gitzendanner, R.; Bruce, P. G. *J. Solid State Chem.* **1999**, *145*, 549–556.
- [52] Penazzi, N.; Arrabito, M.; Piana, M.; Bodoardo, S.; Panero, S.; Amadei, I. *J. Eur. Ceram. Soc.* **2004**, *24*, 1381–1384.
- [53] Kuang, Q.; Zhao, Y.; An, X.; Liu, J.; Dong, Y.; Chen, L. *Electrochim. Acta* **2010**, *55*, 1575–1581.
- [54] Ren, M.; Zhou, Z.; Su, L.; Gao, X. *J. Power Sources* **2009**, *189*, 786–789.
- [55] Wu, C.; Wei, H.; Ning, B.; Xie, Y. *Adv. Mater.* **2010**, *22*, 1972–1976.
- [56] Pavasupree, S.; Suzuki, Y.; Kitiyanan, A.; Pivsa-Art, S.; Yoshikawa, S. *J. Solid State Chem.* **2005**, *178*, 2152–2158.
- [57] Zhou, F.; Zhao, X.; Xu, H.; Yuan, C. *Chem. Lett.* **2006**, *35*, 1280–1281.
- [58] Guiton, B. S.; Gu, Q.; Prieto, A. L.; Gudiksen, M. S.; Park, H. *J. Am. Chem. Soc.* **2005**, *127*, 498–499.
- [59] Kim, H.-T.; Chae, B.-G.; Youn, D.-H.; Maeng, S.-L.; Kim, G.; Kang, K.-Y.; Lim, Y.-S. *New J. Phys.* **2004**, *6*, 52–19.
- [60] Ichikawa, S.; Hibino, M.; Yao, T. *Asian J. Energy Environ.* **2007**, *8*, 33–47.

- [61] Whittingham, M. S. *Progressive Solid State Chem.* **1978**, *12*, 41–99.
- [62] Chung, S.; Chmilenko, N.; Borovykov, A.; Leeal, S. *J. Power Sources* **1999**, *84*, 6–11.
- [63] Huynh, W. U.; Dittmer, J. J.; Alivisatos, A. P. *Science* **2002**, *295*, 2425–2427.
- [64] Kam, K. C.; Cheetham, A. K. *Mater. Res. Bull.* **2006**, *41*, 1015–1021.
- [65] Lee, J.-W.; Park, S.-M.; Kim, H.-J. *J. Power Sources* **2009**, *188*, 583–587.
- [66] Chen, Z.; Qin, Y.; Amine, K.; Sun, Y.-K. *J. Mater. Chem.* **2010**, *20*, 7606–7612.
- [67] Jiang, T.; Du, F.; Zhang, K.; Wei, Y.; Li, Z.; Wang, C.; Chen, G. *Solid State Sci.* **2010**, *12*, 1672–1676.
- [68] Balbuena, *Lithium-ion batteries: Solid-Electrolyte Interphase*; Imperial College Press: London, **2004**, Ch: 2, 3, 8.
- [69] Xu, K.; von Cresce, A. *J. Mater. Chem.* **2011**, *21*, 9849–9864.
- [70] Stanton, A. *Nature* **1896**, *53*, 274–276.
- [71] *Nobel Prize website, Rontgen*, [http://www.nobelprize.org/nobel\\_prizes/physics/laureates/1901/rontgen-bio.html](http://www.nobelprize.org/nobel_prizes/physics/laureates/1901/rontgen-bio.html), Accessed: 1/10/2011.
- [72] *Nobel Prize website, Max von Laue*, [http://www.nobelprize.org/nobel\\_prizes/physics/laureates/1914/laue-bio.html](http://www.nobelprize.org/nobel_prizes/physics/laureates/1914/laue-bio.html), Accessed: 1/10/2011.
- [73] Nuffield, E. W. *X-ray Diffraction Methods*; John Wiley and Sons, Inc.: New York, **1966**, Ch: 1–2.
- [74] West, A. R. *Basic Solid State Chemistry: Second Edition*; Wiley: Chichester, **1999**, Ch: 1, 4.
- [75] Chang, R. *Physical Chemistry for the Chemical and Biological Sciences*; University Science Books: Sausalito, **2000**, Ch: 2–3.

- [76] Atkins, P.; de Paula, J. *Atkins' Physical Chemistry*; Oxford University Press: Oxford, **2010**, Ch: 2–4.
- [77] Warren, B. E. *X-ray Diffraction*; Dover Publications, inc.: New York, **1990**, Ch: 2–3.
- [78] Margaritondo, G. *Introduction to Synchrotron Radiation*; Oxford University Press: Oxford, **1988**, Ch: 1–2.
- [79] Greaves, G. N.; Munro, I. H. *Synchrotron Radiation Sources and their Applications*; SUSSP Publications: Edinburgh, **1985**, Ch: 1–2.
- [80] Catlow, C. R. A.; Greaves, G. N. *Applications of Synchrotron Radiation*; Blackie and Son Ltd: London, **1990**, Ch: 1–2.
- [81] Winick, H.; Doniach, S. *Synchrotron Radiation Research*; Plenum Press: New York, **1980**, Ch: 2–3.
- [82] Elder, F. R.; Gurewitsch, A. M.; Langmuir, R. V.; Pollock, H. C. *Phys. Rev* **1947**, *71*, 829–830.
- [83] Liénard, A. *L'Eclairage Elec.* **1898**, *16*, 5–14.
- [84] Schott, G. A. *Ann. Phys.* **1907**, *24*, 635–660.
- [85] Jassinsky, W. W. *J. Exp. Theor. Phys.* **1935**, *5*, 983–983.
- [86] Kerst, D. *Phys. Rev.* **1941**, *60*, 47–53.
- [87] Ivanenko, D.; Pomeranchuk, I. *Phys. Rev.* **1944**, *65*, 343–343.
- [88] Arzimovich, L.; Pomeranchuk, I. *J. Phys.* **1945**, *9*, 267–276.
- [89] Blewett, J. P. *Phys. Rev.* **1946**, *69*, 87–95.
- [90] Sokolov, A. A.; Ivanenko, D. *Dokl. Akad. Nauk* **1948**, *59*, 1551–1554.

- [91] Schwinger, J. *Phys. Rev.* **1949**, 75, 1912–1925.
- [92] Elder, F. R.; Gurewitsch, A. M.; Langmuir, R. V.; Pollack, H. D. *Phys. Rev.* **1947**, 71, 829–830.
- [93] Korolev, F. A.; Markov, V. S.; Akimov, E. M.; Kulikov, O. F. *Sov. Phys. Dokl.* **1956**, 1, 568–568.
- [94] Bathov, G.; Freytag, E.; Hansel, R. *J. Appl. Phys.* **1966**, 37, 3449–3449.
- [95] Dagneaux, P.; Depautex, C.; Dhez, P.; Durup, J.; Farge, Y.; Fourme, R.; Guyon, P. M.; Jaeglé, P.; Leach, S.; Lopez-Delgado, R.; Morel, G.; Pinachaux, R.; Thiry, P.; Vermeil, C.; Wuilleumer, F. *Ann. Phys.* **1975**, 9, 9–65.
- [96] Rowe, E. M.; Mills, F. E. *Part. Accel.* **1973**, 4, 211–227.
- [97] Brown, F. C.; Bachrach, R. Z.; Lien, N. *Nucl. Instrum. Methods* **1978**, 152, 73–80.
- [98] Kallne, E.; Schnopper, H. W.; Delvaille, J. P.; Speybroeck, L. P. V.; Bachrach, R. Z. *Nucl. Instrum. Methods* **1978**, 152, 101–107.
- [99] Davidson, M. W.; Abramowitz, M. *Optical Microscopy: Encyclopedia of Imaging Science and Technology*; John Wiley and Sons, Inc.: New York, **2002**; pp 1106–1141.
- [100] Knoll, M. *Zeitschrift für technische Physik* **1935**, 16, 467–475.
- [101] von Ardenne, M. *Zeitschrift für technische Physik* **1939**, 108, 553–572.
- [102] von Ardenne, M. *Zeitschrift für technische Physik* **1938**, 19, 407–416.
- [103] Everhart, T. E. *J. Vac. Sci. Technol, B* **1996**, 14, 3620–3624.
- [104] Oatley, C. W. *J. Appl. Phys.* **1982**, 53, R1–R13.

- [105] Corr, S. A.; Grossman, M.; Shi, Y.; Heier, K. R.; Stucky, G. D.; Seshadri, R. *J. Mater. Chem.* **2009**, *19*, 4362–4267.
- [106] Tian, J.; Liu, F.; Shen, C.; Zhang, H.; Yang, T.; Bao, L.; Wang, X.; Liu, D.; Li, H.; Huang, X.; Li, J.; Chen, L.; Gao, H. *J. Mater. Res.* **2007**, *22*, 1921–1926.
- [107] Nia, J.; Jianga, W.; Yua, K.; Gaob, Y.; Zhua, Z. *Electrochim. Acta* **2011**, *56*, 2122–2126.
- [108] Baudrin, E.; Sudant, G.; Larcher, D.; Dunn, B.; Tarascon, J.-M. *Chem. Mater.* **2006**, *18*, 4369–4374.
- [109] Lutterotti, L.; Voltolini, M.; Wenk, H.-R.; Bandyopadhyay, K.; Vanorio, T. *American Mineralogist* **2010**, *95*, 98–103.
- [110] Corr, S.; Grossman, M.; Furman, J.; Melot, B.; Cheetham, A.; Heier, K.; Seshadri, R. *Chem. Mater.* **2008**, *20*, 6396–6404.
- [111] Zhang, K.-F.; Bao, S.-J.; Liu, X.; Shi, J.; Su, Z.-X.; Li, H.-L. *Mater. Res. Bull.* **2006**, *41*, 1985–1989.
- [112] Chen, W.; Peng, J.; Mai, L.; Yu, H.; Qi, Y. *Solid State Commun.* **2004**, *132*, 513–516.
- [113] Yin, H.; Yu, K.; Zhang, Z.; Zhu, Z. *Appl. Surf. Sci.* **2011**, *257*, 8840–8845.
- [114] Qiao, Y. L.; Ma, Y. J.; Luo, Q. P.; Pei, C. H. *Mater. Sci. Forum* **2011**, *694*, 91–99.
- [115] Deb, A.; Bergmann, U.; Cairns, E. J.; Cramer, S. P. *J. Synchrotron Rad.* **2004**, *11*, 497–504.
- [116] Leriche, J. B.; Hamelet, S.; Shu, J.; Morcrette, M.; Masquelier, C.; Ouvrard, G.; Zerrouki, M.; Soudan, P.; Belin, S.; Elkaim, E.; Baudalet, F. *J. Electrochem. Soc.* **2010**, *157*, A606–A610.

- [117] Murphy, D. W.; Christian, P. A.; DiSalvo, F. J.; Carides, J. N.; Waszczak, J. V. *J. Electrochem. Soc.* **1981**, *128*, 2053–2060.
- [118] Murphy, D. W.; Christian, P. A. *Science* **1979**, *205*, 651–656.
- [119] Wong, J.; Lytle, F. W.; Messmer, R. P.; Maylotte, D. H. *Phys. Rev. B* **1984**, *30*, 5596–5610.
- [120] Andersson, G. *Acta Chem. Scand.* **1956**, *10*, 623–628.
- [121] Yu Kang, F.; Ma, J.; Hua Li, B. *New Carbon Mater.* **2011**, *26*, 161–170.
- [122] Padhi, A. K.; Nanjundaswamy, K. S.; Goodenough, J. B. *J. Electrochem. Soc.* **1997**, *144*, 1188–1194.
- [123] Jugović, D.; Uskoković, D. *J. Power Sources* **2009**, *190*, 538–544.
- [124] Wang, D.; Wu, X.; Wang, Z.; Chen, L. *J. Power Sources* **2005**, *140*, 125–128.
- [125] Takahashi, M.; Tobishima, S.; Takei, K.; Sakurai, Y. *J. Power Sources* **2001**, *97–98*, 508–511.
- [126] Yang, S.; Zavalij, P. Y.; Whittingham, M. S. *Electrochem. Commun.* **2001**, *3*, 505–508.
- [127] Shiraishi, K.; Dokko, K.; Kanamura, K. *J. Power Sources* **2005**, *146*, 555–558.
- [128] Chen, J.; Whittingham, M. S. *Electrochem. Commun.* **2006**, *8*, 855–858.
- [129] Ji, H.; Yang, G.; Miao, X.; Hong, A. *Electrochim. Acta* **2010**, *55*, 3392–3397.
- [130] Ji, H.; Yang, G.; Ni, H.; Roy, S.; ao Pinto, J.; Jiang, X. *Electrochim. Acta* **2011**, *56*, 3093–3100.
- [131] Murugan, A. V.; Muraliganth, T.; Manthiram, A. *Electrochem. Commun.* **2008**, *10*, 903–906.

- [132] Zhang, Y.; Feng, H.; Wu, X.; Wang, L.; Zhang, A.; Xia, T.; Dong, H.; Liu, M. *Electrochim. Acta* **2009**, *54*, 3206–3210.
- [133] Bauer, E. M.; Bellitto, C.; Righini, G.; Pasquali, M.; DellEra, A.; Prosini, P. P. *J. Power Sources* **2005**, *146*, 544–549.
- [134] Shin, H. C.; Cho, W. I.; Jang, H. *J. Power Sources* **2006**, *159*, 1383–1388.
- [135] Lu, Z.; Chen, H.; Robert, R.; Zhu, B.; Deng, J.; Wu, L.; Chung, C.; Grey, C. *Chem. Mat.* **2011**, *23*, 2848–2859.
- [136] Ellis, B.; Kan, W. H.; Makahnouk, W. R. M.; Nazar, L. F. *J. Mater. Chem.* **2007**, *17*, 3248–3254.
- [137] Zhao, T.; Chu, W.; Zhao, H.; Liana, X.; Xu, W.; Yu, M.; Xia, D.; Wu, Z. *Nucl. Instrum. Methods Phys. Res., Sect. A* **2010**, *619*, 122–127.
- [138] Tan, L.; Luo, Z.; Liu, H.; Yu, Y. *J. Alloys Compd.* **2010**, *502*, 407–410.
- [139] Rabanal, M.; Gutierrez, M.; Garcia-Alvarado, F.; Gonzalo, E.; de Dompablo, M. A. *J. Power Sources* **2006**, *160*, 523–528.
- [140] Jang, I. C.; Son, C. G.; Yang, S. M. G.; Lee, J. W.; Cho, A. R.; Aravindan, V.; Park, G. J.; Kang, K. S.; Kim, W. S.; Cho, W. I.; Lee, Y. S. *J. Mater. Chem.* **2011**, *21*, 6510–6514.
- [141] Amine, K.; Yasuda, H.; Yamachi, M. *Electrochem. Solid State Lett.* **2000**, *3*, 178–179.
- [142] Loris, J. M.; Vicente, C. P.; Tirado, J. L. *Electrochem. Solid State Lett.* **2002**, *5*, 234–237.
- [143] Jin, B.; Gu, H.-B.; Kim, K.-W. *J. Solid State Electrochem.* **2008**, *12*, 105–111.
- [144] Violeta, K.; Ekaterina, Z.; Radostina, S. *Eur. J. Inorg. Chem.* **2010**, *26*, 4091–4099.

- [145] Bramnik, N. N.; Nikolowski, K.; Trots, D. M.; Ehrenberg, H. *Electrochem. Solid State Lett.* **2008**, *11*, 89–93.
- [146] Gangulibabu,.; Bhuvaneswari, D.; Kalaiselvi, N.; Jayaprakash, N.; Periasamy, P. *J. Sol–Gel Sci. Technol.* **2009**, *49*, 137–144.
- [147] Deniard, P.; Dulac, A. M.; Rocquefelte, X.; Grigorova, V.; Lebacqz, O.; Pasturel, A.; Jobic, S. *J. Phys. Chem. Solids* **2004**, *65*, 229–233.
- [148] Huang, X.; Ma, J.; Wu, P.; Hu, Y.; Dai, J.; Zhu, Z.; Chen, H.; Wang, H. *Mater. Lett.* **2005**, *59*, 578–582.
- [149] Li, H. H.; Jin, J.; Wei, J. P.; Zhou, Z.; Yan, J. *Electrochem. Commun.* **2009**, *11*, 95–98.
- [150] Moen, A.; Nicholson, D. G.; Ronning, M.; Emerich, H. *J. Mater. Chem.* **1998**, *8*, 2533–2539.
- [151] Dominkoa, R.; Belea, M.; Gabersceka, M.; Remskarb, M.; Hanzelb, D.; Goupilc, J.; Pejovnikd, S.; Jamnika, J. *J. Power Sources* **2006**, *153*, 274–280.
- [152] Wang, L.; Sun, W.; He, X.; Li, J.; Jian, C. *Int. J. Electrochem. Sci.* **2011**, *6*, 2022 – 2030.
- [153] Koleva, V.; Stoyanova, R.; Zhecheva, E. *Mater. Chem. Phys.* **2010**, *121*, 370–377.
- [154] Bakenov, Z.; Taniguchi, I. *Mater. Res. Bull.* **2011**, *46*, 1311–1314.
- [155] Taniguchi, I. *Mater. Chem. Phys.* **2005**, *92*, 172–179.
- [156] Doan, T. N. L.; Bakenov, Z.; Taniguchi, I. *Adv. Powder Technol.* **2010**, *21*, 187–196.
- [157] Kappe, C. O.; Dallinger, D.; Murphree, S. *Practical Microwave Synthesis for Organic Chemists: Strategies, Instruments, and Protocols*; Wiley – VCH: Weinheim, **2008**, Ch: 1–2.

- 
- [158] Hanson, H.; Beeman, W. W. *Phys. Rev.* **1949**, *76*, 118–121.
- [159] Liu, H.; Wang, Z.; Li, X.; Guo, H.; Peng, W.; Zhang, Y.; Hu, Q. *J. Power Sources* **2008**, *184*, 469–472.
- [160] Zou, H.; Zhang, G.; Shen, P. K. *Mater. Res. Bull.* **2010**, *45*, 149–152.
- [161] Park, K.; Son, J.; Chung, H.; Kim, S.; Lee, C.; Kim, H. *Electrochem. Commun.* **2003**, *5*, 839–842.
- [162] Higuchia, M.; Katayamaa, K.; Azumaa, Y.; Yukawab, M.; Suhara, M. *J. Power Sources* **2003**, *119–121*, 258–261.
- [163] Yang, S.; Zavalij, P. Y.; Whittingham, M. S. *Electrochem. Commun.* **2001**, *3*, 505–508.